Tailoring of filtration matrix design in dielectrophoretic filtration: towards selective separation for industrial tasks

Vom Fachbereich Produktionstechnik

der

UNIVERSITÄT BREMEN

zur Erlangung des Grades
Doktor der Ingenieurwissenschaften (Dr.-Ing.)
genehmigte

Dissertation

von

M. Sc. Maria Kepper

1. Gutachter: Prof. Dr.-Ing. Jorg Thöming
   (Universität Bremen)
2. Gutachter: Dr. Kai Hoettges
   (Universität Liverpool)

Tag der mündlichen Prüfung: 09.01.2025

This page is left blank intentionally.

This thesis is dedicated to Anna, Xéni, Anastasie, Jörn, Serge, and my cat Silence, whose love, support, and profound influence have guided me through these five challenging years.

I mourn the time this degree has kept us apart and the precious moments we forever missed together.

This page is left blank intentionally.

Zusammenfassung

Die selektive Abtrennung und Rückgewinnung von Mikro- und Submikropartikeln ist eine anspruchsvolle Herausforderung für viele Industriezweige. Neben anderen Techniken zur Bewältigung dieser Aufgabe hat sich die dielektrophoretische (DEP)-Filtration für die Partikelmanipulation etabliert. DEP-Separatoren sind vor allem in biomedizinischen Bereichen zu finden, können aber auch für nicht-biologische Partikel eingesetzt werden, z. B. für solche, die aus Elektronikschrott stammen.

Die Dielektrophorese arbeitet in einem inhomogenen elektrischen Feld und bewegt polarisierbare Partikeln in Abhängigkeit von ihren spezifischen Eigenschaften. Beispiele für diese Eigenschaften können die Größe dieser Partikeln, ihre Form oder ihr Material sein. Die dielektrophoretische Filtration basiert auf der Erzeugung dieses inhomogenen Feldes mit einem porösen Schüttgutfilter und zeichnet sich durch eine druckgesteuerte Strömung aus. In früheren Arbeiten zu diesem Thema wurde bereits gezeigt, dass die Abscheideleistung des Systems hauptsächlich von drei verschiedenen Arten von Faktoren abhängt. Der erste hängt mit den Partikeleigenschaften zusammen. Der zweite hängt mit den experimentellen Parametern zusammen, wie Durchflussmenge, Stärke und Frequenz des elektrischen Feldes und Modifikationen des Suspensionsmediums. Der dritte Faktor hängt mit dem Filter selbst und seinen Parametern zusammen, z. B. mit der Struktur oder dem Material. Die Struktur des Filters ist entscheidend, da sie die Gradienten im elektrischen Feld bestimmt. Die strukturellen Parameter des Filters wurden im Zusammenhang mit der Mikrofluidik eingehend untersucht, eine klare Verbindung zu den Bulk-Filtern im Zusammenhang mit der dielektrophoretischen Filtrierung wurde jedoch noch nicht hergestellt.

In dieser Arbeit wurden experimentelle Untersuchungen zur Modifizierung der Filtermatrix durchgeführt. Sie zielte darauf ab, die Abscheideleistungen verschiedener Typen von Schüttschichtfiltern mit der Kornmorphologie dieser Schüttschichtfilter in Verbindung zu bringen. Außerdem war es das Ziel, den Anwendungsbereich der DEP auf nicht-biologische Filtrationsaufgaben zu erweitern und die Art von Partikeln abzutrennen, die denen ähneln, die aus Batterie-Recycling-Schlämmen stammen. In einer ergänzenden Studie wurde untersucht, ob Materialveränderungen im Filter, wie z. B. die Einführung leitfähiger Einschlüsse

in Nanogröße im Schwamm, einen Einfluss auf die DEP-Filtration bei Frequenzen von ≈1 kHz haben.

Es wurde ein Vergleich der Abscheideleistung von Filtern in Schüttbettkonfiguration durchgeführt, die unterschiedliche Porenstrukturen, aber ähnliche Porositäten der Filtermatrix aufweisen. Die untersuchten Filterkörner bewegten sich zwischen 200 µm und 500 µm. Es wurde festgestellt, dass die DEP-Filtration von Polystyrol-Mikropartikeln mit einer Größe von 500 nm im Frequenzbereich von 1 kHz in hohem Maße von den geometrischen Überlegungen der Körner im Bulk-Filter beeinflusst wurde. Diese Filterkörner mit mehreren Kanten auf der Oberfläche zeigten die beste Abscheideleistung für Polystyrol-Mikropartikel. Die Unterschiede in den Wirkungsgraden, die mit den Veränderungen an den Kanten der Körner zusammenhängen, waren höher als die Unterschiede in den Wirkungsgraden, die mit der Größe der Körner zusammenhängen. Die Ränder wurden durch eine Mikro-CT-Untersuchung charakterisiert, bei der die Abstände zwischen der Oberfläche und dem Schwerpunkt der Körner analysiert wurden. Die Ergebnisse bereichern die Grundlagenforschung zu Schüttschichtfiltern und unterstreichen den Bedarf an weiteren Studien zur Korncharakterisierung. Die einfache Implementierung sowie die kostengünstige Handhabung von Schüttschichtfiltern mit modifizierten Körnern machen sie zu vielversprechenden Kandidaten für DEP mit hohem Durchsatz.

Eine materialselektive Trennung wurde an einem Gemisch aus Lithium-Eisenphosphat (LFP) und Graphitpartikeln durchgeführt: Materialien, die in modifizierter Form in den Kathoden- und Anodenteilen von Batterien enthalten sind. Die Trennung wurde in der experimentellen Umgebung ermöglicht, indem die Unterschiede in der Polarisierbarkeit dieser Partikel ausgenutzt wurden. Diese Ergebnisse zeigen, dass die DEP-Filtration ein gangbarer Weg für das direkte physikalische Recycling von Batterieabfällen ist.

Schließlich wurde ein Aspekt der Modifizierung des Filtermaterials anhand von Simulationen untersucht, die die Wirkung von leitfähigen Einschlüssen in den Minima und Maxima des inhomogenen elektrischen Feldes modellieren. Diese Simulationen zeigten, dass metallische Nanoeinschlüsse keine günstige Wahl für das Filterdesign sind, um die Abscheideeffizienz der DEP zu erhöhen.

Abstract

Selective separation and recovery of micro and sub-micro particles is a challenging task for many industries. Among the others techniques to tackle this task, Dielectrophoretic (DEP) filtration established itself for the particle manipulation. While being present for mostly biomedical fields, DEP separators can also be applied towards non-biological particles, such as the ones which come from the electronics scrap.

Dielectrophoresis operates in the inhomogeneous electric field and moves polarizable particles, depending on their specific properties. Examples of these properties can be the size of these particles, their shape or material. Dielectrophoretic filtration is based on the generation of this inhomogeneous field with a porous bulk filter and features pressure-driven flow. In previous works on this topic, it was already shown that the separation efficiency of the system would mainly depend on three different clusters of factors. The first one is related to the particle properties. The second one is related to the experimental parameters, such as flow rate, strength and frequency of the electric field and modifications of the suspension medium. The third one is related to the filter itself and its parameters, such as structural or material ones. The structure of the filter is a key as it defines the gradients in the electric field. The structural parameters of the filter were studied in detail in the microfluidic context, however, a clear link to the bulk filters in the context of dielectrophoretic filtration was not established yet.

This thesis performed experimental research on modification of the filter matrix. It aimed to connect the separation efficiencies of different types of the packed bed filters to the grain morphology of these packed bed filters. Additionally, the goal was to expand an application scope of the DEP towards non-biological filtration tasks, and separate the type of particles which resemble the ones that come from battery recycling slurry. A complimentary study explored whether material modification in the filter, such as implementation of conductive inclusions with nano-size scale inside the sponge, makes an impact on DEP filtration at frequencies of ≈1 kHz.

A separation efficiency comparison was performed within the bulk packed bed configuration filters that possess different pore structures but similar porosities of

the filter matrix. The investigated filter grains ranged between 200 µm - 500 µm. It was found that the DEP filtration of polystyrene micro-particles of 500 nm in the frequency range of 1 kHz was highly affected by the geometrical considerations of the grains inside the bulk filter. These filter grains with multiple edges on the surface demonstrated the best separation efficiency for polystyrene microparticles. The differences in efficiencies related to the changes in the edges of grains were higher than the ones observed with the changes in efficiency caused by the size of the grains. The edges were characterized by micro-CT inspection using an analysis of the distances from the surface to the center of the gravity of the grains. The findings enrich the basic research knowledge on the packed bed filters and highlight a need for the further studies with grain characterizations. The ease of implementation plus the inexpensive handling of packed bed filters with modified grains makes them promising candidates for the DEP high-throughput future.

A material-selective separation was performed on a mixture of lithium iron phosphate (LFP) and graphite particles: materials which, in a modified form, are present in the cathode and anode parts of the batteries. The separation was enabled in the experimental setting by taking the advantage of the differences in the polarizability of these particles. These findings underscored a roadmap of employing DEP filtration as a viable approach for direct physical recycling of battery waste.

Lastly, an aspect of filter material modification was investigated with simulations that model the effect of conductive inclusions located in the minima and maxima of the inhomogeneous electric field. These simulations showed that metal nano-inclusions are not a favorable filter design choice for enhancing the separation efficiency of DEP.

Acknowledgments

This work was funded at the University of Bremen in the framework of the research training group (GRK 1860) “Micro-, meso- and macroporous nonmetallic Materials: Fundamentals and Applications” (MIMENIMA) that was funded by the German Research Association (DFG) and an additional research grant from MAPEX Center for materials and processes received by me. I would like thank Prof. Dr.-Ing. Jorg Thöming for supervising this thesis, Dr. Kai Hoettges for agreeing to review this thesis in summer and acknowledge Dr. Michael Baune and my other colleagues and students from Center for Environmental Research and Sustainable Technology for their support.

My five years in Bremen were among the most trying times of my life and got marked by profound hardship. During this period, I encountered the global pandemic, two wars, the burning down of my home, the passing of my grandparents, and ultimately, the loss of my parent to cancer. As a result of these tragedies, I found myself responsible for my younger sister, a duty for which I was unprepared at the time. Consequently, a completion of this PhD seemed out of reach amidst these overwhelming circumstances. Yet despite the difficulties, I pushed myself through it, fueled by the memories of all the loved ones I had lost along the way.

Therefore, I wish to thank everyone who was there for me, easing the burden and shining as my brightest light throughout these times of 2019-2024.

A significant contribution which enabled me to do this thesis was made by Jörn, who took the best care and created a warm, safe and cozy atmosphere at home when the external world was failing. He helped in cherishing new ideas and dared me to follow my true passions, such as a career in industry, space applications, and moving into more people-focused roles that would bring me joy and fulfill a need for personal connection. His belief in me has made all the differences, and encouraged me to be in alignment with myself and do what I love, for which I am forever grateful.

The second contribution goes to my parent, who was a scientist bold enough to tell me: “Mein Herzchen, choose either what makes you happy or what makes you very happy. I only gave you an advice to pursue a purely technical career based on my personal experience, which, by the way, hasn't always been very good. I offered it

sincerely, out of love and a desire for your well-being. However, that doesn't make it foolproof for your personal happiness", and backed my aspirations for a change. Though he is no longer with us, I still hear his voice in my heart, reminding me to embrace life, not postpone it "to the better future", value family and disregard the naysayers who doubt my dreams.

The third acknowledgement goes to my former group lead Georg, who played a significant role in transforming me from a physicist to an engineer and continued to support me as I transitioned out of academia. His ability to constantly challenge me, great sense of humor, readiness to read this thesis on a short notice and a reliable companionship made this PhD journey much less lonely. It's a great pity that he moved away from Germany to Ireland and most of our communication is only digital now.

Finally, the fourth contribution goes to Sander. For all his jokes that brightened my mood, all the poffertjes he made, his Dutch honesty and the countless "let me proofread your thesis" moments. His presence made an immense difference in the atmosphere of my writing process, and his soft skills showed the magic to bring the best out of those around him (even when "those" were very grumpy with their PhD paragraphs in correction…).

I would like to explicitly acknowledge the company I'm working for at the moment and my manager Marcel who supported the flexible work-life-balance, motivated me to finish my PhD and gave me vacation for it. Credits also shall go to Yvan for proof-reading carefully the formulas I wrote here and last but not the least, to my beloved Parkrun volunteering team in Bremen who enlightened my weekends (which I spent thinking about this thesis).

List of publications

Kepper M., Karim M. N, Baune M., Thöming J., Pesch G.R., Influence of the filter grain morphology on separation efficiency in dielectrophoretic filtration. *Electrophoresis* **44**, 1645–1654 (2023). DOI: 10.1002/elps.202300075

Kepper M., Rother A., Thöming J., Pesch G. R., Polarisability-dependent separation of lithium iron phosphate (LFP) and graphite in dielectrophoretic filtration. *Results in Engineering.* **21**, 101854 (2024). DOI: 10.1016/j.rineng.2024.101854

O'Donnell M.C., **Kepper M.**, Pesch G.R. A brief history and future directions of dielectrophoretic filtration: A review. *Electrophoresis*. 1-21 (2024). DOI: /10.1002/elps.202400116

Contents

Chapter 1: Introduction

In our modern world, the rapid evolution of technology in the 21st century has brought about significant advancements, such as quantum computing, 5G technologies, artificial intelligence, and miniaturized semiconductor assemblies. These innovations have not only transformed our daily lives but also triggered a need for environmentally friendly technologies and efficient recycling mechanisms for the products produced. The following paragraphs in this chapter are rewritten from the author's 2023 publication [1] (distributed under CC BY 4.0) and adapted to the style of this thesis.

With electronics approaching the end of their lifetime, there occurs a demand for effective methods to retrieve precious materials that would otherwise be lost [2]. Broadly, a recycling process involves pre-treatment, size reduction, physical processing, and metallurgical or chemical purification stages [3]. For instance, once the electronic devices are undergoing recycling, they get dismantled and turn into electronic scrap. If one looks closer at its composition, it has the components of plastics, metals, and glass [3]. Recovering submicron metal particles from this dust is particularly demanding. Widely used methods such as gravity separation rely on particle density and size but are ineffective for small particles because their settling velocity differences are overshadowed by diffusional motion. Although electrophoretic separation continues to be an alternative, it depends on the particle's charge as its key property, thus limiting an application of such a process. To explore a broader range of target particle properties and facilitate sorting without relying on particle charge, dielectrophoretic (DEP) forces provide an interesting alternative [4,5]. The dielectrophoretic approach has a long history in biomedical applications, for instance, in cell manipulation or separation [6–11]. However, in theory, it is also suitable for intricate non-biological separation challenges such as conductive particle recovery from dust [12,13].

The heart of the DEP effect lays in the inhomogeneous electric field. The target particles are suspended in a liquid medium, which gets pushed through a DEP separator. A general classification of DEP separators can be done according to the origin of the electric field. The existence of the two major categories is established in the field: insulator-based DEP (iDEP) and electrode-based DEP (eDEP). Broadly, to

the class of eDEP devices belong microfluidic chips [14] and they are frequently used in fields that do not aim for high volumetric throughputs, such as cellular analysis [15]. A pathway out of this throughput limitation for eDEP devices was demonstrated with an implementation of custom-designed printed circuit boards, highly lowering the fabrication expenses and paving a way towards the scaling up (up till 2023 up to 6 mL/min [16]). Other methods exist that allow separation in the mL/min range, such as DEP field flow fractionation, but they are challenging to scale up further [17]. Electrode-less or insulator-based DEP is a second option for generating field inhomogeneities. Senichi Masuda et al. used this term in 1989 [18]. Particularly, in this principle, the electrodes are located outside the space of the DEP movement region. An insulating material is placed in this void space between the two electrodes and thus generates a spatial variation of the electric field [19]. This results in local extrema of the electric field. Dielectrophoretic filtration is a sub-section of iDEP, concentrating on bulk porous structures (filters) as the DEP region and pump-based liquid manipulations. The electric field appearing inside these porous dielectric constructions is highly inhomogeneous because of the scattering of the electric field at the solid-liquid boundaries of each obstacle and pore inside the filter. Key benefits of this approach are a more straightforward fabrication process without the necessity for advanced electrode patterns, and reduced vulnerability to low performance caused by fouling of the electrode surface [20]. Its potential scalability for higher throughput was demonstrated in several research works at University of Bremen by the group of Prof. Thöming [21–23].

This thesis aims to dive deeper in the dielectrophoretic filtration process. The **second chapter** gives a short theoretical overview, which is essential to understand the underlying principles. The **third chapter** highlights the state-of-the-art in dielectrophoretic filtration for non-biological particles and establishes the potential applications of the technique as a motivation for the studies in this thesis. **The fourth chapter** introduces the goals of this thesis. **The fifth chapter** presents results of a study of geometrical aspects of the filter matrix. **The sixth chapter** shows results on the application of dielectrophoretic filtration to a mixture separation task with relevance to lithium-ion battery recycling. **Chapter seven** concentrates on investigating the material-related changes in the filter. **Chapter eight** summarizes the thesis outcomes. The author would like to note that the theory sections and the first two results chapters are based on author's first two articles for this thesis [1,24].

Chapter 2: Theory

Dielectrophoresis is a motion of polarizable particles under the influence of an inhomogeneous electric field. To understand its underlying mechanisms, one must know some basics of the electric field and polarizability.

Several books give a great step-by-step introduction to this, which the author highly recommends for a comprehensive overview, such as: a book titled "AC electrokinetics: Colloids and Nanoparticles" by Hywel Morgan and Nicolas Green from 2003; a book titled "Electrokinetics and Electrodynamics in Microsystems. International center for mechanical sciences (CISM), Courses and Lectures, vol. 530", edited by Antonio Ramos in 2011 and a book "Dielectrophoresis Theory, Methodology and Biological Applications" by Ronald Pethig from 2017 [14,25,26]. This thesis does not cover all content but gives the essentials needed to understand the conducted experiments.

In this chapter, the description begins with the fundamental laws of physics, such as Coulomb's law. It outlines the electromagnetic principles by introducing expressions for the electric field, its potentials, and the displacement in the medium. Then, dielectrophoretic (DEP) force is introduced along with a concept of polarizability for the target particles and their movement under electric field applied. This section concludes by an overview of particle capture mechanisms, interactions between the particles, and other electrokinetic forces.

I. Basics of electrostatics

The text below is based on the sections of the book by Hywel Morgan and Nicolas Green (2003), pages 15-22, which have been shortened and rewritten in the appropriate style and storyline for the thesis [14].

In the quasi-electrostatic system, the existing charges are assumed to be stationary, or their movement does not impose any deviations in the electromagnetic field. When there is a system of stationary charges, for instance, a presence of two charges close to each other, they will exert a force on each other. Depending on a sign of the charges, they would either exhibit attraction or repulsion. This force describing

a fundamental interaction between charges would depend on the distance in-between them and can be expressed as:

$$\mathbf{F} = \frac{Q_1 Q_2}{4\pi\varepsilon_0 |\mathbf{r}_{12}|^3} \mathbf{r}_{12}, \tag{2.1}$$

where Q_1 and Q_2 are the static charges, ε_0 is vacuum permittivity and is equal to $8.854\times10^{-12}\ \frac{\mathrm{F}}{\mathrm{m}}$, $\mathbf{r}_{12}$ is a vector directed from one charge to another with its absolute value $r = |\mathbf{r}_{12}|$ equal to the distance separating charges. Equation (2.1) is called Coulomb's law.

Further, any charged particle or a point charge produces a surrounding non-uniform electric field. The electric field $\mathbf{E}$ of a single charge Q is defined as:

$$\mathbf{E}(\mathbf{r}) = \frac{Q}{4\pi\varepsilon_0 |\mathbf{r}|^3} \mathbf{r}, \tag{2.2}$$

which can be derived from Coulomb's law, taking one of the charges to be test charge and defining $\mathbf{r}$ as distance vector which points from the charge Q to the test charge. In this case, test charge can be treated as point of electric field measurement. A principle which describes an impact of the sum of charges is called a superposition principle. According to this, to calculate a total electric field at a particular point, one has to get a vector sum of the local electric fields.

One of the central concepts of this thesis is polarizability. Introducing a dipole moment is necessary to describe it. The polarizability is a vector $\mathbf{p}$ defined for a system of two opposite charges with equal absolute charges Q, and distance vector $\mathbf{r}_{12}$ between them:

$$\mathbf{p} = Q\mathbf{r}_{12}. \tag{2.3}$$

This vector is directed from negative charge to positive charge. Such a system of charges is called a dipole. In chemistry, many molecules have permanent dipoles, which do not depend on the surrounding electric field (Figure 2.1).

In a uniform electric field, a potential energy of the dipole, associated with its orientation in the applied field, is:

$$U = -\mathbf{E} \cdot \mathbf{p}. \tag{2.4}$$

When the dipole is perpendicular to the field, U is zero.

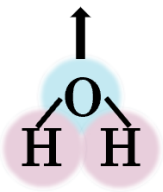

Net dipole moment ≠ 0

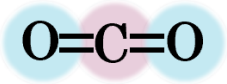

Net dipole moment = 0

FIGURE 2.1 A schematic of a polar water molecule with non-zero net dipole moment (marked with black arrow) and a non-polar carbon dioxide molecule with zero net dipole moment due to its linear molecule geometry.

In a non-uniform stationary electric field, the force acting on the dipole is:

$$\mathbf{F} = (\mathbf{p} \cdot \boldsymbol{\nabla})\mathbf{E}. \tag{2.5}$$

The lines of the dipolar electric field point from the positive to the negative charge. The strength of the electric field is proportional to the number of electric field lines.

It is convenient to work with scalar parameters instead of vectors. For this reason, the electrostatic potential φ of the electric field can be introduced. The electric field and its scalar potential are connected in the following way:

$$\mathbf{E} = -\boldsymbol{\nabla}\varphi. \tag{2.6}$$

Additionally, to describe other objects in the electric field, surface and volume electric charge densities can be used as:

$$\sigma_\rho = \frac{\Delta Q}{\Delta S}, \rho = \frac{\Delta Q}{\Delta V}. \tag{2.7}$$

Another helpful quantity in this context is the electric flux Φ. By considering an infinitely small space within the non-uniform electric field and corresponding small surface area element $d\mathbf{S} = \mathbf{n}dS$, where $\mathbf{n}$ is a surface outward normal vector, one can define the flux of the electric field strength vector through the $d\mathbf{S}$ as [27]:

$$d\Phi = \mathbf{E} \cdot d\mathbf{S}. \tag{2.8}$$

With the free and bound charges existing in the space and with their given volume charge densities $(\rho_\mathrm{f} + \rho_\mathrm{b})$, a following relation is called Gauss's law:

$$\boldsymbol{\nabla} \cdot \mathbf{E} = \frac{\rho_\mathrm{f} + \rho_\mathrm{b}}{\varepsilon_0}. \tag{2.9}$$

According to Gauss's law, the net electric flux Φ through the closed surface, which covers a specific volume, is proportional to the net charge within the given volume[26]. Thus, if there is information about electric charge distribution, the electric field is also known then.

I.1 Electrostatics in matter: polarization and dielectric permittivity concepts

In the presence of matter, electric field can have a complex structure. In this case, it is usually treated in terms of three vector fields: the electric displacement field **D**, an electric field without displacement **E**, and the polarization **P** [14]:

$$\mathbf{D} = \varepsilon_0 \mathbf{E} + \mathbf{P}. \tag{2.10}$$

Further elaboration on this equation is essential as it bridges material characteristics to the electric field concept.

In dielectrics, the charges are not able to move. However, the electric field can cause their displacement. For example, in one of these displacements, positive nuclei might exhibit movement along the field while electrons distort their path in the orbit in the opposite direction of the field. The total effect of it is then referred to as polarization of the bound charges in the dielectric [14,28]:

$$\rho_b = -\nabla \cdot \mathbf{P}. \tag{2.11}$$

Here, ρ_b is the density of bound charges as defined in Equation (2.9). For the case when dielectric is assumed linear and isotropic, polarization and electric field can be connected as[14]:

$$\mathbf{P} = \varepsilon_0 \chi_{ae} \mathbf{E}, \tag{2.12}$$

where χ_{ae} is the electric susceptibility of the material. This relation allows for the introduction of another vital parameter – dielectric permittivity. By defining the dimensionless relative permittivity as:

$$\varepsilon_r = 1 + \chi_{ae} \tag{2.13}$$

and also introducing absolute permittivity $\varepsilon = \varepsilon_0 \varepsilon_r$, one can then rewrite Equation (2.10) as:

$$\mathbf{D} = \varepsilon_0 \mathbf{E} + \varepsilon_0 \chi_{ae} \mathbf{E} = \varepsilon_0 (1 + \chi_{ae}) \mathbf{E} = \varepsilon_0 \varepsilon_r \mathbf{E} = \varepsilon \mathbf{E}. \tag{2.14}$$

which connects the material properties and the applied macroscopic electric field. The relative permittivity is connected to the chemical structure of the given material, and it usually depends on the frequency of the applied electric field.

I.2 Ideal and non-ideal dielectric and conductive media

The text below is based on the sections of the book by Hywel Morgan and Nicolas Green (2003), pages 17, 24-26, which have been shortened and rewritten in the appropriate style and storyline for the thesis [14].

As a rule, real matter appears to be neither fully dielectric nor fully conductive. Conductivity describes how easily electric charges can move through a material when an electric field is applied, linking directly to a current density. When an electric field is applied to the media with conductivity σ, electric current will flow through that medium. The current density $\mathbf{J}$ can be expressed via Ohm's law[14]:

$$\mathbf{J} = \sigma \mathbf{E}. \tag{2.15}$$

Here, Ohm's law is presented in its differential form.

In the case of an ideal conductor, when the electric field is applied, the free charges experience movement, and no energy storage is caused by polarization. The charges are attached to the bulk of the conductor and cannot escape it. The electric fields also do not penetrate it. To arrange that, the induced bound charge density at a perfect conductor's surface compensates for the electric field's free charge density.

In turn, Equation (2.14) valid for the case of an ideal dielectric that has zero conductivity. For a material with a finite (non-zero) conductivity σ, the complex permittivity, which would depend on a specific field frequency ω, can be introduced as follows:

$$\hat{\varepsilon} = \varepsilon_0 \varepsilon_r - i\frac{\sigma}{\omega}. \tag{2.16}$$

Here, imaginary unit $i = \sqrt{-1}$ has been introduced.

This difference between ideal and non-ideal dielectric can be seen from a following concept. For the case of a dielectric material without losses, let us closely follow the reasoning from the book of Hywel Morgan and Nicolas Green (2003) and assume a capacitor with parallel plates and a specific permittivity[14]. Let us assume a parameter such as the specific capacitance $C = \mathrm{Re}\,\varepsilon\frac{S}{d}$, where S is the area of the

capacitor's plates, Re states for the real part of the complex number, ε is the complex permittivity, and d is the distance between those plates. In this context, an impedance, referring to the resistance which dielectric has towards the electric field, for a loss-free dielectric can be expressed as $Z = \frac{1}{i\omega C}$. However, when this dielectric is non-ideal, it can be seen as a system of a parallel-connected loss-free capacitor and a resistor. In this case, the total impedance Z can be redefined, writing $R = \frac{1}{\sigma}\frac{d}{S}$ for the resistor, as [14]:

$$Z = \frac{1}{\frac{1}{R} + i\omega C} = \frac{1}{i\omega \frac{S}{d}\hat{\varepsilon}}. \tag{2.17}$$

The impedance reflects the dependance on the permittivity and the conductivity of the material and shows the ability of the dielectric material to store electrical energy (via permittivity) and a tendency to dissipate energy as heat (via the conductivity). The impedance of the material affects the strength and distribution of the electric field within this media.

I.3 Electrostatic approximation on the very low frequencies

In the case of the two electrodes spaced by a given distance, a homogeneous electromagnetic field is created between them. This capacitor-like configuration consists of two parallel plates connected to an external generator by a pair of wires to which a voltage is applied. In the case of DC voltage, a positive charge will appear on one of the plates, a negative charge will appear on the other, and a uniform electric field will occur between the plates. If an AC voltage of low frequency is applied to the plates instead of a direct current, then the electromagnetic field between the plates can be represented with the zeroth order Bessel function of the first kind J_0, c is the speed of light, and E_0 is electric field amplitude as [29]:

$$\mathbf{E} = E_0 \exp(-i\omega t)\, J_0\left(\frac{\omega r}{c}\right)\mathbf{e}_z. \tag{2.18}$$

Following the reasoning from Richard P. Feynman[29], it is assumed that **E** is directed from one plate to the other. To denote this direction, one can employ $\mathbf{e}_z$ unit vector, which corresponds to the z axis, which in turn is collinear to **E** and orthogonal to both capacitor plates. Here are additionally implicitly introduced polar axes r and ϕ, with unit vectors $\mathbf{e}_r$ and $\mathbf{e}_\phi$ which are orthogonal to $\mathbf{e}_z$ and to each other. This is necessary

to estimate the field values in the very low-frequency range. In particular, the corresponding magnetic field can be estimated from Maxwell's equations as [27]:

$$\mathbf{H} = \frac{\boldsymbol{\nabla} \times \mathbf{E}}{i\frac{\omega}{c}} = -iE_0 J_1\left(\frac{\omega r}{c}\right)\mathbf{e}_\phi. \tag{2.19}$$

Here, × denotes a vector product and $J_1$is a Bessel function of the first kind of 1st order.

In the low-frequency limit, the following relations are valid, as follows from the Bessel function asymptotic properties [30]:

$$\frac{\omega r}{c} \ll 1, \tag{2.20}$$

$$J_0\left(\frac{\omega r}{c}\right) \to 1, \quad J_1\left(\frac{\omega r}{c}\right) \to 0. \tag{2.21}$$

Therefore, one can state that $\mathbf{E} \approx E_0 \exp(-i\omega t)\mathbf{e}_z$ and $\mathbf{H} \approx 0$. Hence, the external field applied in this approximation can be considered to be purely electric within the very low-frequency range (in particular for this thesis at 1 – 15 kHz). This further allows to consider problems in the electrostatic formulation, avoiding general Helmholtz equations and thus relying on the Laplace equation instead. The latter can be obtained by combining Equation (2.6) with Equation (2.9), assuming that $\rho_f + \rho_b = 0$ [26]:

$$\boldsymbol{\nabla}^2\varphi = 0. \tag{2.22}$$

Alternatively, the Laplace equation can be derived as an approximation to the Helmholtz equation in the very low-frequency limit, and the Helmholtz equation for scalar and vector field potentials can be obtained directly from the Maxwell system of equations. These mathematical derivations are outside the scope of the current thesis.

II. Dielectrophoresis (DEP)

The theoretical framework outlined above guides the reader to the main topic of this thesis. Dielectrophoresis is a movement of polarizable particles which occurs in DC or AC fields. Not so long ago, in the range of frequencies above 1 kHz, DEP was demonstrated to be the main electrokinetic effect [31]. The DEP force appears only when the electric field is non-homogeneous.

The DEP force emerges in this theory section as a main factor. This force is proportional to the volume of the target particle and, in the case of a small spherical particle, is written as [14]:

$$\mathbf{F}_{\mathrm{DEP}} = \pi\varepsilon_{\mathrm{m}} r_{\mathrm{p}}^3 \mathrm{Re}[f_{\mathrm{CM}}]\nabla|\mathbf{E}|^2 \tag{2.23}$$

Here in the formula, r_{p} represents the radius of the particle, ε_{m} is dielectric constant permittivity of the medium (suspension), f_{CM} is Clausius–Mossotti (CM) factor, and $\mathbf{E}$ is the amplitude for the applied electric field which can be translated to a root-mean-square (rms) electric field vector as $\mathbf{E}_{\mathrm{rms}} = \sqrt{0.5}\mathbf{E}$.

DEP target particles are usually suspended in the liquid [14]. The subsections below briefly cover general polarization types, Clausius–Mossotti (CM) factor and target particle polarizability, double layer contributions to it and finally the motion of target particles with DEP.

II.1 General polarization types

In the context of DEP, target particles polarize in electric field. Generally, different materials possess different polarization types, which impacts the polarizability and, thus, the DEP behavior of the particle.

For a comprehensive understanding of the polarization mechanisms, the author strongly recommends the book titled "Dielectric Phenomena in Solids" by Kwan Chi Kao from 2004 (section 2.2.3) [32]. Here, only the basic concepts of the polarization types will be discussed in a broad manner. The text in this section is mostly based on the sections of the book edited by Antonio Ramos (2011), particularly, pages 34-35, 43-44, 47-48, 57 shortened and rewritten in the appropriate style and storyline for the thesis [25].

Typically, each dielectric material needs its unique time to achieve the maximum polarization effect. This time is referred to as dielectric relaxation. In low-frequency regimes, the dipoles can be considered fully aligned with the field, hence maximum polarization is obtained. When the field frequency is increased, the polarization decreases, as the dipoles are only aligned to the field for a fraction of the period of the alternating field. At the higher frequencies, the dipoles can no longer align with the electric field; thus, no polarization occurs in the material.

Four main polarization mechanisms with frequency responses (and reaction times) can be distinguished and present in the dielectric: atomic, electronic, orientational,

and interfacial. A brief overview of them is given below. It shall be noted that the overall polarization would be a combination of those types mentioned here.

a) Atomic

This type represents the displacement of charges induced by the motion of ions in a crystalline solid structure. This type of polarization is found on high frequencies in the range of 10^{12} Hz [25].

b) Electronic

This type of polarization can be found in all materials, too and exists on the frequencies of the order of 10^{15} Hz [25]. Taking a single atom as an example, in an absence of the electric field, the force of the positive nucleus balances the average electrostatic force imposed on the negative electrons. When the electric field is present, the center of the negative charge is displaced and no longer located around the positive nucleus, forming the non-zero dipole moment from there.

c) Orientational

This type can occur at materials which have permanent electric dipole and is typically on the frequencies of 10^6-10^9 Hz [25]. Particularly, when permanent dipole moments of the molecules align in the electric field, orientational polarization is induced. This polarization observes the longest relaxation time, and the overall representation of this polarization can be given as:

$$\mathbf{P}_{\text{orientational}} = \frac{\varepsilon_0 \chi_{or}}{1 + i\omega\tau_{or}} \mathbf{E}. \tag{2.24}$$

Here, χ_{or} is a low-frequency limit for the orientational susceptibility, and τ_{or} is orientational relaxation time. Analogically, for the low frequency,

$$\chi_{ae} + \chi_{or} = \varepsilon_s - 1, \tag{2.25}$$

where ε_s is a permittivity in the case of unchanging in time electric field. When the frequencies are high,

$$\chi_{ae} = \varepsilon_\infty - 1, \tag{2.26}$$

where ε_∞ is a permittivity of the material at the frequency when no orientational polarization is present. Then, the resulting total polarization is expressed as:

$$\mathbf{P}_{\text{total}} = \varepsilon_0 \left(\chi_{ae} + \frac{\chi_{or}}{1 + i\omega\tau_{or}} \right) \mathbf{E}. \tag{2.27}$$

Then, building upon the knowledge of non-ideal dielectrics, their complex-valued relative permittivity, can be expressed as:

$$\varepsilon_r = \left(\varepsilon_\infty + \frac{\varepsilon_s - \varepsilon_\infty}{1 + i\omega\tau_{or}}\right) - i\frac{\sigma}{\varepsilon_0\omega}. \tag{2.28}$$

It is helpful to rewrite permittivity in terms of its real and imaginary parts: $\varepsilon = \varepsilon_0\varepsilon_r = \varepsilon' - i\varepsilon''$:

$$\varepsilon' = \varepsilon_0\left(\varepsilon_\infty + \frac{\varepsilon_s - \varepsilon_\infty}{1 + \omega^2\tau_{or}^2}\right), \tag{2.29}$$

$$\varepsilon'' = \varepsilon_0\left(\frac{(\varepsilon_s - \varepsilon_\infty)\omega\tau_{or}}{1 + \omega^2\tau_{or}^2}\right) + \frac{\sigma}{\omega}. \tag{2.30}$$

These equations are known as Debye relations. In the first term, the ε' is responsible for the polarization capacity of the material. In contrast, the second term is accountable for the transfer from electrical to thermal energy, thus, ensuring the presence of losses in the medium. These equations complete a basic review of the dielectric permittivity concept. At frequencies of $\omega \ll \tau^{-1}$ when ε'' is zero, **D** and **E** are in phase, and after one-half cycle of the electric field, the energy returns to the driving source in the second half-cycle. The energy loss would occur due to Joule heating as a process of transfer of electrical energy into the heat and the present electric conductivity in the material.

d) Interfacial (Maxwell-Wagner)

This type of polarization is relevant for materials with internal interfaces and is the most important for describing DEP. It relies on the interface's effective surface and its morphology. In DEP, typically, liquid and the dielectric material come in contact. They possess different electrical properties. This system can be approximated as a capacitor composed of two materials and modelled with an equivalent circuit, with a total impedance being a sum of the two involved. From there, the complex permittivity of such a system would have a dispersion coming from the differences in conductivities and permittivities of these two materials. Relaxations imposed by this type of polarization are present in the frequency range much lower than those for electronic, atomic and orientational polarization. More information on this polarization type is given in the section below.

II.2 Target particle: polarizability and Clausius–Mossotti factor

The polarization model which reflects the frequency-dependent polarization of materials and particularly incorporates the interfacial polarization effect is the Maxwell-Wagner model.

Generally, the induced dipole on particles has an origin in interfacial polarization. A charge separation along the diameter of the particle appears. A close estimate of this separation might be explained as two charges located on both ends of the particle being of the same magnitude but possessing a different sign. A Coulomb force will be present and due to the non-homogeneous external field, the force on one side will be stronger than on the other, leading to a net force leading to particle mobility [1,33]. In this thesis, the particles which are of interest are sub-micron to micron range and are introduced to a suspension in low concentration. In this regime it can be assumed that the dipole approximation describes the particle polarization well. An important assumption is that the sizes of the target particles are smaller than the scale of non-uniformity of the electric field.

The text below is based on the sections of the book by Hywel Morgan and Nicolas Green (2003), pages 35-39, which have been shortened and rewritten in the appropriate style and storyline for the thesis [14].

The induced (effective) dipole moment is influenced by the parameters of the applied electric field, the properties of the target particle itself, and the media with relative permittivity ε_m in which it is suspended. In the most simplified form, a spherical solid particle of radius r_p submerged inside the suspension can be used as an example. The effective dipole moment is equal to [14]:

$$\mathbf{p} = \varepsilon_m 4\pi {r_p}^3 \frac{\hat{\varepsilon}_p - \hat{\varepsilon}_m}{\hat{\varepsilon}_p + 2\hat{\varepsilon}_m} \mathbf{E}, \tag{2.31}$$

with $\hat{\varepsilon}_p, \hat{\varepsilon}_m$ the complex permittivity of the particle and the medium, correspondingly. This dipole moment is proportional to the applied electric field via a polarizability term. In the case when the target particle is not spherical, is important to note that the effective dipole moment and polarizability would in general derive not only from the size but also from the orientation of the particle. For example, for the elliptical or rod-shaped particles, the polarizability would differ and in the case of more complex shapes an estimation of the polarizability involves numerical methods. These complex shapes are not a focus of this thesis.

In the formula above, the term before the **E,** is called the Clausius–Mossotti (CM) factor and can be marked as f_{CM}. It reflects the frequency dependence of the polarizability. The key aspects influencing this parameter are the complex permittivities of the particle and the suspension or a liquid medium in which this particle is located $(\hat{\varepsilon}_p, \hat{\varepsilon}_m)$ [14]:

$$f_{\mathrm{CM}} = \frac{\hat{\varepsilon}_p - \hat{\varepsilon}_m}{\hat{\varepsilon}_p + 2\hat{\varepsilon}_m}. \tag{2.32}$$

The polarizability of the given particle is associated with the relaxation time of Maxwell-Wagner (MW):

$$\tau_{MW} = \frac{\varepsilon_p + 2\varepsilon_m}{\sigma_p + 2\sigma_m}. \tag{2.33}$$

The real part of the CM factor changes concerning relaxation frequency, according to the following relations in Table 2.1 and Figure 2.2.

Low frequencies $\left(\ll \frac{1}{2\pi\tau_{MW}}\right)$	**High frequencies** $\left(\gg \frac{1}{2\pi\tau_{MW}}\right)$
$\frac{\sigma_p - \sigma_m}{\sigma_p + 2\sigma_m}$	$\frac{\varepsilon_p - \varepsilon_m}{\varepsilon_p + 2\varepsilon_m}$

TABLE 2.1 CM factor in different frequency ranges[14].

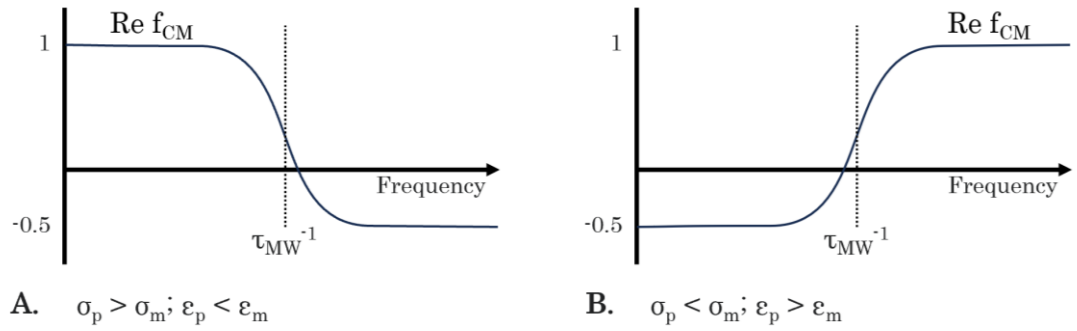

FIGURE 2.2 Illustration of the low and high-frequency dependencies of the real part of the CM factor, reflecting the properties of the liquid suspension (m) and the particle (p). This is created by the author based on explanations from of the Hywel Morgan and Nicolas Green (2003) book (page 39, Figures 3.4, 3.5 [14]).

The real and imaginary parts of the Clausius-Mossotti factor can take certain values: for the real part, the maximum and minimum are 1 and -0.5, and for the imaginary part, the maximum and minimum are 0.75 and -0.75.

When the sign and the value of the CM factor are determined, one can assume the direction of the movement for the target particles. In the following two paragraphs is rewritten a theory part from the author's publications from 2023 and 2024, which describes well this parameter [1,24].

When the real part of the CM factor is positive, the surrounding medium is less polarizable than the particle. Then, the force points along the field gradient towards the maxima of the electric field, and is called positive dielectrophoresis (pDEP) [14]. When the real part of this factor is negative, the medium is more polarizable than the particle. The force then repulses the target particle from the electric field's maxima against its gradient. It is called negative dielectrophoresis (nDEP) (Figure 2.3). Particles can cross over from pDEP to nDEP or vice versa with a change in frequency. As was discussed above, at high frequencies, the real-valued permittivities determine the behavior; at low frequencies, the conductivities determine it [14].

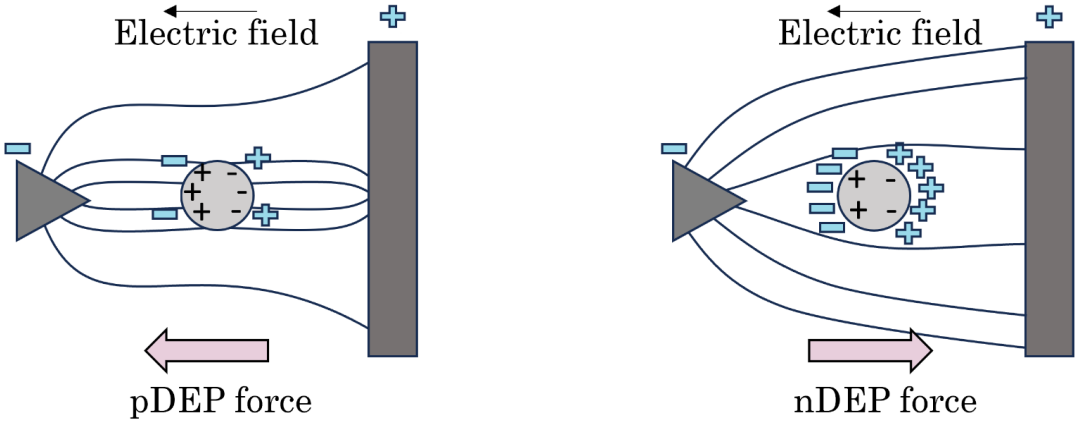

FIGURE 2.3 DEP movements of the particle. This figure is created by the author and is inspired by the Nicolas Green and Hossein Nili book (2012) (page 540, Figure 6 [34]).

Several particle properties influence the DEP force. This enables the mixture of the different target particles to be separated in the desired way. The separation of two different particles can be arranged when they demonstrate significantly different real parts of the CM factor. While the conductivity and permittivity of the particle are, in most cases, not a changeable parameter, both the suspension conductivity and applied field frequency might be varied for the goal of getting largely different $\mathrm{Re}[f_{\mathrm{CM}}]$ of both types of particles. By following this, a mechanism of a material-

selective DEP separation in a particle mixture becomes feasible, which will be further employed in this thesis.

To dive deeper into the concept of particle separation and their polarizability differences in the suspension, the importance of the double layer and its influence on the polarizability shall be explained.

II.3 Double layer contributions

The text below is based on the sections of the book by Hywel Morgan and Nicolas Green (2003), pages 85, 90-96, 126-128, which have been shortened and rewritten in the appropriate style and storyline for the thesis [14].

Double layer (DL) is a necessary term when it comes to the description of the particle polarization behavior in liquid media. The double layer consists of two components: Stern and diffusive layers (Figure 2.4). A brief explanation will be presented in the next paragraphs.

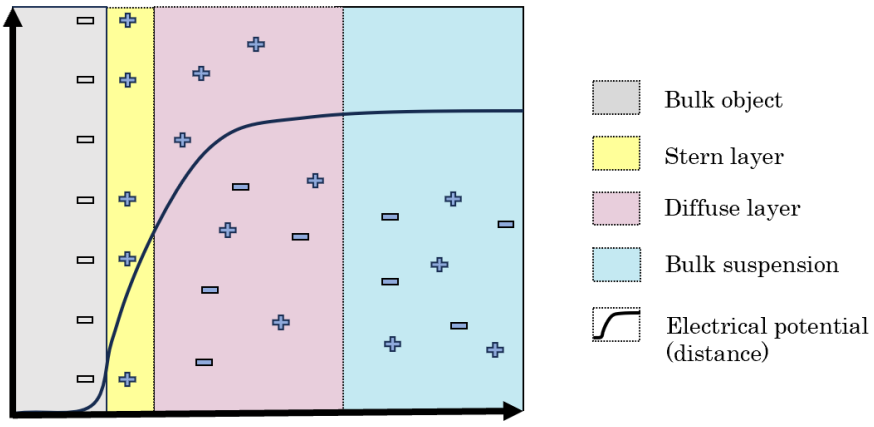

FIGURE 2.4 A simplified double layer (Stern and diffusive layer) formation around a negatively charged surface. This schematic is created by the author and is based on the original image from the paper of Matthias Buecker et al. (2019) (page 5658, Figure 1 [35]).

In general, when an object comes into contact with liquid on its surface, two mechanisms create a net charge, leading to an electrostatic surface potential. One mechanism is the dissociation of the chemical groups and the second one is an adsorption process of molecules or ions from the liquid. The counter-charged ions, densely located near the surface of the submerged body, form a bound part of the double layer called the Stern layer. Further from the surface of the object would be

a region in which charges of the opposite sign would be attracted closer to the surface, and charges with identical sign to the one on the surface would be repelled. This region is called a diffuse layer. This layer screens the surface charge of the object. Therefore, the overall charge globally remains neutral.

Following the Figure 2.4, the potential of the object's surface decreases up to the interface between the stern and diffuse layers. In the diffuse layer, the potential drops exponentially with a characteristic distance. This distance is normally around several nm and is called Debye length[14] which the author denotes as k^{-1}:

$$k^{-1} = \sqrt{\frac{\varepsilon_0 \varepsilon_r T k_B}{2z^2 Q_-^2 c_{ion}}}, \tag{2.34}$$

where z is ion valence, Q_- is the elementary charge, the concentration of ions in liquid is c_{ion}, k_B is the Boltzmann constant, and T is the temperature. The diffusive layer and the bulk suspension have a slipping plane in between, at which the molecules can move freely. This slipping plane has a potential called zeta potential, which can be determined experimentally. This measurement is particularly important to determine the "sticking" of the target particles to the filter matrix in the absence of the DEP.

The paragraphs below in this section are devoted to the discussion of surface conductance of the particles, which is particularly important for DEP trapping. It shall be noted that in the cases when the DL is bigger than the dimensions of the target particle, it require a different approach [36], which is not a subject of this thesis.

The presence of the DL results in changes in the particle's overall polarizability, and as a consequence the Maxwell-Wagner (MW) model stops describing the system's behavior well. Another model, Maxwell-Wagner-O'Konski (MWO), is then considered to be more suitable. O'Konski, in 1960, modified the derivation of a particle's dipole moment, and represented the particle conductivity σ_p was as a sum of two components, bulk and surface conductivities, written as [14]:

$$\sigma_p = \sigma_{\mathrm{p,bulk}} + \frac{2K_{\mathrm{s}}}{a}. \tag{2.35}$$

K_{s} is a surface conductance, composed of two contributions: namely diffuse and Stern layer. The Stern layer conductance does not change with changes in the ionic

concentration of the suspension. The diffuse layer conductance is influenced by the size of the submerged particle and by the ionic concentration of the suspension.

This MWO model explains well the dielectric properties of colloidal particles [14], however, it no longer applies at very low frequencies (for example, at couple of Hz). There, the Dukhin-Shilov (DS) model is a better choice, as it accounts for ion diffusion, which comes from the evolved DL [36]. These extensions are not a central topic of this thesis.

It shall be noted that while several models can be used to predict the surface conductance of the particle, an experimental investigation is needed in some cases. Thermodynamic conditions of the experiment and the surface structure of the particle would play a crucial role in these predictions.

For the experimental part of this thesis, polystyrene target particles will mainly be used to characterize the DEP filter performance. For particles with a size of 1 μm, their surface conductance is around 1 nS [37]. This highly impacts their resulting total conductivity[1], leading to the fact that at frequencies up to 10 kHz in deionized water, these particles would possess positive real part of CM [38].

In the case of the target particles made of metal, a review by Antonio Ramos et al. (2016) is a good source for the further DL discussion [39]. While considering at the CM factor, metal particles seem to be more polarizable than most of the media in which they can be submerged. However, for the low AC or DC currents, some negative CM factors were detected [40]. That can potentially be attributed to the following. In metals the double layer's charges compensate for the particle's primary induced dipole. Thus, at the very low frequencies metal particles seem to be non-conductive and also less polarizable than the media in which they are submerged, and have a negative CM. To fully charge the double layer, the frequency f_{DL} is required [41,42]:

$$f_{DL} = \frac{C}{\sigma_m}. \tag{2.36}$$

Here, C is an estimated capacity of the DL and σ_m is the conductivity of the liquid in which the particle is submerged. At frequencies higher than f_{DL}, the real part of the CM factor for metals turns out to be positive.

II.4 Motion of particles with DEP, fluid flow considerations

Now that the basics for the polarizability of the target particles have been established, the next point would be to look into the motion of them and in the processes taking place in the liquid. The text below is mostly based on the sections of the book by Hywel Morgan and Nicolas Green (2003), pages 66-69, 76-78, which have been shortened and rewritten in the appropriate style and storyline for the thesis [14].

To have a complete understanding of the motion of the particles in the system, one has to account for the fluid flow profile and the impact of DEP force on it. In general, the equation that characterizes the motion of the incompressible fluid is called the Navier-Stokes equation and is written as [14]:

$$\rho_{FL}\frac{\partial \mathbf{u}}{\partial t} + \rho_{FL}(\mathbf{u}\cdot\boldsymbol{\nabla})\mathbf{u} = -\boldsymbol{\nabla}\Pi + \eta\boldsymbol{\nabla}^2\mathbf{u} + \mathbf{F}, \qquad \boldsymbol{\nabla}\cdot\mathbf{u} = 0 \tag{2.37}$$

Here ρ_{FL} is a fluid density, Π is the pressure, $\mathbf{u}$ is fluid velocity, η is the dynamic viscosity and $\mathbf{F}$ is the vector sum of all applied forces, which also includes DEP force. The second term of the sum on the left of this equation is called the inertial term, and the second term of the right equation part is called the viscous one.

The fluid can be moved by the applied electric field, or externally such as with a water pump and pressure-driven flow. To determine the fluid dynamics and make a flow pattern prediction, one shall take into account the Reynold's number R_n:

$$R_n = \frac{\rho_{FL}u_0 l_0}{\eta}. \tag{2.38}$$

Here u_0 is the characteristic velocity of the fluid and l_0 is the characteristic length scale. If this number is much larger than 1, then the inertial term from the equation above prevails; if it is much less than 1, then the viscous one plays the leading role. In the latter case, the fluid would not experience the movement without external forces. When the fluid follows the streamline of the fluid, the flow is considered laminar. In the case of microchannels, the velocity at the walls would be zero, and the flow would form a parabolic profile. When Reynold's numbers are higher than 1000, the flow becomes turbulent.

When the particle is submerged in the fluid and moves through it, the force opposing this movement is called drag force, and is described by a certain friction coefficient η_D. For a spherical particle in the laminar flow setting this force will be [14]:

$$\mathbf{F}_{\text{drag}} = 6\pi\eta r_p(\mathbf{u} - \mathbf{v}), \tag{2.39}$$

The other important parameter is the Stokes number for the particles, which defines whether or not inertia forces shall be considered when assuming the particle traveling along the fluid streamlines. It depends on the viscous forces, the fluid's characteristic velocity, and the particle's properties, such as density ρ_p and dimensions [43]:

$$St = \frac{\rho_p d_p^2 u_0}{18\eta l_0} \tag{2.40}$$

When this number is smaller than 1, target particles are assumed to follow the fluid flow. To connect this into an equation of particle motion, and take into account the factors mentioned above, one needs Newton's second law. In the case of small particles which are traveling through a laminar flow and possess low Stokes number, that can be simplified as [14]:

$$m\frac{d\mathbf{v}}{dt} = \mathbf{F}_{\text{DEP}} - \eta_D(\mathbf{u} - \mathbf{v}) = \mathbf{F}_{\text{DEP}} - 6\pi\eta r_p(\mathbf{u} - \mathbf{v}). \tag{2.41}$$

Assuming a steady state condition on the equation from above, one other interesting parameter μ_{DEP} , called dielectrophoretic mobility of particles, can be expressed as:

$$\mu_{\text{DEP}} = \frac{\mathbf{u} - \mathbf{v}}{\boldsymbol{\nabla}|\mathbf{E}|^2} = \frac{d_p^2 \varepsilon_{\text{m}} \text{Re}[f_{\text{CM}}]}{24\eta}, \tag{2.42}$$

Different target particles would have different dielectrophoretic mobilities, which affects their movement and enables selective separation. There is a way how to estimate the target particle trajectories in a simplified form. In the case when there are N identical particles and the contribution to the velocity of the particles mainly comes from drag force and DEP (inertia can be disregarded as Stokes number remains consistently below 1), a steady state velocity of each i'th particle can be defined as [23,44]:

$$\frac{\partial \boldsymbol{\psi}_{\text{i}}(t)}{\partial t} = \mathbf{u}(\boldsymbol{\psi}_{\text{i}}) + 2\mu_{\text{DEP}}\boldsymbol{\nabla}|\mathbf{E}(\boldsymbol{\psi}_{\text{i}})|^2, \tag{2.43}$$

where $\boldsymbol{\psi}_{\text{i}}$ is the position vector for i$^{\text{th}}$ particle.

III. Particles in the liquid

Without any external forces, the target particles would be also influenced by two other existing mechanisms such as diffusion and gravity (Figure 2.5). Let us assume

a dilute suspension and look closer to these mechanisms. The text below is mostly based on the sections of the book by Hywel Morgan and Nicolas Green (2003), pages 81-82, ,180-184, which have been shortened and rewritten in the appropriate style and storyline for the thesis [14].

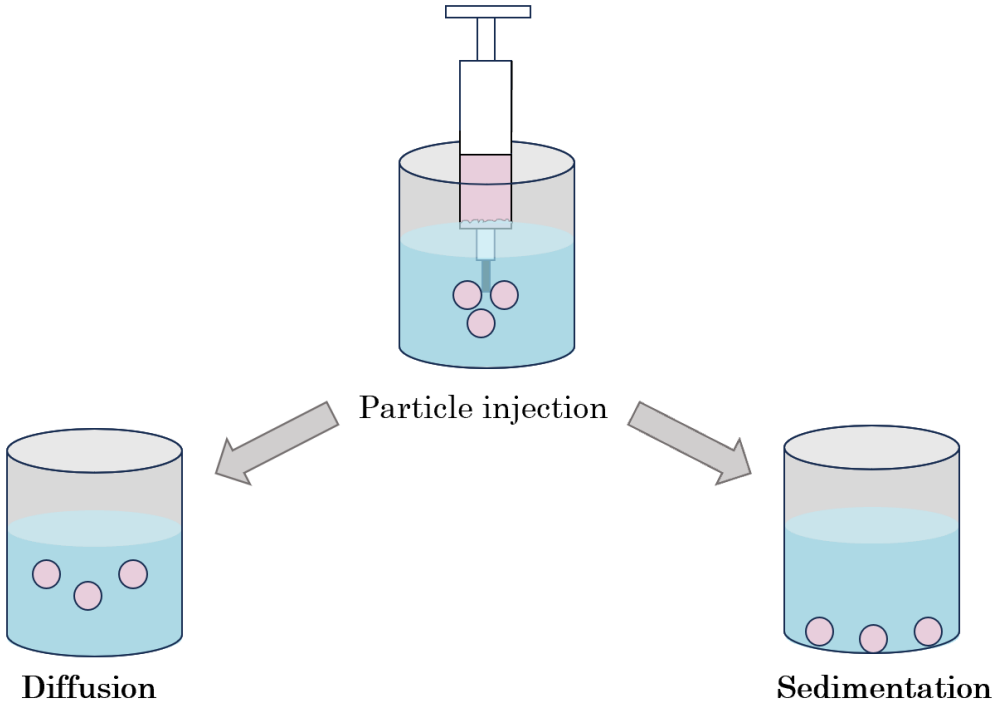

FIGURE 2.5 A simplified representation of two different behaviors of the particles in the suspension: diffusion and sedimentation.

III.1 Particle capture mechanisms

a) Diffusion

The stochastic Brownian motion–diffusion impacts the polarization mechanism of the particles. Diffusion flux is meant to restore the particle concentration to stable equilibrium. During diffusion, the particles move and touch each other chaotically, and transport away from the highly concentrated regions occurs. The diffusion factor is characterized by the temperature, viscosity of the liquid, and particle size.

The diffusion coefficient of a spherical particle in the laminar flow is [14]:

$$D = \frac{k_B T}{6\pi r_p \eta}. \tag{2.44}$$

The relation between convection and diffusion transport processes is described by the Peclet number and with the characteristic velocity as u_0 and characteristic length of the system or size of the particle as l_0, it is [45]:

$$P_{ec} = \frac{l_0 u_0}{D}. \tag{2.45}$$

When it is $\gg 1$, diffusion influence is negligible compared to the advection process [45]. For small particles in the sub-micron range, the diffusion process often prevails and, therefore shall be considered while designing the filter system.

b) Gravity, sedimentation

When the particles have a density higher than the density of the liquid media around them, gravity will act to push the particle down. For example, sub-micrometer range particles that are slightly denser than pure water would only experience movement of a couple of μm in the timeframe of several minutes. For dense particles such as metal ones, this movement would appear stronger.

Sedimentation is a process during which the particles, influenced by gravity and diffusion, are redistributing in the liquid vessel. Due to this process, most particles reside on the bottom of the vessel. Full sedimentation occurs when gravity is more significant than diffusion. The concentration of the particles is decaying exponentially from the bottom of the vessel.

III.2 Particle interactions between the particles

Interaction energy in-between the particles also plays a role in determining their behavior. When it is positive, particles experience repulsion. When it is negative, particles stay with each other. The total sum of the forces is a deciding factor for repulsive or attractive interaction in the particles. It shall be noted that the total interaction relies on electrolyte concentration and the distance between the observed particles.

The text below is mostly based on the sections of the book by Hywel Morgan and Nicolas Green (2003), pages 110-111, 113-115 which have been shortened and rewritten in the appropriate style and storyline for the thesis [14].

a) Van der Waals force

The van der Waals force is a long-range attractive force which occurs between closely positioned particles submerged in the liquid media. The van der Waals force would overpower the repulsive force in short-distance ranges [14].

Generally, the van der Waals force consists of three components: an orientation interaction force, an induction (Debye interaction) force, and a dispersion force. The first one comes from the interaction between the two permanent dipoles; the second one comes from dipole-induced-dipole interaction and is considered not strong enough to influence the orientation of the molecule and the third one exists between atoms and molecules and leads to attraction. The third one is based on the movements of electrons and the generated electric field from the electrons that further leads to induced dipoles. This force is always present and is considered to be the strongest one. Usually, forces from all the atoms are summed up to estimate the interaction between the particles.

The van der Waals forces might lead to target particles agglomerating with each other and thus experiencing alterations in their movement in the electric field. However, van der Waals forces are significant only when there is a short distance between the two particles which shall be in the order of a couple of angstrom.

b) Double-layer force

The repulsive forces are also present for the particles in the mixture. In particular, the repulsive force between the two particles comes from the double-layer interaction. For the case of the two particles in the near, the ions are moving in a way at which the charge neutrality is kept. The electrostatic force remains then zero at the mid-plane between the two surfaces. However, when these particles come closer, the osmotic pressure increases and the concentration of ions changes. The work required to keep these particles together against the counterforce pressure determines the repulsion energy. This interaction energy is decreasing exponentially with the distance in-between of the particles [14].

Therefore, the total energy for particle interaction would be the sum of the van der Waals and double layer contributions. Understanding these energies and surface potentials is important for choosing appropriate parameters for the DEP particle trapping task. Practically, to arrange that target particles experience no adhesion to

the filter, the pH of the media and zeta potentials of the filter and the particles shall be compared and tuned [46].

IV. Other electrokinetic forces acting on the particles

Several electrokinetic effects should be considered along with the DEP force (Figure 2.6). They can be present in the liquid media and influence the target particle when electric field is applied under certain conditions which would be shortly outlined below. The text below is mostly based on the sections of the book by Hywel Morgan and Nicolas Green (2003), pages 123-124, 139-140, 152, 156-159 which have been shortened and rewritten in the appropriate style and storyline for the thesis [14].

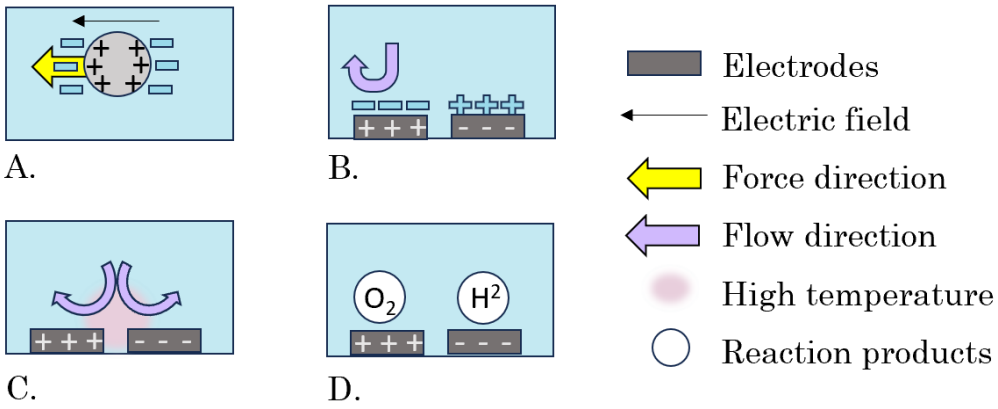

FIGURE 2.6 Electrokinetic phenomena schematics. A. Electrophoresis of a positively charged particle. B. AC-Electroosmosis occurring on the electrodes, accompanied by the formation of DL. C. Electrothermal flow with schematic temperature gradients on the edges of the electrodes D. Electrolysis on the anode and cathode. It shall be noted that the field lines are not depicted here. Parts of this schematic are inspired by the paper from Alinaghi Salari and Michael Thompson (2018) (page 3604, Figure 5[47]).

IV.1 Electrophoresis

Electrophoresis is the movement of the submerged charged target particles in the fluid with the electric field. The key difference with DEP is the requirement for the particle to have the non-zero net charge, which leads to motion also in homogeneous electric fields. The force $\mathbf{F}_{EL}$ that the target particle is experiencing is derived from the Coulomb force Equation (2.1) [14]:

$$\mathbf{F}_{EL} = Q\mathbf{E}. \tag{2.46}$$

Typically, the movement of the particles under electrophoresis depends on the zeta potential of the particle ζ and dynamic viscosity of the fluid η. Increased electrophoretic mobility indicates faster particle movement toward an opposingly charged electrode.

IV.2 Electroosmosis (EO) and induced-charge electroosmosis (ICEO)

A particular flow can occur in the suspension under the DC electric field applied which is called electroosmosis. When the electrical field is tangential to an object submerged in the fluid, the charges in the double layer between the liquid and the object's surface will move, subsequently causing the fluid to move. This flow has a certain property: at the surface of the body, it is null due to the bound charges, however, at the slip plane, it reaches its peak. When the electrodes are in the suspension, the electroosmotic flow would result in ions of liquid moving towards the opposing charge of the electrode.

In the case when the electric field is of AC nature, AC electroosmosis might occur. It is close to zero at very low (<100 Hz) and high frequencies (>100 kHz). That would be the prevailing fluid flow in the region of the low frequencies (<100 kHz) and thus can influence particle mixture transport. At frequencies higher than that, the influence of it would decrease, and the prevailing one would be the electrothermal flow, which would be discussed in the next section [14].

It shall be noted that there is also induced-charge electroosmosis (ICEO) flow. It can involve AC or DC fields and is a specific surface fluid flow which occurs due to the electric field interacting with its induced charges at polarizable matter [48]. The flow occurs near the surface (for instance, the surface of the filter) and thus can highly influence the target particle's trajectories [44]. As a general example, in the case of a metal particle, due to ICEO, the fluid flows are formed at the poles of the particle, and then get released at its equator. The ICEO flow is rotational. The geometry and size of the particle are important. For the case of the dielectric filter with a particular permittivity ε, electric field amplitude E_0 and dynamic viscosity of the fluid η the ICEO would be [44,48]:

$$\mathbf{v}_{\mathrm{ICEO}} = \frac{\varepsilon k^{-1} E_0^2}{\eta}. \tag{2.47}$$

Malte Lorenz investigated the influence of ICEO on pump-driven DEP filtration using COMSOL [44]. The sharp edges of the porous filter matrix became a region of

the maximum ICEO flow, and it was shown that the ICEO flow is highly dependent on the strength of the electric field. In the case of field strengths lower than $75\ \mathrm{kV_{rms}\,m^{-1}}$, the pressure-driven flow prevails, at $75\ \mathrm{kV_{rms}\,m^{-1}}$ the ICEO and pressure-driven flow velocities were found to be of identical order.

IV.3 Electrothermal flow

The electrothermal flow exists when temperature gradients are present in the given fluid. One way of generating them is through the process of Joule heating [14]. The temperature distribution is assumed to be steady-state in the case of DC or high AC frequencies. A temperature gradient occurs when power dissipation happens in the surrounding media under the applied electric field. The velocity of the electrothermal flow is dependent on the rise in temperature in the media. When the conductivity and the magnitude of the electric field are high, it would also increase thermal flow. For the low-conductive fluids used in this thesis, electrothermal motion has a negligible impact on the flow behavior. As follows from the review paper from Xiangchun Xuan (2022), ICEO flow is said to be the main one in low-ionic-concentration fluids for the non-pressure driven flow, and electrothermal motion is taking the central role in high-ionic-concentration fluids at high conductivities [49]. However, these assumptions shall be carefully revised when considering a particular particle mixture.

IV.4 Electrolysis

Electrolysis is a phenomenon that occurs when, under the applied energy of a DC electric field, molecules of water split into oxygen and hydrogen. The process can generally be described as [50]:

$$\mathrm{H_2O} + \mathrm{energy} = \mathrm{H_2} + \frac{1}{2}\mathrm{O_2}. \tag{2.48}$$

In low-conductive liquids, the process takes place on a very small scale.

The text in this paragraph is mostly based on the paper of Aytug Gencoglu et al. (2011), selectively shortened and rewritten in the appropriate style and storyline for the thesis [51]. Several scenarios for ionic charges might occur, one of which is conversion into electronic charges. During that, the H^+ ions and oxygen are appearing on the anode (positive electrode) and OH^- ions and hydrogen on the cathode (negative electrode). Subsequently, the anode's pH decreases, and it is increasing on the cathode. Electrolysis can lead to pH gradients in the suspension

and also introduce a change in the ion concentration, implying a change in the gradients in the electric field [52]. Generally, application of AC fields with frequencies are higher than the charge relaxation frequency, prevent the occurrence of the electrolysis [53,54].

V. The DEP filter characterization and main terms used in this thesis

Several parameters shall be taken into account to describe the performance and working principles of the DEP filter. The most of the aspects described in this section are a rewritten copy of the text of the author's publication from 2023, changed in the appropriate style for the thesis (CC BY 4.0) [1].

Particle trapping without DEP in this thesis is labelled as mechanical trapping. Mechanical trapping occurs, for instance, when dead-end pores are occurring in the filter or due to particles being majorly influenced by electrostatic or van der Waals forces [1,55]. Normally, it is possible to determine experimentally the mechanical trapping of the filter by flushing the suspension through it without applying an electric field and measuring the concentration difference before and after the filter.

The separation efficiency of the particles in the DEP filter is considered as a ratio between trapped and normally present particles in the filtration system. That can be expressed through the particles' concentrations in the system (depending on the type of the particles, there would be different methods to experimentally determine this parameter). In the case of a DEP experimental measurement, a separation efficiency in % can be seen by comparing the concentrations of the target particles at the outlet of the setup. For the concentration of particles without an electric field c_0 to the concentration when the electric field was applied c_e [1,21]:

$$\text{Efficiency (\%)} = 100 - \frac{100 c_e}{c_0}. \tag{2.49}$$

One other important parameter for the characterization of the filter performance is a recovery rate of the filter. It determines how many particles are getting recovered, derived from the concentration ratio c_r of released particles (particles travelling through the system from the moment when the electric field was off), and concentration c_tr of trapped due to DEP particles [44]:

$$\text{Recovery (\%)} = \frac{100\ c_\mathrm{r}}{c_\mathrm{tr}}\ . \tag{2.50}$$

Filter capacity is considered a parameter that reflects how much concentration of the particles the filter can hold before it fails. Target particles would occupy the regions of the filter where DEP manipulation is taking place, and that would thus, over time, reduce the filter performance [21].

Throughputs in this thesis refer to volumetric flow rates q_{flow} at which the pumps operate. This is generally related to the area of the cross-section of the filter, through which the suspension is going (S_F) and the speed of the flow u (in m/s):

$$q_{\text{flow}} = u\, S_F. \tag{2.51}$$

In this thesis, the filter matrix refers to a bulk porous filter located between the electrodes, and the term matrix emphasizes the geometrical aspects of the filter. These aspects are: porosity (%), permeability (m^2), pore-to-window ratio (reflecting, how much opening the specific pore has), mean sphericity of the pores, tortuosity, specific surface area (mm^{-1}), and particularly in the case of packed beds filters: angularity of the grains and a change in the distance from the center of the gravity of the grain (particle) in µm.

As was already mentioned in the supporting information in the author's paper from 2023 and is rewritten here in the style appropriate for the thesis in the next three paragraphs: porosity, permeability and sphericity take several assumptions to define them [1].

The porosity of the sample primarily relies on the packed bed's packing and the grains' shape [56]. Porosity can be determined by dividing the total pore volume by the total volume. For example, while considering alternative materials to the glass beads for the packed bed filter construction, grained silica (sand) can be used. Literature estimates the porosities of the sand filter materials to be around 40% [57]. Regarding the glass beads as a packed bed filter, loosely packed monodisperse spheres possess a porosity of around 41 % [58].

Based on Darcy's law, one can determine the permeability. When a linear dependence between the pressure gradient and the volumetric flow q_{flow} is considered, then the relation is [59]:

$$q_{\text{flow}} = \frac{\kappa_p S \Delta\Pi}{\eta L}. \tag{2.52}$$

Where among the parameters q_{flow} is the flow rate, κ_p is the permeability coefficient, S is the cross-sectional area, $\Delta\Pi$ is the pressure drop, η is fluid viscosity, and L is the flow length of the porous filter. Permeability affects the volumetric flow rate, so this value is also vital when comparing the DEP performance of different porous filters.

The mean sphericity of the pores can be determined from the sphericity of individual pores and expressed analogously to $36\pi\frac{V_\mathrm{p}^2}{S_\mathrm{p}^3}$. In this formula, S_p denotes the surface area of the pore and V_p represents the pore volume [60]. The sphericity can reach a maximum value of 1, indicating a perfectly spherical pore.

Tortuosity is used in this work in its geometrical sense and characterizes the path of the particles through the filter. Differences in tortuosity might influence the residence time of the target particles traveling through the filter [61].

The term "angular" is related to the sharpness of the corners shown by individual grains which are forming the packed bed filter [62]. In this thesis, angularity is used solely as a qualitative property, further characterized by a property of the grains called a variation of a distance to the center of gravity. The distance to the center of gravity is a geometrical property and represents the measurement from the gravity center of the grain (particle) to its surface. In the case of the perfect spherical grain, this distance does not vary over the different surface points. This variation of the distance is a factor, helping to distinguish different grain morphologies in this work.

The term surface morphology in this thesis refers to a combination of properties, such as the angularity of the grain, pore shape, 3D shapes of the grain, and its surface roughness. It is also given only in a qualitative sense here.

Chapter 3: State of the art in the dielectrophoretic filtration

This chapter aims to provide the reader with a comprehensive historical background of dielectrophoretic filtration from the beginning of the 20th century until now. It is divided into two parts. The first part gives the reader a short overview of the general potentials of this technique and mainly focuses on the niche application of non-biological separation of DEP. The second part reviews in detail dielectrophoretic filtration – up to 2024. A table with an overview of the literature is also provided at the end of this chapter and is a copy from a part of the submitted author's review paper from 2024 [63].

I. A short introduction to the field of interest

As detailed in the theory section, DEP is the movement of specific target particles in an inhomogeneous electric field. The dielectrophoretic effects have a wide range of potential applications, including the enrichment of target particles, particle or cell analysis, particle filtration, and the separation and purification of liquids.

The term "DEP" itself was first introduced by Herbert A. Pohl in 1951, who studied the behavior of carbon particles in an inhomogeneous electric field created by electrode design in a petri dish under AC and DC fields [5]. In 1966, another pioneering work was published by him a s a first author, where he demonstrated the separation of dead and live cells using dielectrophoresis [64]. This paved a way for further cell separation and characterization application development and many other researchers have followed up on this one [65–69]. In 2016, Michael P. Hughes gave a good overview of the literature on DEP applicability for cell analysis [70]. He pointed out some market devices capable of collecting bacteria or performing a complete DEP analysis on the cells for the scan of their properties. Another great review on this topic was published in 2020 by Benjamin Sarno et al., where cancer and blood cell manipulations and differentiations by DEP are thoroughly addressed [71] .

Most recently, in 2022, Taher Ghomian and Joshua Hihath highlighted that developments in DEP and several other broad fields are accelerated, such as medical diagnostics or material characterization [72]. They also note that they see a future in

the straightforward fabrication of DEP devices and their potential to handle increasing volumes of samples.

DEP is mainly connected to particle, cell or component manipulation. A term of DEP separation targeting particular particle properties is quite broad and has to be classified further on. For this purpose, several selection criteria of the manipulation properties of the target particles can be addressed [52,73,74] (Figure 3.1).

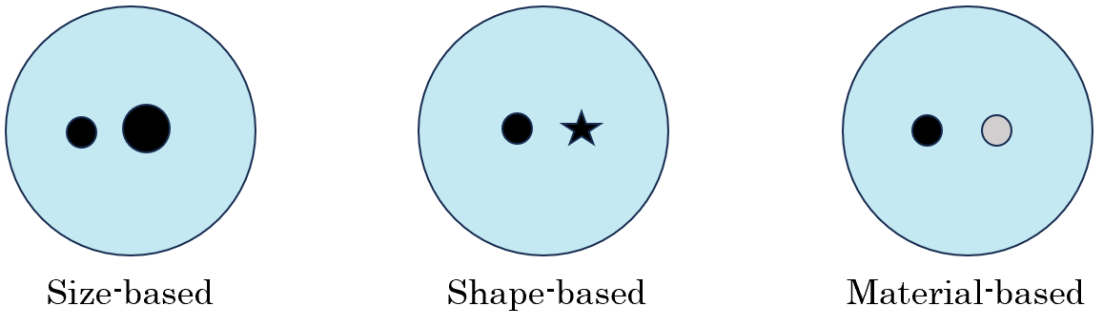

FIGURE 3.1 Three different selection criteria of the target particle separation.

Firstly, the particle fraction can be separated by their size. In 1998 Xiao-Bo Wang et al. discussed the separation of polystyrene beads in different sizes (6, 10, 15 µm in diameter) [75]. In 2019, Qiaoying Chen and Yong J. Yuan also mentioned in their review the size-based separation of polystyrene microparticles, which are often used as target particles in the performance characterization of DEP filters [76]. In some occasions, with cells, the size is a factor that indicates non-healthy versus healthy mammalian cells, as was noted by Peter Gascoyne et al. in 1992, showing the DEP separation from the mixture [77].

Secondly, dielectrophoresis can also target particles based on shape in some cases. One case would be a study by Reza Riahifar et al. in 2011, where a separation of ZnO rod and cubic-shaped particles was investigated with the help of DEP [78]. There, the rod-shaped fractions were trapped in the array of the electrode gaps. In the biology field, shape is also acknowledged as an important factor. 2014, John DuBose et al. noted that the shape of the particle is a vital indication of the cell life cycle stage and can also be used for differentiating rod-like bacilli or spherical cocci [79]. The group separated peanut and spherical-shaped particles using DEP. In 2022, Laura

Weirauch et al. demonstrated selective separation of ellipsoidal and spherical polystyrene particles [22].

Thirdly, material-based separation of particles of the same size can also be handled by dielectrophoresis. A particular relevance can come from the separation of the electronic scrap, where there is a demand to target the noble metals, as was mentioned in the introduction of this thesis and also in the review of Kui Huang et al. in 2009 [80]. In 2013, Noriaki Sano et al. showed a separation of tungsten carbide particles from a mixture of diatomite by a mesh-electrode-based DEP separator [81]. In 2008, Fei Du et al. published a paper about separating gold particles from a mixture of gold, zircon, and quartz using DEP [12]. There, gold particles formed chains along the electric field lines.

The author is particularly interested in the broad field of material-selective separation applications. One of the exciting tasks in this category can be tailored towards using DEP as an additional recycling procedure for lithium-ion batteries (LIBs). A good overview of this motivation was presented in the author's second paper from 2024 (CC BY 4.0) and is rewritten here in the style appropriate for the thesis [24]. Generally, lithium metal oxides serve as cathode active materials. A requisite for graphite in LIB production exceeds that of lithium 10-20 times, and this graphite is an active anode material [82]. For a broader picture, pyrometallurgy, hydrometallurgy, and direct physical methods are widely used for LIB recycling [83,84]. Two processes are mainly engaged in recovering the dominating cathode components: hydrometallurgy and pyrometallurgy. Pyrometallurgy is a solution that does not necessitate pre-treatment but is afflicted by significant energy requirements. It results in environmental contamination due to the emission of toxic gases occurring in the process. Further, to establish a complete recovery, a hydrometallurgical step needs to be accompanied by pyrometallurgy to process the alloy and additionally a wide usage of chemical reagents is connected to it [83,84]. At the same time, graphite is mainly not targeted and vanishes without the proper recovery method in these processes. The utilization of particle technology is a center of direct physical recycling processes, and the active materials from the cathode and anode are getting separated; nonetheless, the globally used methods are not yet present. Dielectrophoretic filtration, in principle, can be applied to address the parts of this task, which further would be researched as a proof-of-concept in the results part of this thesis.

Dielectrophoresis, in general, can go in hand with other forms, such as traveling wave dielectrophoresis, electrorotation, or even a combination with optical tweezers [14,85,86]. Such combinations are not covered further in this thesis.

With these classifications mentioned, the reader is invited to proceed further to a more detailed historical outline of the developments in DEP filtration in the non-biological field.

II. Dielectrophoretic filtration: back in time

As was already mentioned in the theory, a required electric field inhomogeneities can be established by several means: by the electrodes – known as electrode-based (eDEP) or by the porous dielectric structure, squeezed in-between of the electrodes – referred to as insulator-based (iDEP, see also Figure 3.2). To understand the mechanisms behind this, the author suggests a review by Victor H. Perez-Gonzalez from 2021, which compares the differences well [54].

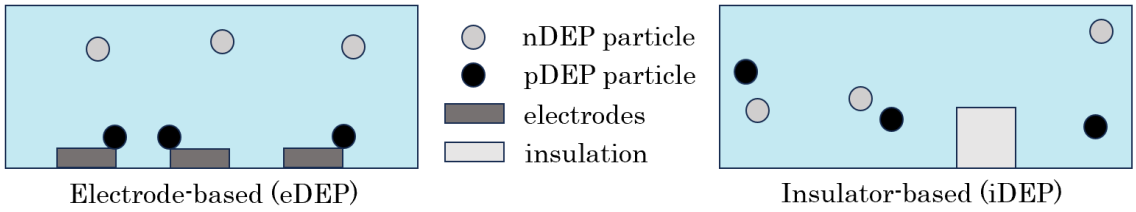

FIGURE 3.2 Schematic of the eDEP and iDEP approaches. This schematic is a created by the author drawing based on the Figure from the book chapter by Matthaus Barasinski et al. (2022) (Chapter 7, Figure 7.5 [87]).

Dielectrophoretic filtration, a topic of this thesis, belongs to the iDEP section and is distinguished by using bulk porous media as a filter. It operates in the pressure-driven flow in the liquid-based media, in which the target particles are undergoing separation.

Dielectrophoretic filtration can be used for non-biological purposes. In 1981, I. J. Lin and L. L. Benguigui noted that dielectric separation can also be applied to remove contaminations from non-conductive or conductive liquids, selectively remove the noble metals from minerals, and increase the noble metal concentrations or purification of the oils [88]. In 1982, in the "Dielectrophoretic Filtration of Nonconductive Liquids" review, they further elaborated that when the dielectric permittivity of the target particles is higher than the one of the liquid and that these

particles then would be attached to the high gradient regions of the filter [89]. These scientists saw possibilities of the future of dielectrophoretic filtration in the purification of non-conductive liquids from metallic, plastic, and ceramic impurities.

Beginning in the 1950s, there was a boom of works that share several common vital elements: the inhomogeneous electric field is generated using scattering on a porous, often a packed bed filter, and the filter is most often filled with the oil liquid media with DC field applied across the structure. This filter appeared in many forms, such as open porous foam, glass packed beds, or even stacked textile fibers. The pores of this filter were usually much larger than the filtered particles, so the mechanical filtration was kept to a minimum or not present at all, which allowed for selectivity of the separation, and the filter itself had less pressure loss with the larger pores. Many of these patents concentrate on addressing particle contamination, introducing the recovery process of the captured particles, or testing several filter design configurations. The author participated a more comprehensive overview concerning the usage of DEP filtration on biological and non-biological particles with Mary Clare O'Donnell and Georg Pesch in 2024 [63]. Here, the author summarized a shorter historical timeline of these patents and publications, centralized only around the DEP filtration of non-biological particles. The author would like to note that in this historical overview, some old patents often used imperial units, which can be translated to the thesis units by employing the relation of 1 inch = 2.54 cm.

II.1 Mostly chronological timeline of DEP filtration

One of the first patents in 1950 was submitted by Garnet Philip Ham and Robert Bowling Barnes who proved the removal of copper at the DC regime with the granular material filter [90]. It was related to the purification of petroleum distillates, which were becoming unusable in the case of the present gum formation. An anion-active resin was utilized as a filter in this case. The authors offered to regenerate the active resigns by flushing a solution of organic bases and watering through them. That was the beginning of the industry boom of DEP-based filters.

An interest in using irregular grains as a packed bed filter was raised in several other patents later on. In 1951, a patent by Hamlin Henry Frederick and Hoffman Machinery Corporation demonstrated that the purification of lubricating oil from carbon particles could be achieved [91]. A filter was assembled of loosely packed dielectric, consisting of fibers (such as wool). The electric field used to remove the

particles was DC with very high voltages (up to 10 kV). Large surface area and loose packing were the requirements for this filter configuration, but it was also noted that granular materials are becoming a good alternative. In 1968, in the patent from William L. Shirley and Petroline Corporation, was claimed to be successful to remove particles electrodeposited from open-porous polyurethane foam [92]. It was noted that the pores inside the filter can be so large that they possess little to zero mechanical trapping. The invention also mentioned using sand, gravel, and other sintered materials or natural fibers packed as filters. The electric fields in use were still quite strong; the applied voltage in the oil was up to 44 kV per inch. In 1977, another patent claimed an electrofiltration system that does not possess problems such as pressure buildup electrical arcing in the bed—operating at 40 kV per inch in DC field, as a filter media options were presented furnace slag, sand, gravel, limestone, crushed glass, glass beads, ceramics and minerals with crystalline silicon dioxide, in the dimensions ranges of 1-13 mm [93]. In 1979, another packed bed filter with grains was used by Joel V. Landis [94]. He was utilizing flint and fused quartz. He applied DC, 20 kV per inch, and had a stage of application for an aqueous alkali reagent in the process. Concerning the application, he purified non-petroleum oils by removing solid adsorbents. Interestingly, he notices the importance of the filter material possessing "relatively discontinuous surfaces," such as crushed flint rock.

A property of the resistivity of the filter material was noted to play a role in the separation efficiency in several patents, utilizing oils as a liquid media. In 1967, in one of the inventions there was an improvement on the electrodes, operating in oils (for example, on lubricating ones or fuels) [95]. In that invention, the space between the electrodes was stacked with multiple layers of filling with an example of sheets of glass or synthetic fibers. It was mentioned that the filter materials with higher resistivity produced better filtration results. The targeted particles were > 5 μm, in the nature of dust or metals (like iron oxide) or non-metallic ones. Several other patents report a similar observation. In 1975, was presented an approach of mixing the filter beads with high and low resistivity [96]. It showed that it was proven to be very effective in the filtration of conductive particles (around 5 μm or less) in high resistivity oil. As a filter ceramic bead (for instance, mullite) of high resistivity was used, mill slug river gravel was also given as a possible alternative. The crucial step was noted to ensure that the filtration media has a lower electric resistivity than the filter media because it improved the reusability of the filter and prolonged its

lifetime. In 1993, inventors from General Atomics claimed another interesting patent [97]. There, the particles of interest were catalyst fines in hydrocarbon oil. The invention had a comparison of a performance of the glass beads made of different materials, such as potassium oxide and sodium oxide, and the main observation was that potassium oxide ones, with particular electrical resistance, contributed to the prolonged lifetime of the filter.

Different packaging options or arrangements of the packed bed have been considered over the years. In 1974, in one of the inventions was mentioned a purification of solids from organic liquids and with a particular emphasis on the packed bed voids [98]. An interesting observation was that void in the packed bed glass beads configuration around 30-40 % gave the best results in the particle removal structure. The target particles were iron oxide (for instance, coming from the rust) or also non-metallic ones and were around 1-100 μm with the used voltages to capture the particles in the DC regime, 5-50 kV per inch.

An importance of a suitable cleaning-up process and reusability of the filter was highlighted in further other works. In 1977, a filter construction in one of the patents did not require disassembling for the cleaning-up process and was claimed to be effective with backflushing [99]. The invention used a central tubular electrode with a concentric cylindrical outer electrode and a radial flow pattern that allowed for increased flow rates. With 5-20 kV per inch operating voltages on the liquid of high resistivity, a filtration of finely divided particles, some of which were electrically conductive, was successfully achieved. As filter options were used glass beads, sand, gravel, etc.

Some studies also included additional theoretical analysis or state-of-art showing the perspective of the field. In 1981 by Peter Dietz was published a theoretical investigation focused on the efficiency of such a packed bed configuration [100]. The results showed conditions for trapping of particles that possess finite size under the consideration of low Reynolds number. The modeling was done in a way that the grains of the packed bed were represented as the liquid around each spherical granule, and the amount of void present in such a cell correlated with the localized void in the packed bed. In 1982, I. J. Lin and L. Benguigui published two interesting reviews, one of which was already mentioned above [89,101]. The components of dielectrophoretic filtration were discussed, including the applied electric field and its parameters, properties of the particles and liquid media (such as dielectric

constants), and experimental parameters such as flow. They presented a very systematic approach, studying the DEP filtration phenomena in more and more depth.

An importance of the cost efficiency of the process and usage of lower kV was highlighted as well. In 1983, one invention described the low conductive liquids and removal of pipeline dust where it was noted that higher kV results in very high costs for the process [102]. The filter in this invention was operating at 1-60 kV per inch [102].

One interesting publication from I. J. Lin and L. Benguigui (1985) acknowledged a successful filtration in a conductive liquid with the usage of AC fields at 4kHz [103]. The researchers took a filter consisting of beads in the sizes of mm made of $BaTiO_3$ with a very high dielectric constant. The particles in question were Polyvinyl chloride ones. To tune a conductivity of the medium, they used pure kerosene and a mixture of it with isopropanol. Implementing the AC fields solved the problem of the dielectric constant of the investigated particle being higher and the conductivity being lower than those of the surrounding media in DC fields. They also interestingly observed that the density of the particles influences the drag force and the polarizability of the particles (which, in the case of the light ones, becomes high under certain conditions).

Further exciting investigations of the influence of the liquid media and a motivation to arrange the filtration of the sub-micron particles continued. In 1995 in the article by Warren Sisson et al., a demand to remove the target SiO particles in submicron or even smaller range was accommodated for [104]. A DC field of a strength of 8 kV/cm was applied across the meshed electrodes, and glass beads of 1 mm served as a filter. The experiments showed the effective removal from tert-Amyl Alcohol, which possesses a low dielectric constant. With the higher temperature of the liquid, the drag force was getting lower due to lower viscosity, which resulted in the better separation. In 2000, in the patent by Roland Halm et al. from Dow Corning Corporation was made the effort to remove tiny particles (0.01 μm) from silicon fluids [105]. It was arranged with DC field, utilizing 1-35 kV per inch, with throughputs up to 70 mL/min in a liquid of a relatively high electrical resistivity (1×10^8 Ω·cm at 125°C). It was noted that the separation efficiencies were higher at high liquid temperatures. In 2003, Richard Wakeman and his colleague studied the separation in the filter made of glass bead matrix of 500 μm in diameter with the field at 10 kHz going up to 11 kV/cm [106]. They demonstrated that the high viscosity of the liquid

leads to an increased drag force. Polyvinyl chloride (PVC) and air-conditioning dust were used as target particles dispersed in a hydraulic fluid, Tellus 37. The particles had mean diameters around 28 and 10 μm, respectively. A maximum separation efficiency achieved was 65 %, with a flow rate of just 0.09 mL/min.

The design parameters of the packed bed filter were researched further. In 2019, in the study from Zhang Zhe et al. was acknowledged that the filler diameter decreased the process's efficiency [107]. The filter in use was glass beads one, 10 mm in diameter, studied in four stacking manners. They considered a face-centered cubic manner to bring the best results in the heat-conducting oil. There was also an interesting note that both electric field strength and the uniformity of the electric field play a crucial role in the separation process. In 2020, Qiang Li et al. published a paper investigating glass beads as a filter for catalytic particles in DC mode [108]. There, he noted that the maximum of the applied electric field was occurring when the glass beads were located parallel to the electric field lines. It was also found that the strength of the electric field was maximum for the case of the ellipsoid packing of the filter when the ratio of the short to long axis was 0.4. In 2023 and 2024, Qiang Li et al. proceeded with their studies of the spheres in the packed bed configurations further, which would not be discussed here in details [109–112].

Other media, such as meshed filters or sponges, have further used in other recent works. In 2011, Yueyang Shen et al. presented a work that had a filter as a construction of sheets of woven metal wire mesh with other sheets made of insulating woven polymer wire mesh positioned in between [113]. This configuration generated a highly inhomogeneous electric field, which also enabled the operation of DEP for high throughputs (maximum was around 120 mL/min at which trapping still took place). The particles of interest were spherical glass beads or silicon metal powder filtered in the oil. In 2022, Laura Weirauch et al. presented a mesh-based DEP filter which showed a shape-selective sorting of ellipsoidal and spherical polystyrene particles at high throughputs (120 mL/h) in water in AC mode [22]. Also in 2022, a very interesting pre-print was published by Md Nazibul Islam and Zachary Gagnon, who claimed that dielectrophoretic filtration could be performed with a paper bag as a filter which possesses “naturally occurring insulating porous structures” [114].

Summing up the discoveries, DEP filtration was broadly applied with various filters in R&D to purify and separate particles in various oils. High voltages, usually in DC mode, were applied up to hundreds of kV ranges. For the purification tasks carried

out in water, significantly lower AC-based voltages were in use. At the same time, high throughputs of the process were of interest, and removing sub-micron particles remained an ongoing challenge. The other important emphasis was on filter reusability and recovery of the particles from it.

II.2 Selected contributions to iDEP and dielectrophoretic filtration from the group

One of the advantages of using DEP for separating microparticles is a possibility to recover these particles after the separation. The group of the Prof. Dr. Thöming at the University of Bremen looked closer at the quasi-two-dimensional post array configuration in microfluidic iDEP [33]. In 2014, Georg Pesch et al. demonstrated this recovery advantage and used polyethylene foam with irregular pore structures and varying mean pore diameters [33]. He resuspended the target particles, in this case layer-by-layer (LbL) assembled nanocapsules being 340 nm diameter, by DEP filtration with maximum separation efficiencies of 65 %.

Further on in other later publications of this group, it was shown that sharp edges of the posts led to high electric field gradients. In particular, in a paper from 2016, Georg Pesch et al. investigated rhombus and circular-shaped posts [115]. He categorized the structures based on their geometry and cross-section. One of the main findings was that the high gradients formed around the sharp edges of the posts had a smaller area of influence than the gradients of the circular posts. In 2017, Georg Pesch et al. established design rules for the efficiency of the DEP filter, combining the experimental variables, such as flow rate and strength of the electric field, with the filter variables, such as the size and geometry of the obstacles [116]. In 2018, the study by him verified that these relations experimentally apply in the polydimethylsiloxane (PDMS) microchannels[23]. That study also mentioned that dielectrophoretic filtration has a potential to recover noble metals from dust waste in water.

Next to that, high-throughput possibilities in DEP filtration were addressed in several papers, which utilized dielectrophoretic filtration with a porous dielectric filter positioned in between the electrodes [21,22]. In 2020, Malte Lorenz et al. showed that some of the above-mentioned established rules from the microchannels can also be translated to the macro-porous sponge structures [21]. He used a bulk DEP filter, such as a monolithic alumina sponge which was implemented as the porous filtration matrix, and studied a contribution to the DEP trapping to several factors such as the

pore size, flow rate, or applied voltage. He also used glass beads to separate polystyrene and graphite particles in water at 1-15 kHz at 300-600 V pp. There, the glass beads overall were demonstrating lower separation efficiencies than the sponge filter structure, which was attributed to their inverse pore geometry. However, it shall be noted that the porosities of the packed bed and sponge filters were not identical in those tests.

The pore structure of the filter contributes significantly to changes in the electric field. From the DEP theory and the papers above can be highlighted that a gradient of the electric field squared influences DEP force, and a porous structure's design highly determines the dielectrophoretic filtration efficiency. Therefore, this thesis aims to contribute to systematic understanding of the influences of the pore geometries and pore shapes, as is further elaborated in Chapter 4.

II.3 A table-summary of the selected works in non-biological DEP filtration

Content in this table is an identical copy of the shortened table from [63] with minor additions and is based on the review paper in which the author participated in 2024.

Year	Authors	Particles	Medium	Insulating Structure	Voltage (kV)
1950[90]	G.P.Ham, R.B.Barnes	Copper	Hydrocarbons	Anion active resin	0.1-2
1951[91]	F.H.Hamlin	Laundry dirt	Stoddard solvent	Glass wool	10-15
1967[95]	L.C. Waterman, A.D.Franse	Dust, metals (iron oxide), or carbon	Oil (lubricating oils, fuels, hydraulic oils. etc.)	A porous material in sheet form	≈15
1968[92]	W.L.Shirley	Oil contaminants	Jet fuel	Poly-urethane foam	44
1974[98]	A.D.Franse	Metallic compounds, or carbon	The organic liquid	Glass beads, slag, river gravel, etc.	5-50
1975[96]	G R. Fritsche, L.W.Haniak	FeS, Fe_2O_3	Hydrocarbon oil	Glass/ ceramic beads, river gravel, etc.	
1977[93]	S. Oberton, Petrolite Corporation	Hydrogenation catalysts	Non-petroleum organic liquids	Crushed flint, marine sand, river gravel	20-40
1977[99]	J.H. Crissman, G.R.Fritsche F.B.Hamel, L.W.Hilty	FeS, Fe_2O_3	Hydrocarbons	Glass beads	20-80
1979[94]	J.V.Landis	Solid adsorbent, catalyst, etc	Mediums like coconut oils or fats.	Flint, garnet, granite, fused quartz.	20
1981[100]	P.W.Dietz	Dust particles	-	-	-
1982[89]	L.Benguigui, I.J.Lin	MgO, Cu, ilmenite, PVC	Kerosene	Glass beads	2-12

Year	Authors	Particles	Medium	Insulating Structure	Voltage (kV)
1982[101]	I.J.Lin, L.Benguigui	PVC, Cu	Kerosene, propanol	Glass beads	2-8
1983[102]	F.D. Watson, W.D.Mayse, A.D.Franse	LPG Pipeline dust	Absorption oil, jet fuel	Polyurethane foam	1-60
1985[103]	I.J.Lin, L.Benguigui	PVC, Polyvinyl Chloride	Pure kerosene and a mixture of kerosene with isopropanol.	Beads of BaTiO3	2-3
1993[97]	G.R. Fritsche, R.S.V.Bujas, G.C. Caprioglio	Catalyst fines	FCC oil	K_2O/Na_2O glass beads	30
1995[104]	W. G. Sisson, R.R.Brunson T.C.Scott, M.T.Harris, J.L.Look	SiO particles	test-Amyl Alcohol	Glass beads	0-25
2000[105]	R.L.Halm, K.Hayes	KCO_3, $KHCO_3$, KCl, MgO, $CaCO_3$	Siloxanes, silicon-containing compounds	Glass beads	1-35
2003[106]	R.J. Wakeman, G.Butt	PVC, AC dust	Tellus 37 oil	Glass beads	8-14
2011[113]	Y.Shen, E.Elele, B.Khusid	Glass beads, silicon, Al2O3	Engine oil	Poly-propylene mesh	0.22-0.44
2014[33]	G.R.Pesch, F.Du, U. Schwientek, C. Gehrmeyer, A.Maurer, J.Thöming, M.Baune	Silica nanocapsules	Poly-electrolyte, NaAc buffer	Polyethylene	200 V_{rms} at 200 kHz

Year	Authors	Particles	Medium	Insulating Structure	Voltage (kV)
2018[23]	G.R.Pesch, M.Lorenz, S.Sachdev, S.Salameh, F.Du, M.Baune, P.E.Boukany J.Thöming	Polystyrene, yeast cells	H_2O	Alumina-mullite ceramic	150-300 V_{rms}, 15-30 kHz
2019[62]	Z.Zhang, Q.Li, Z.Wang, Z.Wu, A.Li, L.Guo	Catalyst particles	Conducting oil	Glass beads	5-11
2020[108]	Q.Li, A.Li, L.Guo, H.Cao, W.Xu, Z.Wang	Catalyst Particles	Conducting oil	Glass beads	15
2020[21]	M.Lorenz, D.Malangré, F.Du, M.Baune, J.Thöming, G.R.Pesch	Polystyrene, graphite	H_2O	Alumina-mullite ceramic	150-600 V_{rms}, 1-15 kHz
2022[22]	L.Weirauch, J.Giesler, M.Baune, J.Thöming	Polystyrene	H_2O	Poly-propylene mesh	176 V_{rms}, 10-65 kHz
2022[114]	Md N.Islam, Z.Gagnon	Polystyrene	H_2O	Fiberglass fibers	100 kHz, 2-10 V_{rms}
2023[111]	Q.Li, H.Cao, Q.Qiu,L.Guo A.Li, W.Xu, Z.Wang	Catalyst particles	FCCS	Glass beads	2-12
2023[1]	M.Kepper, Md N. Karim, M. Baune, J.Thöming, G.R.Pesch	Polystyrene	H_2O	Crushed glass, glass beads, sand	300-600 V_{rms}, 1 kHz
2024[24]	M.Kepper, A.Rother, J.Thöming, G.R.Pesch	Graphite, lithium iron phosphate	H_2O	Sand	300-500 V_{rms}, 15 kHz

Chapter 4: Motivation, leading questions and structure of the thesis

A global motivation of this thesis is to present a new understanding of modifications of the dielectrophoretic filtration's bulk filter matrix in the AC regime, with a focus on the usage of cost-efficient packed bed filters for material-selective separation. Furthermore, the goal is to push the DEP field toward applied research. The results presented in this thesis are divided in three main parts. Each part is presented with its motivation, leading question (hypothesis) and the scope of the conducted work.

The first part, titled "**Chapter 5**. Topological considerations: macro filter geometry changes", investigates whether findings from microfluidics apply to macro filters in terms of geometry changes and their impact on dielectrophoretic (DEP) filtration efficiency. This is motivated by several aspects. First of all, it is known that sharp edges cause larger electric field gradients [115,116]. In these papers, the geometrical aspects of the filtration matrix were already investigated but only at the microfluidics scale in the context of insulator DEP. Therefore, an aspect of the pore geometry changes and influence of the morphology of the bulk filters which have similar porosities was not further analyzed, to the best of the author's knowledge. Secondly, several old patents from 1950s have already mentioned that using gravel, sand, and crushed glass in a packed bed filter configuration is possible. Notably, in 1977 Oberton Serafin Bess and Petrolite corporation in the patent mentioned an opportunity of employing crushed materials, which led to better trapping, and this interest to grain filter materials was also pointed out by Joel V. Landis in 1979 [93,94]. Still, there was no elaborated analysis and comparison of the filter performances for this suggestion. ***The leading question of this chapter is whether shape of the pores between grains in a packed bed configuration influences DEP filtration.*** Concave filters with polystyrene microparticles are used to investigate how geometric modifications of the filter matrix affect separation efficiency in the macro filters.

The second part, titled "**Chapter 6**. Selective Separation: lithium-ion batteries", comes from a motivation to address the use dielectrophoretic filtration for a societally relevant problem. ***The leading question is if dielectrophoretic filtration can be applied for battery recycling.*** As partially was already noted by the state of the art,

recycling of lithium-ion batteries (LIB) suffers from several problems, such as low recovery rates and loss of graphite. DEP is capable of material selective separation, for example separation of conductive from non-conductive particles. In this part the isolated trapping of graphite from a mixture consisting of graphite and uncoated lithium iron phosphate (LFP) target particles is shown.

The third part is titled "**Chapter 7**. Modified porous filter: conductive particles", and is a complimentary chapter. In conventional DEP filtration, typically only the material boundary between the dielectric material and the liquid scatters the electric field. However, if a filter is hybrid such as consisting of three different materials, where one material is more conductive than the liquid (such as deionized water), and the other one is less conductive than the liquid, there are three kinds of boundaries that could cause more field inhomogeneities, potentially enhancing the separation efficiency in the DEP. This configuration was already noted by Mario A. Saucedo-Espinosa in 2017 for microfluidics [117]. ***The leading question is whether the separation efficiency of DEP filtration of particle mixture in very low frequency AC fields can benefit by adding conductive sub-micron particles (inclusions) as a part of the porous sponge-like filter.*** The chapter discusses the feasibility of embedding conductive nanoparticles into porous ceramics, and studies the optimal size of conductive inclusions in a simplified 2D filter structure.

Each part of the results is written as a stand-alone chapter and has its own materials and methods section, results, and short summary. Joint conclusions and outlook, along with suggestions for further development of the field, are provided in **chapter 8.**

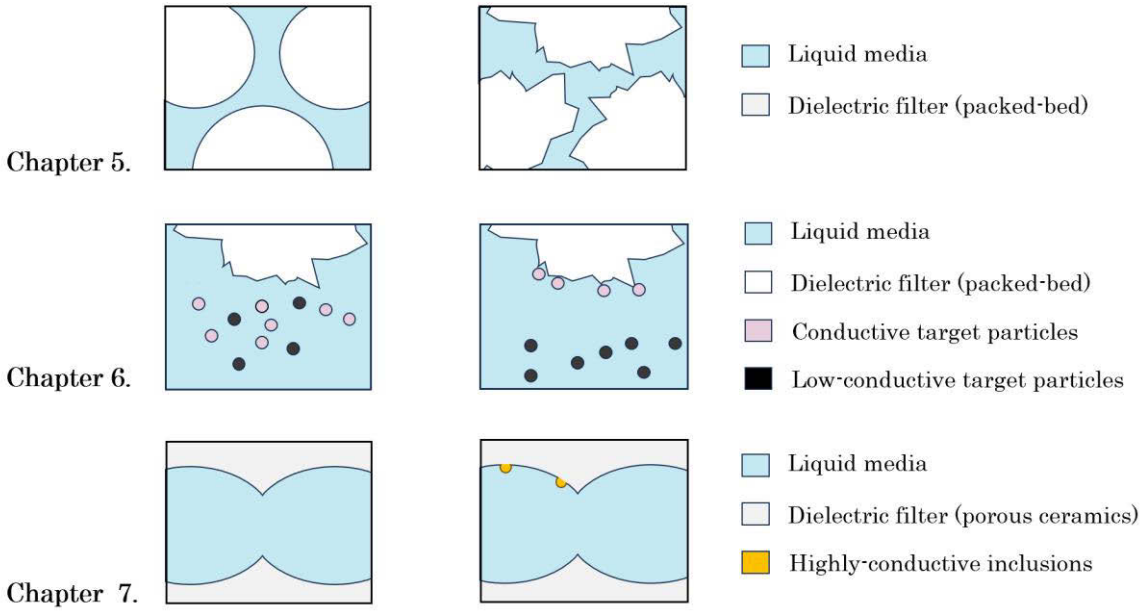

FIGURE 4.1 Thesis results chapters visualized

Chapter 5: Topological considerations: macro filter geometry changes

In this chapter, the main question concentrates on the geometrical aspect of the macro filter for DEP. A study is conducted using packed bed filters, the geometry of which is straightforwardly adjustable with the usage of a certain grain type. The content of this part is a modified copy of the text and images from the author's publication from 2023 with adapted colors and writing to match the style of the thesis (CC BY 4.0), apart from the investigation on recovery rates and angularity analysis, which were not a part of this paper [1].

A selection of the grains was done in a way that introduces angular and spherical grains as a packed bed filter material. Two types of angular grains were under consideration: sand and crushed glass, representing the edges on their surface; glass beads were taken for the non-angular (spherical) grains. The crushed glass sample was taken for the tests because it allowed for a proper shape comparison between grains with the same material configuration (as both glass beads and crushed glass are soda-lime glass). In total, three fractions of each grain type were tested out in this research, with modal grain diameters ranging from 200 µm to 500 µm: in a fraction of 150-250, 250-355, and a fraction of 355-500 µm.

I Materials and methods

This section summarizes all the methods and materials required for the macro filter geometry investigations. First, the section describes the target particles used for the filtration tasks in the DEP setup. Then, it provides an overview of the DEP filter setup with various (filter) grains packed inside for their experimental validation of the separation efficiency. Afterward, these grains are characterized via several methods, such as particle size distribution (PSD), micro-computed X-ray tomography (µCT), and image analysis.

I.1 Particle suspension

To map the filter performance, it is beneficial to use the target particles of known geometry and material, which are straightforward to capture. The DEP separation performance of all packed bed filters was measured with fluorescently labeled

carboxylated polystyrene particles (PS), purchased as Polysciences Fluoresbrite Yellow-Green Carboxylate Microspheres at Polysciences Europe GmbH from Germany. In terms of their size, these particles have a diameter of 0.5 µm and a coefficient of variation of 3 % (as reported by the manufacturer). The suspension, in which particles were injected, was prepared in-house. The procedure involved mixing PS particles with ultrapure water (Omniatap 6 UV/UF, stakpure GmbH, Germany) to a concentration of 2.2×10^6 particles per ml. To lower the unspecific adsorption of particles to the filter in use, a tiny amount of Tween 20 (Sigma–Aldrich, Germany) was injected to the suspension (with a final concentration of 0.002 vol %). A monitoring of the temperature and conductivity was arranged during the experiment, with mean values of 1 ± 0.1 µS/cm and 22 ± 1.3 °C (with respective standard deviations).

I.2 Setup details

The filter setup matches that in former studies of the group where the author of the thesis was working [21,44]. The DEP experimental setup, initially created by Malte Lorenz, included a suspension beaker, a peristaltic pump (REGLO Analog, Ismatec, Switzerland), a filter cell that had a DEP manipulation region featuring two stainless steel electrodes, all assembled in-house, and a fluorescence spectrometer (FluoroMax 4, Horiba, Japan) (schematically shown in Figure 5.1) [21]. The suspension beaker has a connection to the pump. The pump had two connections in Teflon tubes: one joining the pump to the filter cell and another joining the pump directly to the spectrometer (bypass). Changing between the tubes was feasible using a three-way valve. This was done to allow for mechanical trapping measurement.

The DEP manipulation region inside the filter possesses dimensions of 8 x 29 x 18 mm, with tapered inlet and outlet sections, and is constructed from polytetrafluoroethylene. It contains two large plates of stainless steel that serve as electrodes, located 8 mm from each other. In the space between the electrodes, the grained filter was installed in the configuration of a packed bed that matched the dimensions of the filter cell. The details of the installation and its reproducibility are shown in Appendix 2. Each fraction of the grains was positioned within the filter cell as follows: 13 grams of grains were measured out, added to the filter cell, and secured using a polyamide mesh which had a regular pore size of approximately 110 µm, which closed the 8 x 18 mm gap for the cross-section of the flow. After carefully

closing the cell, the assembly was rotated 90° and flushed with ethanol and pure deionized water through the inlet of the experiment.

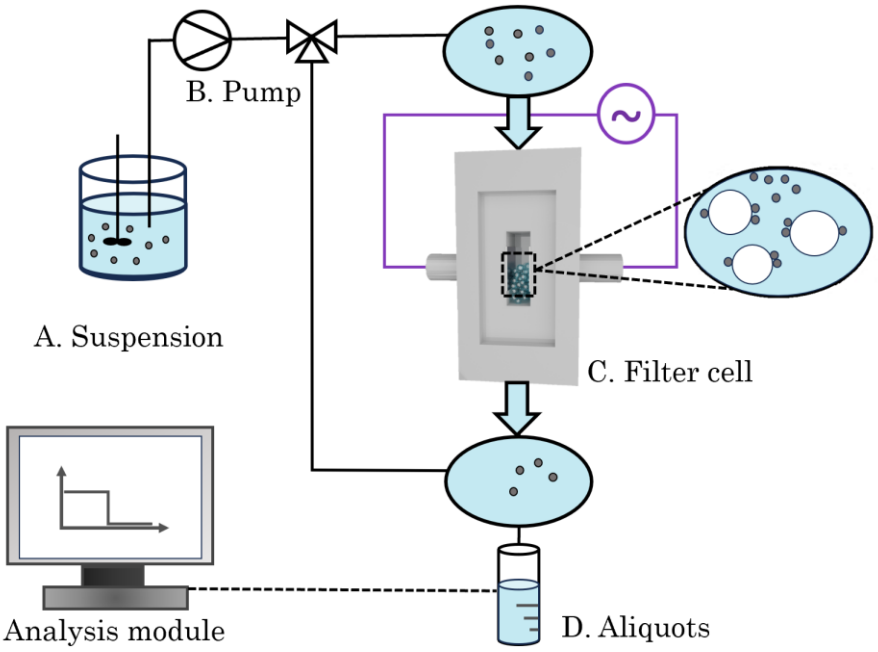

FIGURE 5.1 A schematic representation of DEP experimental setup. In the filter cell are loaded the packed bed filters of various forms (such as glass beads, milled glass and sand). The image is redrawn from the components of the setup images from the authors papers [1,24], CC BY 4.0.

The generation of an electric field was achieved by using a sinusoidal voltage (up to 450 Vrms at 1 kHz) across the electrode gap with a voltage amplifier (PZD700A, TREK Inc., USA) and a function generator (HM8131, Hameg Instruments GmbH, Germany). During all conducted experiments, the current was monitored by a power analyzer (LMG 670, ZES ZIMMER Electronic Systems GmbH, Germany).

The concentration of the target particles traveling through the filter cell was also checked online with a fluorescence spectrometer, which features a quartz flow-through cuvette (176.762-QS, Hellma). According to the manufacturer, the PS particles had a particular excitation/emission wavelength of 441 nm and 486 nm. In the online measurement, the concentration of the PS particles is linearly related to the intensity signal (measured in counts per second, cps) [44]. For the statistics, each experiment was repeated at least three times before calculating the final separation efficiency. As preparation for each of these experiments, the pure water at a flow rate of 11 mL/min was pumped through the filter cell to ensure that the grains were wet before introducing particle suspension to the system.

I.3 Trapping efficiency of the filters

Before each DEP efficiency recording, the background intensity signal from flushing pure water through the filter cell was registered with the spectrometer. Subsequently, the suspension was initially directed to the bypass (where it flowed directly to the spectrometer without going through the filter cell). This procedure allowed the particle concentration to be recorded without mechanical trapping. The details are shown in Appendix 3.

To calculate separation efficiency, Equation (2.49) was used. The flow was directed to the filter cell, set to a constant 11 mL/min flow rate, and set the initial particle concentration inside the filter, denoted as c_0 ("load" phase, Figure 5.2). When the concentration of particles stabilized, an electric field was applied across the porous filter. To calculate the recovery rates, the suspension was flushed through the filter cell without any pH modifications or flow rate changes after the electric field was off and the Equation (2.50) was used for a calculation in a similar manner ("recovery", Figure 5.2).

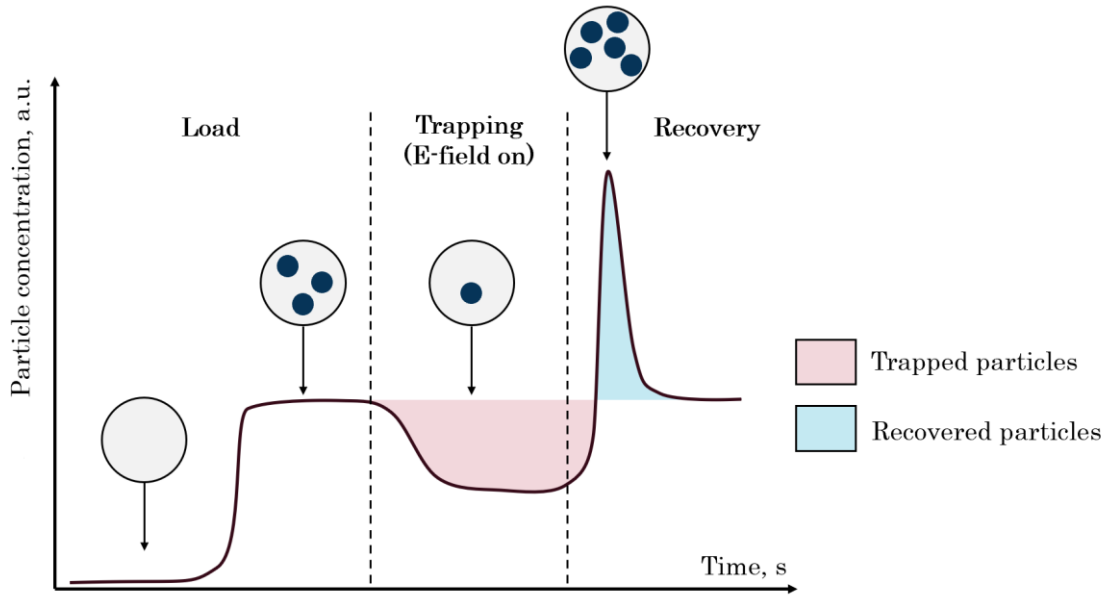

FIGURE 5.2 A visualization of the recovery process in DEP filtration.

I.4 Packed beds grain size analysis

The filter grain size was analyzed using laser diffraction (LD, Mastersizer 2000, Malvern Panalytical GmbH, United Kingdom). The analyzer featured stirring and dispersion units set to operate at 2500 rpm. The analysis began when the grains, dispersed in water, reached an obscuration level in the range of 3 % to 15 %. The

analyzer was cleaned and refreshed with pure water between each fraction measurement. To maintain consistency, each fraction was stirred in the storage reservoir for 10 seconds before sampling and only then extracted for testing. For the statistics, this measurement process was repeated three times for each fraction and each grain type.

I.5 Sieving

The grains were divided into three fractions using a Retsch Vibrotronic Type VE 1 sieving device (Retsch GmbH, Germany). As was already mentioned, this study presents three types of grains: glass beads, sand, and crushed glass. Each type of grain was individually sieved in the device mentioned above via a standardized set of sieves. Each grain type was divided into three size fractions, with each fraction separated using two sieves: 150 and 250 µm, 250 and 355 µm, and 355 and 500 µm. The grains retained on the smaller sieve (i.e., 150 µm, 250 µm, or 355 µm) were taken for further DEP experiments and labeled accordingly as mesh 150, 250, or 355.

I.6 Micro-CT (µCT) analysis of the packed beds

Micro-CT analysis was performed to get the structural parameters of each packed bed. Here, the pore sizes, porosity, tortuosity, and other quantities mentioned in theory section about filter characterization are considered structural parameters. To reduce the number of scans and corresponding measurement costs, it was decided to perform only the scans of the sand and the glass beads in two size fractions: mesh 355 and 250. The grains of each type were packed in the same quantities used in DEP experiments into 3D-printed plastic containers with dimensions of 8.3 x 20 x 30 mm^3 and a container wall thickness of 0.5 mm. The equipment allowed the scans with a 7.85 µm/voxel resolution, conducted using an Xradia 520 Versa X-ray microscope (ZEISS, Oberkochen, Germany). The images were produced by the attenuation of X-rays as they passed through the packed bed configuration. Subsequently, a reconstruction technique provided a 3D spatial representation of the sample based on the helical path traversed by the objective. Each voxel in the reconstructed image had its 16-bit grayscale value and represented an X-ray attenuation coefficient correlated to the sample density. Scans were carried out at MAPEX-CF facilities with 1600 projections per rotation, featuring a 4x objective length. The resulting 16-bit computer tomography (CT) image was processed by

Nurul Karim to segment these packed bed structures, as a part of a collaboration arranged by the author of this thesis.

II Results and discussion

II.1 Grain's particle size distributions

The particle size distribution (PSD) was analyzed for the three size fractions of each grain type. These size fractions are labeled as 150, 250, and 355 mesh, based on the smallest mesh size (in μm) from which they were taken after sieving. A full parameter set for the characterization of each sample is provided in Appendix 4. It is important to note that the mesh size does not relate to the median particle diameter; for example, the d_{50} of the sand-type fraction is 365.2 μm, while the corresponding sieving mesh size of this fraction is 250 μm. The mesh size label represents the sample's smallest sieve's grain diameter. Additionally, d_{50} represents the diameter at which 50 % of the total amount of grains are smaller than this particular number (in μm), d_{90} means 90 % are smaller, and d_{10} indicates 10 % are smaller.

According to a volume-based analysis, all three packed bed samples exhibit polydispersity and have a monomodal distribution (Figure 5.3). It can be concluded that the particle size distributions of the samples are similar, with the d_{50} values of the sand and glass beads being comparable, particularly for the smaller grain sizes (with a variation of 1.8% for the sample size of mesh 150). In contrast, particularly at the larger grain sizes, the d_{50} of the crushed glass is notably larger. For example, when comparing the crushed glass sample to the glass beads, the d_{50} is 21 % larger at mesh 250 and 16 % larger at mesh 355. This difference is attributed to a slightly wider Gaussian distribution for the sample size of mesh 355 in crushed glass and is further influenced by the chosen manufacturing method (the material labeled as crushed glass was not commercially available. Therefore, milling was arranged in-house, and sieving of such material is further demanding due to the non-spherical shape of the grains going through the set of sieves).

The coefficient of variation (COV) for the most important parameters of each fraction was additionally examined. For the grain types such as glass beads and sand, the COV showed a strong correlation with variations below 3 % for d_{50} and below 5 % for d_{10} and d_{90}. The crushed glass also met the same correlations for d_{50} and d_{10} in the mesh 250 and 355. However, the COV falls outside the specified limits for the

smallest fraction of the crushed glass (mesh 150), which has a wider dispersion. This deviation may be due to the agglomeration of particles within the storage reservoir, which is especially the case for the smaller sizes of these particles. This could potentially be resolved by employing another method of sampling.

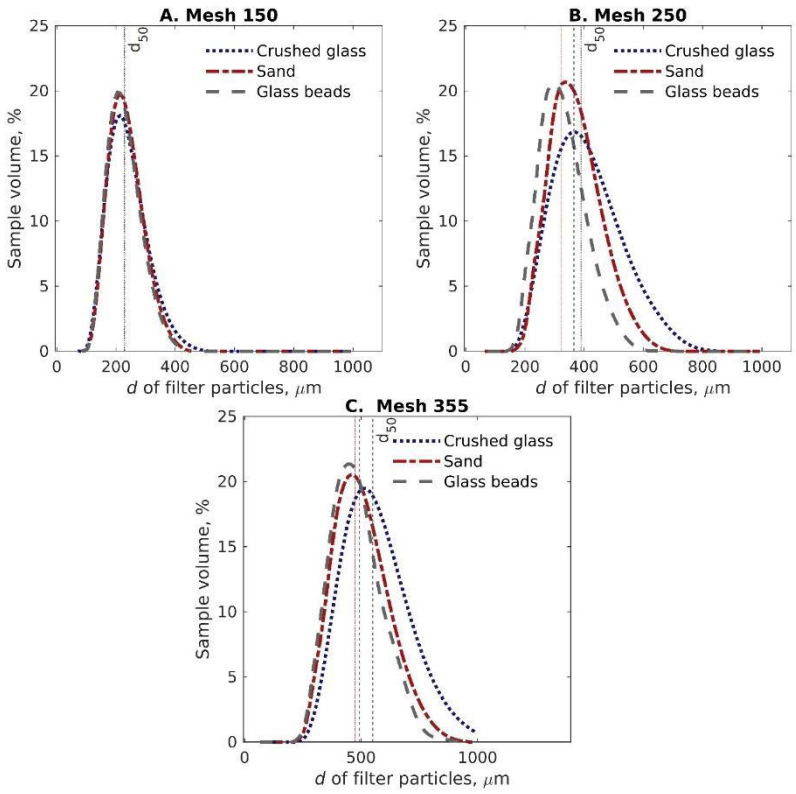

FIGURE 5.3 Results from the particle size distribution of the three different grain types in three different sizes: A. mesh 150, B. mesh 250, C. mesh 355. Image and caption, adapted from the author's paper [1], CC BY 4.0.

II.2 Micro-CT analysis of the packed bed samples

The filter matrix structure was morphologically characterized using micro-computed X-ray tomography. Packing was uniformly managed for all samples during tests. The investigation included glass beads and sand samples (mesh size 250) and two sand samples with mesh sizes 250 and 355. Figure 5.4 illustrates the 3D μCT images of all the samples (glass beads mesh 250, sand mesh 250, and sand mesh 355) along with their pores. Details regarding segmentation and analysis are mentioned in the author's paper from 2023. They are not a subject of this thesis due to the fact that they were established and described by Nurul Karim. The complete table with details of these results is located in Appendix 5.

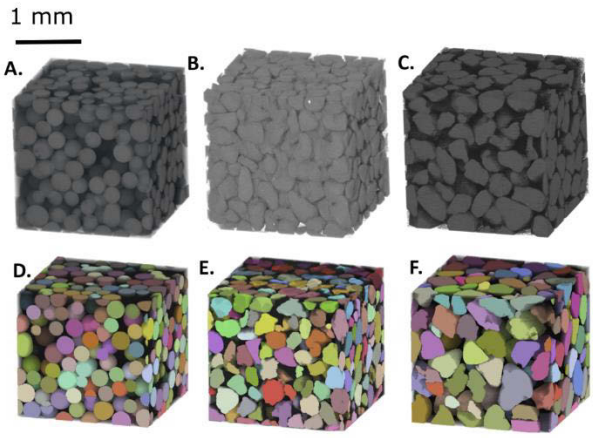

FIGURE 5.4 A visualization of the grain segmentation process, demonstrated on glass beads and sand samples: grayscale-based models of three different filter structures (A: glass beads mesh 250, B: sand mesh 250, and C: sand mesh 355) and after-processing segmented grains of these samples (D–F, respectively). Image and caption , reprinted from the author's paper [1], CC BY 4.0.

In general, the sand fractions possess comparable porosities, with 35 % for mesh 250 and 38 % for mesh 355. The comparable sand sample in mesh 250 of the glass beads shows a porosity of 43 %, which is approximately 8 percentage points higher — the sand sample with mesh 250 exhibits the smallest hydraulic pore diameter. The hydraulic pore diameter for the mesh 250 glass beads sample is notably 157 µm, similar to the 151 µm observed in the mesh 355 sand sample. The hydraulic pore diameter in the mesh 250 sand sample is 132 µm, roughly 20 µm smaller than the above values.

The sand mesh 250 sample exhibits the highest surface area related to its smallest grain size and pore diameter. The sphericity of the pores for both sand samples is three orders of magnitude lower than that of the pores formed by the glass bead sample. This is attributed to the higher angularity of sand in contrast to the spherical glass beads.

Previous studies on DEP filtration have consistently shown that DEP trapping efficiency increases as pore size decreases. Therefore, it is highly likely that the smallest sand fractions, with their smaller average pore diameter compared to the mesh 355 glass beads, will exhibit the highest DEP efficiency among these three samples. This potential is further supported by the likelihood of similar DEP trapping efficiencies between the mesh 355 sand sample and the mesh 250 glass

bead sample. This assumption is based on comparing the pore diameters formed by the structure (Appendix 5). It would likely remain valid unless the morphological structure of the grains (or the grain type in use) notably influences the trapping (i.e., the greater number of edges on the grain, which could improve the DEP effect).

II.3 Comparison of the filter efficiencies of the different filter matrixes

pDEP is exhibited by polystyrene particles at the utilized frequency of 1 kHz. The trapping of these particles in the absence of an electric field in the given packed beds is low, as was expected since these particles are three orders of magnitude smaller than the filter's pore sizes. The DEP experiments conducted are shown in Figure 5.5.

As grain size decreases and pore size decreases, DEP separation efficiency rises for all materials (Fig. 5.5 A-C). Additionally, separation efficiency improves with higher voltage, and this trend is valid for all grain types and sizes. Previous findings agree with this observation: separation efficiency increases as pore size decreases. This occurs because the electric field gradient is larger at smaller pore sizes, and particles go through the filter at shorter distances to get captured [21]. The separation efficiency for various size fractions of each material is nearly identical and always below 50 % at the lowest voltages in use (300 V_{rms}).

While inspecting angular grains (sand and crushed glass) and spherical grains (glass beads), it can be observed that the separation efficiency increases with the angularity of the filter grain (Fig. 5.5 D). Interestingly, the efficiency is more pronounced for crushed glass mesh 150 than in other samples. This can be attributed to a wider sample distribution, resulting in slightly different grain sizes than sand and glass beads of the identical mesh. Another trend is seen at the highest voltage. It can be observed that glass beads (represented by the dark grey line in Fig. 5.5 D) exhibit the lowest DEP trapping efficiency among all samples, followed by sand (shown by the red line). The highest trapping efficiency is demonstrated by the crushed glass. Overall, distinctions between the types of grains are more substantial than variations in pore sizes within a single type of grain (Fig. 5.5 D, the lines display notable differences between each other compared to the endpoints of each line). Remarkably, the hydraulic pore diameter of the mesh 350 filter (sand sample) is similar to that of the mesh 250 filter (in the case of glass beads), measuring 151 µm and 157 µm. Nevertheless, the DEP efficiency of the glass bead sample is significantly inferior to that of the sand. This suggests that the shape of the grain

and its surface characteristics significantly affect DEP efficiency, as the intensity of the field gradient directly relates to grain morphology. Certain aspects of one study by Claire Crowther and Mark Hayes (2017) correlate well with this hypothesis [118]. In their investigation, an elliptical insulator with additional smaller insulators distributed across was the most effective insulator design for DEP [118].

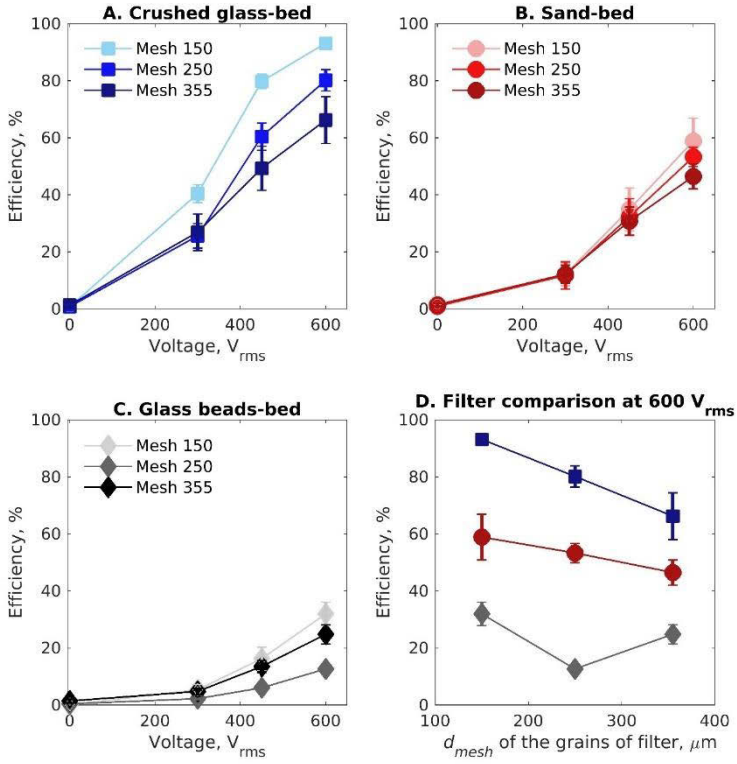

FIGURE 5.5 A trapping efficiency of different packed bed filters at 11 mL/min flow rate and frequency of 1 kHz. (A-C) Separation efficiency as a function of voltage and grain size for A. crushed glass beads, B. sand particles, and C. glass beads. (D) Separation efficiency as a function of grain size and grain shape at 600 V_{rms} for three different filter materials (dark blue – crushed glass, red – sand, dark grey – glass beads). The error bars represent the standard deviation in all the cases. Image and caption, recolored from the author's paper [1], CC BY 4.0.

Also notable that at the high applied voltages (particularly at 600 V_{rms} and higher), an induced-charge electroosmotic flow (ICEO) can further influence the trapping of the target particles [44]. Because the experiment conditions included sealing the filter cell on top, no vortices were noticed during the particle trapping process. Yet, for a comprehensive characterization, it is recommended that the setup design be

modified to completely visualize the potential complexities of ICEO. Another electrokinetic flow (electrothermal motion) can also be indicated at high voltages (600 V_{rms}). Still, it is typically not anticipated to impact DEP trapping at low fluid conductivities in use here (≤ 2 μS/cm) [49].

II.4 Comparison of recovery rates

To calculate the recovery rates of PS, utilization of the formula from the theory Equation (2.50) can be done with an addition that the areas under the intensity signal of PS can be calculated numerically and used for concentration estimation in the following way: $c_r = S_{released} - S_{normal}$, where S_{normal} is the area under the curve when no electric field is present in the system, and $S_{released}$ is the area under the signal of released particles[119]. For the filter with the glass bead fractions, the recovery of 500 nm PS particles was around 90 %; for the sand, it was around 73 % and for the crushed glass, it was around 95 %. It should be noted that in these tests, the electric field was applied for about 5 minutes. From some old patents, for instance, from the one from Gulf R&D company by G. Ray Fritsche and Leonard Haniak from 1975, where they also discussed the measurements with irregular grains, can be seen that the irregular surfaces in the grains did not perform well, supposedly because of the filter clogging issues [96]. While that would highly depend on the target particles' type, size, and concentration, recovery of most of the target particles in the current experimental setting was possible. The sand, demonstrating lower recovery, also showed higher mechanical trapping (Appendix 3) in the absence of the electric field [1], which might be associated with zeta potential differences between PS and sand surface. The second interesting test was a check of the recovery rate of the PS particles on the longer test. In this case, the electric field has to be turned on for almost an hour and the trapping efficiency has to be extracted in a similar manner from the recorded PS signal. In this long-term testing, the sample of crushed glass demonstrated an 80 % recovery rate, with an electric field being applied for ≈50 minutes at an 11 mL/min flow rate. To put these numbers into the context of a bigger picture, Malte Lorenz et al. in 2020 showed the recovery of the same PS particles in the long-term experiments in ceramic sponges with a recovery rate of about 65-75 % and later on showed that with pH adjustments, that number can be higher than that [21]. To benefit from this finding, a similar strategy can be used with the current samples of this study (was not pursued further in the context of the current work).

II.5 Scanning electron microscopy

Scanning electron microscope (SEM) images of individual grains were captured in the mesh 150 size fraction (Figure 5.6). The nearly perfect spherical shapes are present for the glass beads (Figure 5.6 A). This is opposed to both sand and crushed glass (Figure 5.6 B and 5.6 C), which display more small steps and kinks on their surfaces, indicating higher amount of edges.

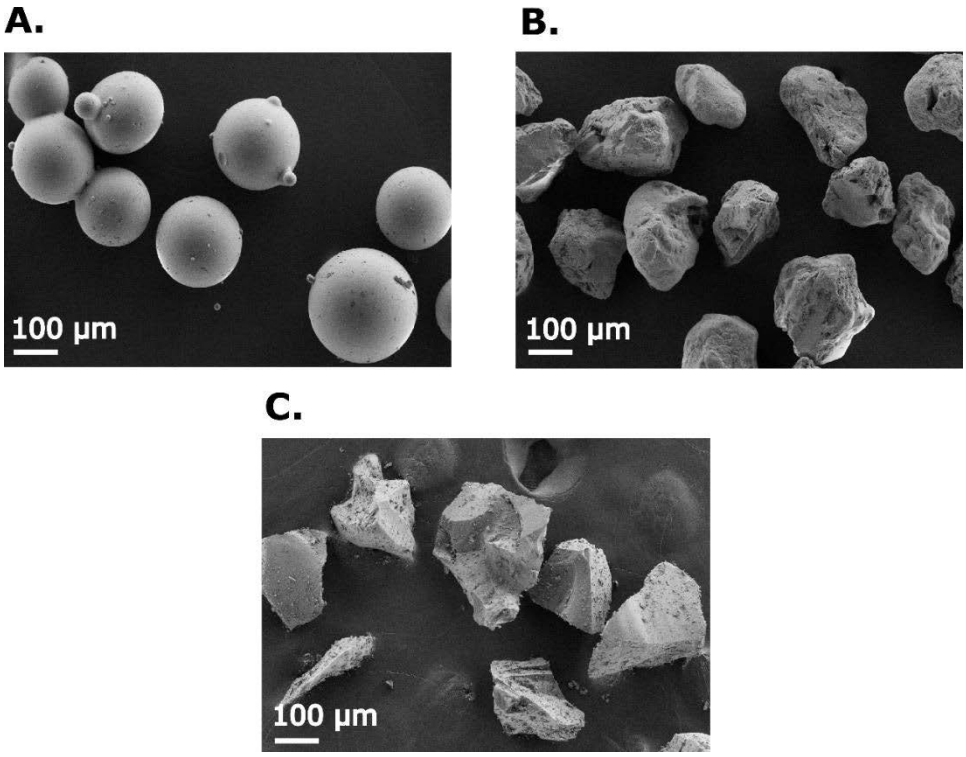

FIGURE 5.6 SEM images of the three grains investigated in this study, A. glass beads. B. sand, C. crushed (milled) glass. Image and caption, reprinted from the author's paper [1], CC BY 4.0.

By comparing the DEP results with SEM pictures, the hypothesis that specific grain morphology enhances trapping efficiency is verified. Notably, this trapping efficiency improvement is independent of pore size. One previous publication noted that sharp edges of insulating posts in iDEP offer benefits only when the distance between the posts is minimized [116]. Across the three pore sizes studied in this research, no evidence of this behavior is detected in macro-scale filters. In contrast, it is observed that DEP trapping efficiency rises with grain angularity or morphology change across all three-grain size categories (susceptible to future comprehensive examination focused on measuring the angularity and morphological characteristics of these grains).

II.6 Grain morphology: angularity

To further discuss the geometrical aspects of the filter grains, was conducted an additional μCT scan performed at Technical University (TU) Bergakademie Freiberg, Institute of Mechanical Process Engineering and Mineral Processing (Figure 5.7) [120]. This part of the investigation was done to present a feasible characterization parameter for the "angularity" of the grains. The samples of three materials (sand, glass beads, and crushed glass) in the fraction of the mesh 150 were sent for the test (with a resolution of ≈1 μm). TU Freiberg performed the shape analysis in collaboration with the author of this thesis. The center of gravity was determined for each particle (Figure 5.7 D). Then, the distance from each surface pixel to the particle's center of gravity was measured, and an average of all the distances for each particle was calculated. Then, the procedure was repeated for all the particles, and around 900 values were obtained for each particle system. The details of these parameter extractions are not a subject of this thesis because colleagues from TU Freiberg established them and thus are not a part of the own work of the author (the raw data for these graphs is stored by Alica Rother, according to the transfer protocol).

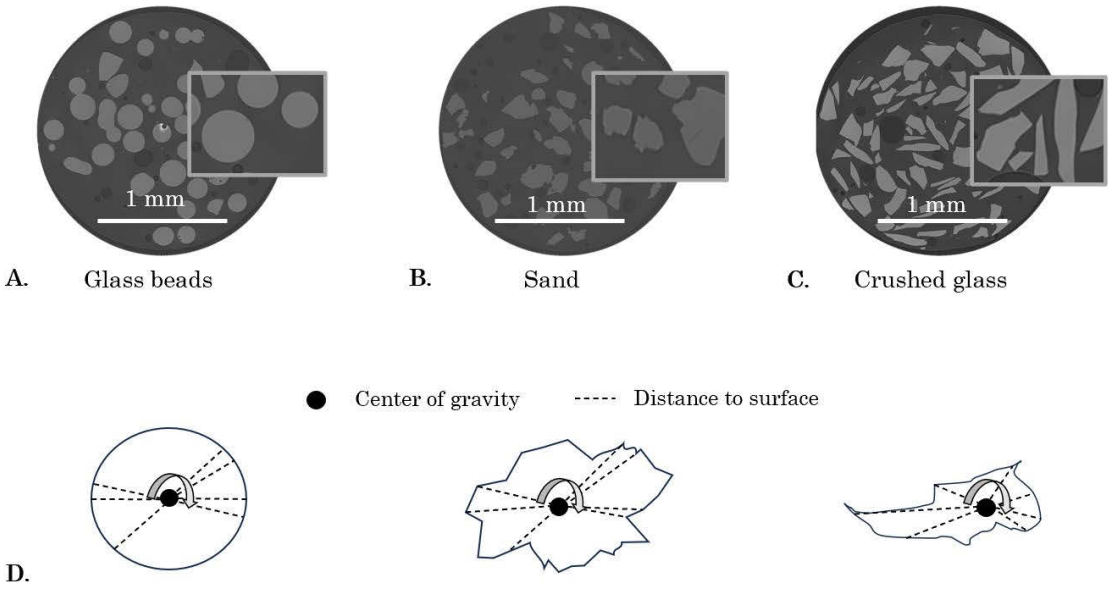

FIGURE 5.7 **μCT** scans of the grains for their surface characterization (A-C) and schematics of the center of gravity for each type of the grain (D).

When there are many edges on the surface of the particle, the distances from the surface to the center of the gravity of the particle would always change. To estimate

a shape of each particle and distinguish the angularity of materials between them, one can use the standard deviation (STD) of these distances. If one plots this parameter for three materials (Figure 5.8). STD is more or less symmetrically distributed for each of the grain systems. A high STD means a high deviation of the distance to the surface, which might indicate edginess/angularity. A broad distribution of STD means that particles in the sample are all different; some are more rapidly changing, and some are not (such as glass). In the case of the sand, the median is low, which means that sand particles are relatively compact. When one looks at the distribution for the glass beads (Figure 5.8, panel A), a low standard deviation of these distances is present and quite typical for the spheres (without kinks on the surface, the distance from the center of gravity to the surface would not change much). However, there are broader distributions of sand and crushed glass. That indicated that the surface of these materials' grains changes a lot and, therefore, is more irregular.

To better identify the relationships between the parameters of each particle, it is advisable to plot the standard deviation of the distances over the radius distributions of the particles (Figure 5.8, panel B), with a goal to identify if there are any changes in the number of edges when looking at the sizes of the particles. Looking at the box plot for glass beads, it becomes evident that the STD values show minimal variation, with some outliers. The length of the box indicates data dispersion, and in the case of sand, the distribution appears asymmetrical. Figure 5.8, panel B shows the grain "size" dependency of STD. If one zooms in on the data, one can see that there are two centers because points around the small sizes of the particles overlap with each other very much. It means sand particles would have different "edginess" depending on size. For smaller sand particles, the distance to the surface would change less than in the case of the bigger sand particles. Interestingly, the analysis showed no relation for glass beads: there is no change (no size effect) on the edges of this material (as was to be expected, assuming glass beads as a perfect sphere). An increased standard deviation with an increased radius of the particles was observed for the other materials. For both sand and crushed glass (especially for the crushed glass), bigger particles have more edges than the smaller ones. That means that the materials of the sand and the crushed glass do possess differences in their shape factors, and, while comparing these fractions in of each other, crushed glass would be a more edgy one. It is interesting to note that the STD, on average, is very high. For the crushed

glass, the highest STD is 400 µm with a less than 50 µm radius. That would mean some very thin particles in the sample, which are very long in one direction.

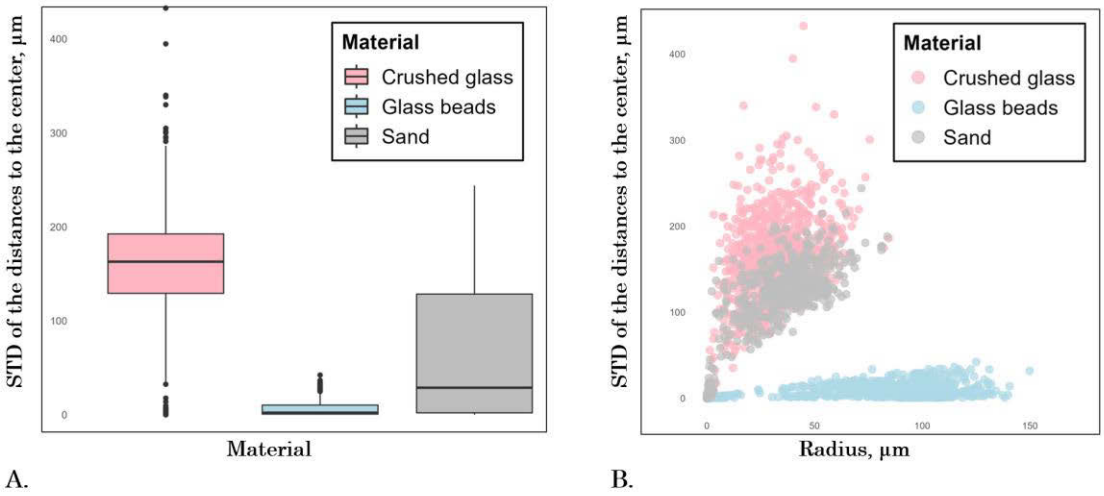

FIGURE 5.8 Analysis of the grain angularity. A: Standard deviation of the distances measured from each particle's center of gravity. B: Focusing on the size dependency, the standard deviation of the distance over the radius of the particles. The STD is not increasing for the glass beads but drastically for the crushed glass and the sand. Note: the average distance to the center (radius) can also not be half of the particle size (depending on whether the center of gravity is shifted or not); therefore, when it comes to the size analysis of the fractions, laser diffraction is a better and more suited method for that.

III Summary of the results of this part

In this chapter, an influence of grain filter shape factors, including surface morphology, on DEP trapping efficiency was researched experimentally with PS particles. The main findings from this chapter of the thesis enhanced the general understanding of the design of macro-scale dielectrophoretic filters.

Tests in the packed bed filters show that grain angularity confirms benefits irrespective of the dimensions of the grain (within the investigated sizes) for PS particles in use. It is an observation opposing a prior study on the design of insulating posts for iDEP pDEP, which explicitly hinted at the advantages of the sharp edges of post surfaces when post-to-post spacing is small. This underscores a need for further research to create a link between grain shape and pore size for a thorough recognition of these mechanisms. Additionally, the author also

recommends considering other grain size characterization devices for a more precise control of sieving the materials into different fractions. For instance, those that can measure the PSD of grains while considering particle shapes.

A shape-related characterization of the grains was made according to the deviations from the center of their gravity. That allowed to show the differences in the particle systems better than the visual investigation by SEM. It shall be emphasized again that a single parameter that allows for defining a particle geometry does not exist: one must see the overall data (for example, the box plots from Figure 5.8) to identify the material. The author believes more studies are needed to classify the 3D grains in terms of their surface properties and to develop such a characteristic. Additionally, with crushed/milled glass filters, it would be very beneficial to have precise control of the grain surface changes before and after cleaning the filter because fine powders, present there straight after milling, could also enhance the DEP.

Chapter 6: Selective Separation: lithium-ion batteries

The application-related part of the thesis underscores a promise of dielectrophoretic filtration as an auxiliary purification step in the recycling of battery components and thus obtain a material-selective separation. Here, the separation task of two different materials, accomplished by dielectrophoresis, is discussed in more detail with a mixture example. The mixture undergoing the separation in this part of the thesis contained uncoated lithium iron phosphate (LFP) and graphite particles, which, along with some modifications and other impurities, are a part of lithium-ion batteries. The content of this part is a modified copy of the text and images from the author's publication from 2024 with adapted colors and writing to match the style of the thesis [24] (CC BY 4.0).

I Materials and Methods

This section summarizes all the methods and materials required for the material-selective separation to take place. First, the target particles used for this task and the suspension preparation method are discussed. Then, the DEP setup used for separation is mentioned again, with the emphasis of the change on the particle detection methods.

I.1 Particle suspensions and the setup

The target particles were virgin materials acquired as fine powders with particle sizes below 5 µm from Sigma-Aldrich. Uncoated lithium iron phosphate and graphite particles constituted the particle suspensions in use. MSE Supplies sourced the graphite (TIMCAL KS-6) as a powder with an average particle size ≤3.4 µm. The particle size distributions were determined using laser diffraction (LD, Mastersizer 2000, Malvern Panalytical GmbH, United Kingdom) before the DEP experiments, and the results are illustrated in Appendix 7. The results closely matched the size ranges provided by the suppliers.

Deionized water (Omniatap 6 UV/UF, Starkpure GmbH, Germany) was used to suspend the particles at concentrations of 4 mg/L for graphite and 8 mg/L for LFP to arrange pure particle suspensions. Tween 20 solution (Sigma-Aldrich, Germany)

was used to achieve a final concentration of 0.004% vol. The final suspension undergoes the conductivity adjustment by adding 0.1 M KCl, reaching a final value of 1–15 μS/cm. A stirring magnet continuously disturbed the suspension during the measurements. For the mixed suspension, graphite and LFP were combined at the same concentrations as in their separate suspensions.

The DEP filter matches the one detailed in Results Chapter 5. Therefore, in this chapter, only schematic of it is shown (Figure 6.1). A packed bed of grained silica material (sand mesh 350) was installed as a filter. The diameter of the target particles is at least 20 times smaller than the pores in the packed bed. In all the experiments, a peristaltic pump (REGLO Analog, Ismatec, Switzerland) was set at a constant flow rate of 360 mL/h.

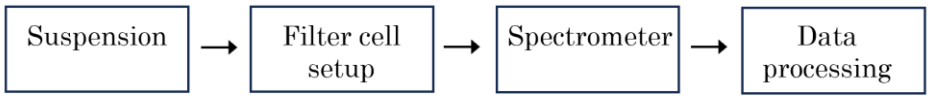

FIGURE 6.1 A simplified setup schematics for DEP experiment.

I.2 Particle detection methods

A spectrometer (HORIBA, FluorMAX-4) combined with MATLAB processing was utilized to qualitatively identify the trapping efficiency of the prepared suspensions, following the method described in the previous results part, with a difference that, in this case, particles are not fluorescent ladled and thus can only be detected via their reflection. This reflection of the particles at the outlet of the filter was detected online to provide a qualitative evaluation of DEP separation efficiency in the case of separate suspensions. Since the supplier informed that the particles are not perfect spheres, their concentration can only be measured qualitatively in this manner.

Atomic absorption spectroscopy (AAS) was utilized to quantitatively assess the separation efficiency of LFP in a mixture with graphite. A set volume of around 20 mL of the particle suspension was secured into 50 mL volumetric flasks during the various phases of the experiment for AAS analysis. 3 mL 65% nitric acid (VWR International, Belgium) and 3 mL 30% hydrogen peroxide (Sigma-Aldrich, Germany) dissolved the LFP. The next step was adding to the volumetric flasks pure deionized water, after which the lithium content within the mixture was detected with AAS using a Solaar 989 QZ AA Spectrometer (Unicam, England) equipped with a GF90+

furnace and an FS90+ autosampler. This measurement was planned and analyzed in the context of DEP by the author of this thesis, but arranged and conducted by Alica Rother.

It shall be noted that in the current state of the research, a lower solid-to-liquid ratio of the particles was prioritized as in this case they are more dispersed. Their interactions with the electric field can be more individually controlled and it overall simplifies the procedure for analysis with the AAS device (as it requires a dilution of the sample to a certain sensitivity value, and a significant increase of the concentration would also significantly add the dilution steps for the analysis).

II Results and discussion

Due to bulk conductivity of graphite particles being much higher than that of the aqueous suspension, pDEP behavior was predicted. Conversely, particles with a low conductivity value of 10^{-7}–10^{-8} S/cm, such as uncoated LFP, are expected to exhibit nDEP behavior since their conductivity is lower than that of the surrounding medium [121,122].

The test exploits the material selectivity using DEP when the conductivity of the medium surpasses that of the target particles significantly; the particles are moving away from the electric field maxima, demonstrating negative dielectrophoresis (nDEP). Conversely, when the particle conductivity exceeds that of the medium, the particles are drawn toward the local field maxima affiliated with positive dielectrophoresis (pDEP).

Therefore, initially, the analysis focused on determining if LFP exhibited negative DEP in a basic setup. Due to the need to show the nDEP (which explains the absence of trapping at higher conductivities for the LFP), the experiment was performed with LFP only (as graphite would exhibit pDEP behavior at these conductivities). The interdigitated electrode array had a 50 µL drop of the LFP suspension, which had a conductivity of 30 µS/cm, positioned on top of it. Particle movement was monitored using a microscope while using a voltage of 20 V_{rms} at 15 kHz with a signal generator (Rigol DG4062, Rigol Technologies EU GmbH, Puchheim, Germany). Utilizing an inverted microscope (ECLIPSE Ts2R-FL, Nikon Instruments Europe BV, Amsterdam, Netherlands) and a CMOS camera (Grasshopper GS3-U3-51S5C-C, FLIR Systems Inc., Wilsonville, OR, USA), the particle movement was detected. The interdigitated electrodes, featuring arms and gaps measuring 100 µm, were

manufactured using conventional cleanroom methods: this setup was borrowed from Laura Weirauch by the author of the thesis. Shall be noted that this configuration channel had no stirring device.

After turning on the voltage, LFP particles concentrated in the region between the electrodes, a characteristic nDEP behavior [24]. It should be emphasized that not all particles were transported there. Some particles were agglomerating, becoming too heavy and sedimenting in the channel (Figure 6.2)

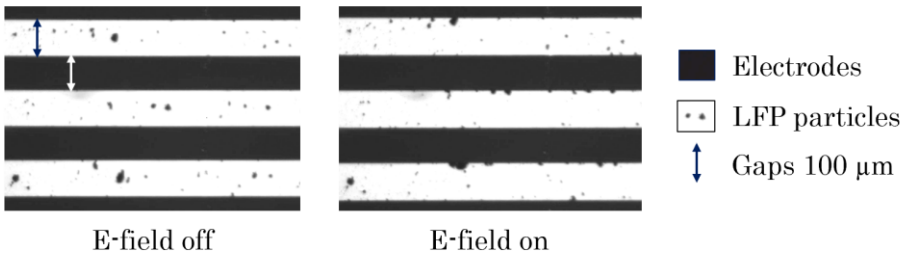

FIGURE 6.2 The behavior of LFP (marked in black) in an array of interdigitated electrodes at 20 V and 15 kHz and at 30 µS/cm conductivity. Upon application of an electric field, the randomly distributed LFP particles (left) are predominantly repelled to the space between the electrodes (right). This is typical behavior for the target particles that experience nDEP. The electrode distance is 100 µm. Image and caption, adapted from the author's paper [24], CC BY 4.0.

As a next step, an investigation was conducted to separate LFP and graphite in the DEP setup mentioned in the method section. Results showed that in non-selective suspensions, at 5 µS/cm, the capture of graphite particles enhanced with higher voltage, as predicted for pDEP particles (Figure 6.3, panel A). Similar behavior is demonstrated by LFP, potentially attributable to nDEP effects, as was already noted [21].

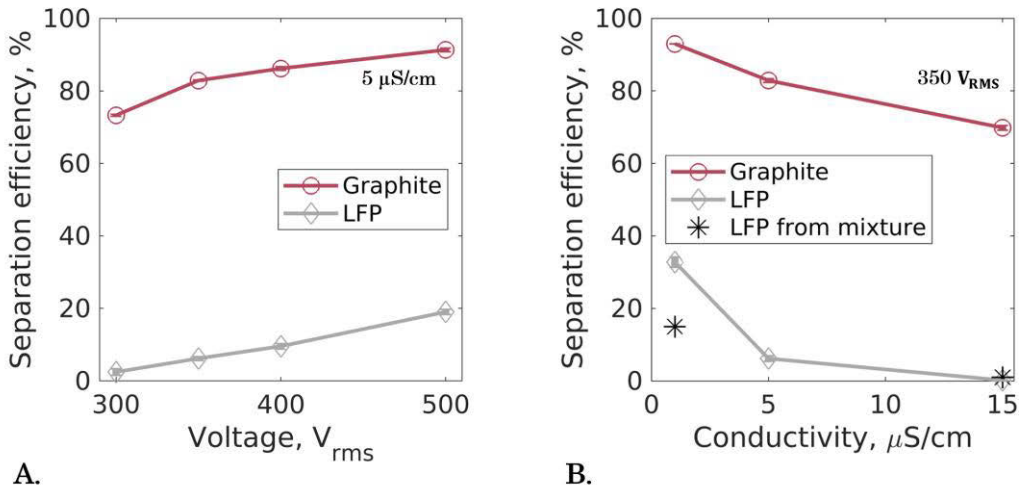

FIGURE 6.3 A: DEP trapping efficiency of powders at 15 kHz, with a 360 mL/h flow rate. A: Dependence on the voltage (at 5 µS/cm conductivity); B: dependence on the conductivity (at 350 V_{rms} voltage) with respective standard deviations from three repetitions. Image and caption, adapted from the author's paper [24], CC BY 4.0.

The trapping efficiency of LFP is minimal at 300 V_{rms}, but it shows a separation of nearly 20% at 500 V_{rms}. Moreover, it was noted that LFP trapping diminishes with higher solution conductivity (Figure 6.3). While at 1 µS/cm and 350 V_{rms}, LFP trapping exceeds 30%, at 15 µS/cm, it plummets to 1%. The decrease was also seen for graphite trapping efficiency with higher conductivity to some degree, from 90% at the lowest conductivity to 70% at the highest. Consequently, at 15 µS/cm, LFP trapping is negligible, whereas graphite trapping remains substantial. The reason why LFP exhibits higher trapping at lower conductivities is uncertain. Its bulk conductivity is estimated to be below 1 µS/cm, and microscopy experiments have shown that LFP exhibits nDEP at 30 µS/cm. Conducting microscopy experiments at lower conductivities was not feasible, as the required particle concentration was too high to reach those lower values. A slight decrease in graphite trapping efficiency is linked to thermal effects in suspension at high conductivities. This assumption is consistent with other observations made with polystyrene particles, where it was derived that an increase in conductivity raises temperature due to higher energy dissipation. It amplified the fluid's natural convection, assisting for "undirected" fluid motion [21].

A combined mixture of both suspensions - particles was prepared to divide graphite from a mixture of graphite and LFP of similar size. The AAS was utilized to measure the trapping efficiency of LFP at 15 kHz, 350 V_{rms}, at two different solution

conductivities, 1 and 15 µS/cm. The trapping efficiency of LFP in the tests, represented by stars in Fig. 6.3, showed that LFP exhibited approximately 1 % trapping efficiency at 15 µS/cm and around 15% at 1 µS/cm, almost mirroring the results of the pure particle experiments. Some mismatches in the exact efficiency numbers can be explained by the following. There is almost an absence of separation of the LFP at the conductivity of 15 µs/cm; thus, at any analysis method chosen, the results would show values around 0 %. Additionally, there would be a difference caused by the difference between the measurement methods. The author's colleague in 2023, Jasper Giesler discovered and discussed this in detail [123]. AAS is designed to quantify the concentration in a liquid sample by examining light absorption at distinct atomic absorption lines. On the other hand, the spectrometer reflectance measurements only address the result qualitatively, as it detects the intensity of light reflected from the unspecified solid target particles in the suspension. Therefore, reflection measurement provides a qualitative estimate, while AAS detects lithium content for more accurate results, as previously noted [123]. The graphite concentration in mixture experiments was not conducted, so it is assumed that graphite exhibits a separation efficiency identical to that in separate suspension experiments.

III Summary of the results of this part

The findings illustrate that manipulating the liquid medium's conductivity facilitates selective separation of graphite from a mixture with uncoated LFP using DEP filtration. It was established that LFP exhibits negative DEP while graphite exhibits positive DEP. The conductivity threshold necessary for this separation was identified, thereby validating the concept of sorting non-carbon-coated lithium iron phosphate ($LiFePO_4$) and graphite.

In a previous study conducted by the same research group as the author's, graphite particles were separated from considerably smaller carbon black-coated LFP particles using pDEP in electrode-based dielectrophoresis [123]. Despite both particles exhibiting pDEP, separation was achievable due to the volume-dependent nature of the DEP force. The results from this chapter demonstrate that graphite particles can be captured from uncoated, i.e., non-conductive, LFP particles of similar size using dielectrophoretic filtration.

It shall be noted that separating commercially available particles was successful; however, applying this method to real black mass with graphite-coated LFP introduces additional challenges. Several aspects to consider would be the concentration of the mixture, potential clogging of the filter with higher loads, and impurities present in the black mass. In the case of the more concentrated mixtures, one shall account not only for potential agglomerations of these particles but also for the ability of the porous filter to hold the target particles in their position while the electric field is still on. The author's colleagues have already explored the pathway toward the filter capacity in previous works [21,123]. Further investigation is needed to assess the recovery rates.

Chapter 7: Modified porous filter: conductive particles

This chapter aims to answer whether metal particles (inclusions) would be of interest as a part of the hybrid filter at very low frequencies (≈1 kHz) and which impact they would make on DEP filtration of potential mixtures. As an example of these metals, noble ones, such as gold, is taken for the simulations. The content in this chapter summarizes unpublished simulations of the first year of the author's PhD.

As was stated in the Chapter 4, a hypothesis was that presence of a metal inclusion in the porous filter increases field inhomogeneity while comparing to the situation when no metal inclusion is present there.
In this chapter, two models are introduced: a simplified two-dimensional sponge model and a two-dimensional "one pore model". The sponge model aims to illustrate particle trajectories and DEP trapping in the porous medium. The "one-pore model" demonstrates the effect of metal inclusion addition. In this model, to represent two extreme cases, metal inclusions with varying sizes were deposited next to field maxima and next to field minima. This model adaptation is based on the model developed in Malte Lorenz's thesis (2021) [44].

I Materials and methods

This section provides the details on the conducted simulations. All simulations were done in COMSOL Multiphysics, using AC/DC module to calculate the electric field distribution across the filter geometry. In all the current simulation, the electric field and the flow are applied along each other.

I.1 First simulation. Two-dimensional sponge model

Generally, as discussed in the theory section of DEP, target particles are affected by the DEP force when they enter the inhomogeneous electric field regions. A simplified 2D porous geometry is constructed from an inspiration of micro-computed tomography scan. This artificial porous filter had certain geometrical parameters (Figure 7.1), which are summarized in Appendix 1.

In the simulations, the electric field was simulated with "electric currents" in COMSOL Multiphysics. An assumption was a charge-free space and the materials in use which are homogeneous in their nature. An artificial 2D dielectric porous structure in the simulation was represented by the solid domain, defined as a solid isotropic material with pore openings. The material was set to a relative permittivity of 9.14 and a very low electric conductivity of 10^{-14} S/m to represent a dielectric, positioned in the very low frequency fields. The tips of the sharp edges were kept everywhere to a circular form of 2 μm in radius. This estimation is used as an assumption of the sharpness of the tips, as that parameter was not measured in CT data.

The "aqueous" medium, which filled the filter, was defined as a second domain (marked light blue in Figure 7.1). It was assumed as a low-viscosity (10^{-3} Pa·s) incompressible fluid with a global pressure of 1 bar. It had material parameters of a relative permittivity of 80.2 and electric conductivity of 2×10^{-4} S/m. The material properties of the medium aimed to show a similarity to deionized water in the very low-frequency domain, which is commonly used in dielectrophoretic filtration experiments. The electric field in the simulation was applied in the direction of fluid flow and with an assumption of the uniform potentials along the upper and the lower boundaries. The flow profile was assumed to be laminar with a fully developed velocity in the inlet (left of the Figure 7.1) and no slip boundaries at the filter wall (resulting in the null velocity there).

The target particles passed through the structure. The target particles were assumed to possess negligible inertia in the simulation for computation simplicity. For the results part, the velocity of each i'th particle was calculated using Equation (2.43) and further visualized as particle trajectories. These target particles represent a similarity to polystyrene particles, which are broadly used in DEP filtration experiments. They had d_p being 4.5 μm, and f_{CM} set to its maximum value 1. The goal was to set a low voltage setting and the fixed flow ($\approx 26\ \mathrm{kV_{rms}/m}$, 812 μm/s) for the visualization of the behavior of 50 target particles. No variation of these parameters was done in the first model.

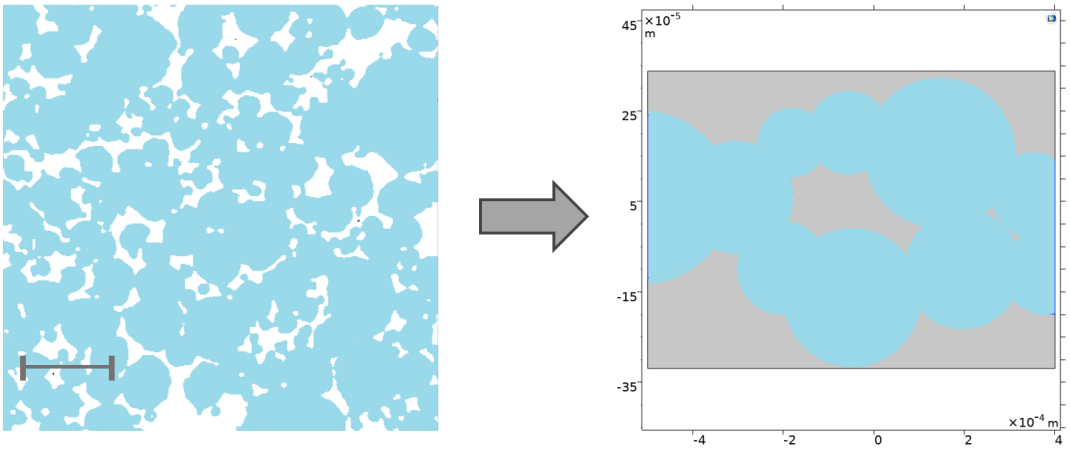

FIGURE 7.1 An example of the μCT structure of the porous filter [in a.u.], obtained from the raw data of Malte Lorenz [44] and the artificial 2D pore model. The pores in the artificial structure vary in the dimensions of $\mathbf{0.85 \times 10^{-4}}$ to $\mathbf{1.5 \times 10^{-4}}$ m in radius[119]. The length in-between the electrodes is $\mathbf{9 \times 10^{-4}}$ m here.

I.2 Second model. "One pore model"

The second model depicted only one pore opening of the structure. This "one-pore" structure had a 300 μm pore (as in Figure 7.2). It was a geometrical structure from the model used in Malter Lorenz's thesis (page 57)[44], with implemented metal inclusions and parametric connections. This was done by the author to build up the adapted model on the knowledge already existing in the DEP field. In this adapted model, close to the inlet of the pore, the metal inclusion was represented as a sphere placed at two different positions (not simultaneously). The first position of the metal was in the low field region of the pore (named below as "the first"). The other one was located closer to the ceramic tip (named below as "the second"). Their sizes were varied in a parametric sweep setting of COMSOL Multiphysics. The metal inclusion was assumed as gold with a conductivity of 4.1×10^7 S/m, and a relative permittivity of 1.

The assumptions for the fluid, target particles, and dielectric filter material were the same as in the previous model. The field strength here was set to $26-75\ \mathrm{kV_{rms}/m}$, the flow velocity was set to 10–812 μm/s. The estimation of the upper field strength and the speed of flow came from the setup limitation, which can be overcome by equipment changes (for example, the current volumetric pump has a limit of 11 mL/min, which translates into the specific cross-section of the flow to ≈1200 μm/s and the current amplifier allows for a stable voltage of up to 600 V_{rms},

which then translates to 75 kV_{rms}/m). The trajectories of the particles were calculated in the same manner as in the first model.

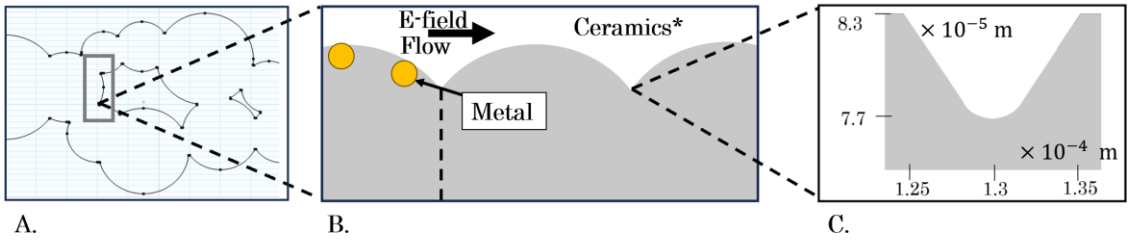

FIGURE 7.2 A schematic of the one-pore model A. The 2D cut structure. B: A one-pore construction: the visualization of the metal inclusion of two investigated positions in a region before the pore window. C. The geometry of the "sharp" corners of the pore.

Two main variables were under investigation. The size of the inclusion was varied from 100 nm to 15 μm in radius. And the window-to-pore ratio of the pore was set to 0.25, 0.5, or 0.75 (not simultaneously). The lower limit of the specification (100 nm) comes from a perspective to test out in the future experimentally the hybrid filters, produced from the cooperation with Tongwei Guo, who was a member of the same graduate school as the author of this thesis [124,125]. It should be noted that for the simulations with sizes larger than 100 nm, it is assumed unnecessary to consider possible quantum effects that were not in the scope of classical modeling, and in this size scale will not play a major role [126].

The central data in the second model was the number of the trajectories of the target particle that changed. In this context, an important factor was the separation efficiency, as outlined in Table 7.1. There, the total efficiency includes the trapping efficiency of the structure and the metal together. The number of particles used in this simulation was 50 for the study on the impact of the metal inclusion and 10 for the study on the impact of the pore-to-window ratio.

Efficiency total, %	Efficiency metal, %
$\text{Efficiency total (\%)} = \frac{100N_{\text{exit}}}{N_{\text{total}}}$	$\text{Efficiency metal (\%)} = \frac{100N_{\text{metal}}}{N_{\text{total}}}$

TABLE 7.1 Separation efficiency metric in simulations.

II Results and discussion

In this section results from two models are summarized.

II.1 First model: highlighting the effect

In the first simulation model, trajectories of target particles with enabled or disabled electric fields were visualized in the artificial sponge structure (Figure 7.3). The low-field regions are the smooth pore parts and are represented in blue color in panel A, Figure 7.3. As shown in panel C Figure 7.3, target particles are trapped in the regions of the high gradients of the electric field, and in this particular setting, this led to a total efficiency of 18 % in the presence of 50 particles. Pores with different sizes led to different local trapping efficiencies inside the pores.

While porous structures indeed have a "random" pore distribution inside the filter sponge, that setting would not be a good fit for the metal inclusion study. To study the influence of a metal inclusion, there is a need to fix the major DEP separation efficiency parameters such as size of the pores, electric field strength, the speed of the fluid flow, the size and location of the metal inclusions. This is accomplished in the second "one-pore" model.

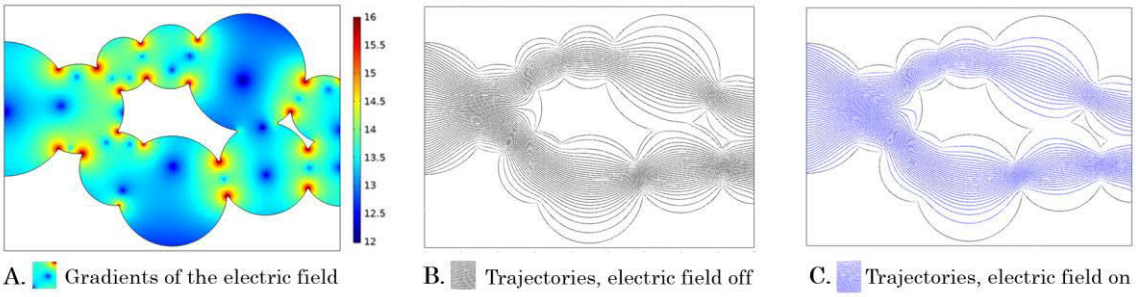

FIGURE 7.3 2D pore geometry A: The distribution of the electric field gradients B: Trajectories in the absence of the electric field C: The electric field is at **26 kV_{rms}**/m, flow of 812 μm/s.

II.2 Second model: inclusion changes, feasibility evaluation

Here, in the second model, the goal was to reveal the quantitative influence of the metal inclusions positioned near the maximum and the minimum of the electric field. Figure 7.4 shows the two positions of the metal. The metal inclusions of the largest size (15 μm) are visualized. In this figure, no electric field is applied, and 50 target particles are present in the system.

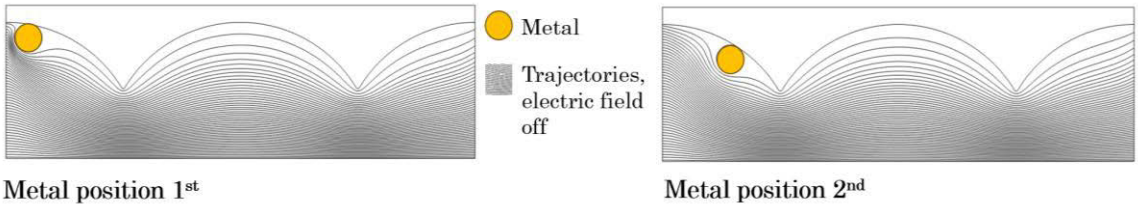

FIGURE 7.4 One example of the simulation of two locations of the **15 µm** metal inclusion in the one-pore model, with the parameters of the experiment of 0 $\mathbf{V_{rms}}$

The first parameter varied was the size of the metal inclusion. It was changed at two specific positions, subsequently. The impact of the metal inclusion was recorded with the metric "Efficiency metal", reflecting only those particles which were captured by the inclusion, and "Efficiency total", reflecting the total amount of the particles captured by the dielectric structure and the inclusion together (Figure 7.5). The results are in Figure 7.6.

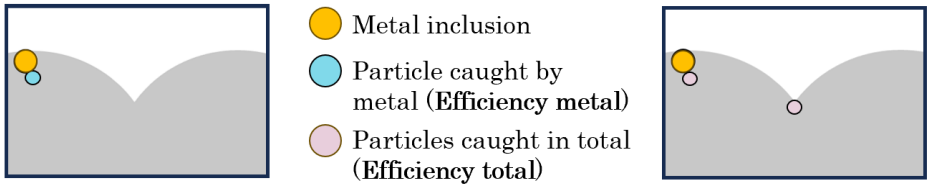

FIGURE 7.5 Total and local (metal) efficiencies representation.

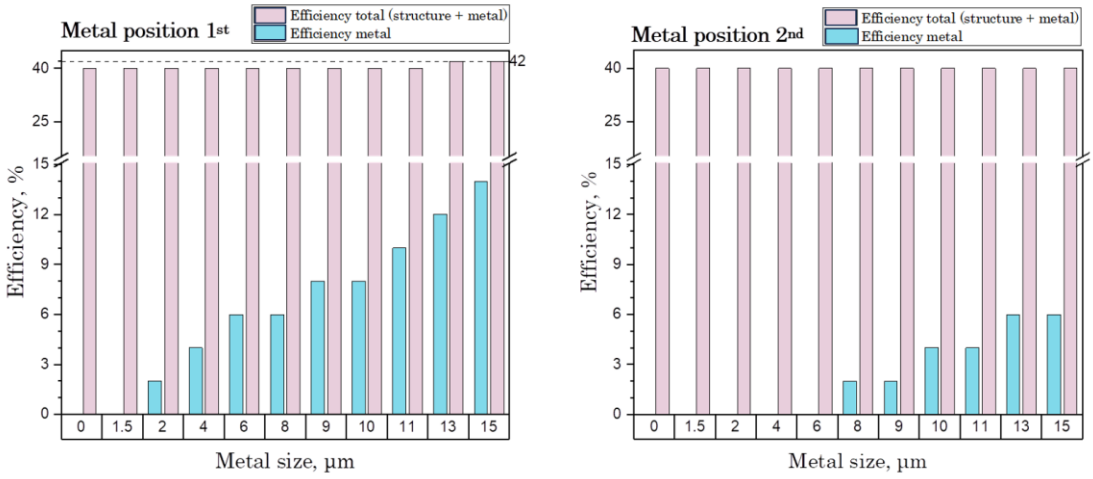

FIGURE 7.6 Total trapping efficiency which is a sum of both metal and sharp edge efficiencies, depicted in rose color and metal trapping efficiency in blue color as a function of metal inclusion size. This was conducted at maximum parameters of the flow and electric field: 75 kV_{rms}/m, 812 µm/s.

The pore-to-window ratio was set to 0.5. The electric field was applied with 50 target particles (Figure 7.6). The simulation was performed at the maximized setting of the flow rate and voltage (812 μm/s, 75 kV_{rms}/m).

Small metal inclusions did not contribute to particle trapping. For inclusions in the first position, metal trapping was only occurring for the inclusions which were 2 μm or larger. For metal inclusion in the second position, the inclusion had to be 8 μm or larger. Overall, only the first metal inclusion made an impact on the total trapping efficiency at sizes of 13 and 15 μm (2 % improvement to the total efficiency). A trapping efficiency improvement means that the metal inclusion caught the particles that were otherwise not caught by the ceramic tip in the absence of the metal. For the smaller-sized metal inclusions, the DEP force is very high, however, only in the region close to this inclusion. Thus, the effect was too localized to attract the target particles: no enhanced effect in DEP trapping was observed for the metal inclusions, which were 100 times smaller than the pore diameter.

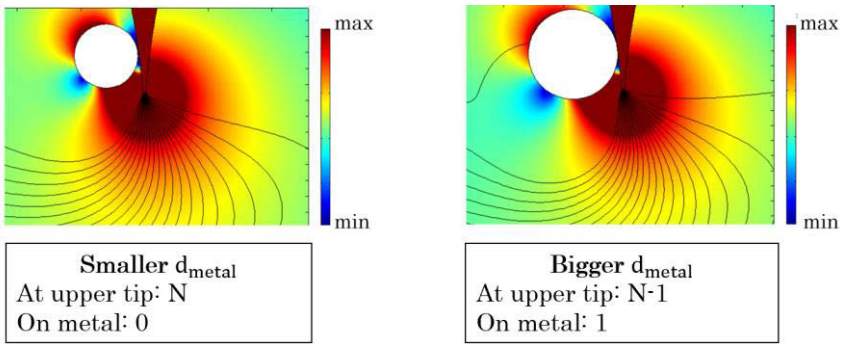

FIGURE 7.7 The second metal position schematics. The gradients of the electric field from two different sizes of the metal inclusion and an effect of the "stealing" of the target particle from the ceramics tip. The red indicates the electric field maxima (which attracts TP using pDEP). The TP trajectories are shown in black color.

Additionally, for the second metal position, when the inclusion's gradients affect a wider spatial region, the target particles, previously attracted to the filter tip, get "stolen" by the metal inclusion (Figure 7.7). Therefore, the second inclusion (Figure 7.4), located close to the ceramics tip, did not capture new target particles but took those that would otherwise be attached to the tip. That led to constant total efficiency which was not increased by the presence of metal.

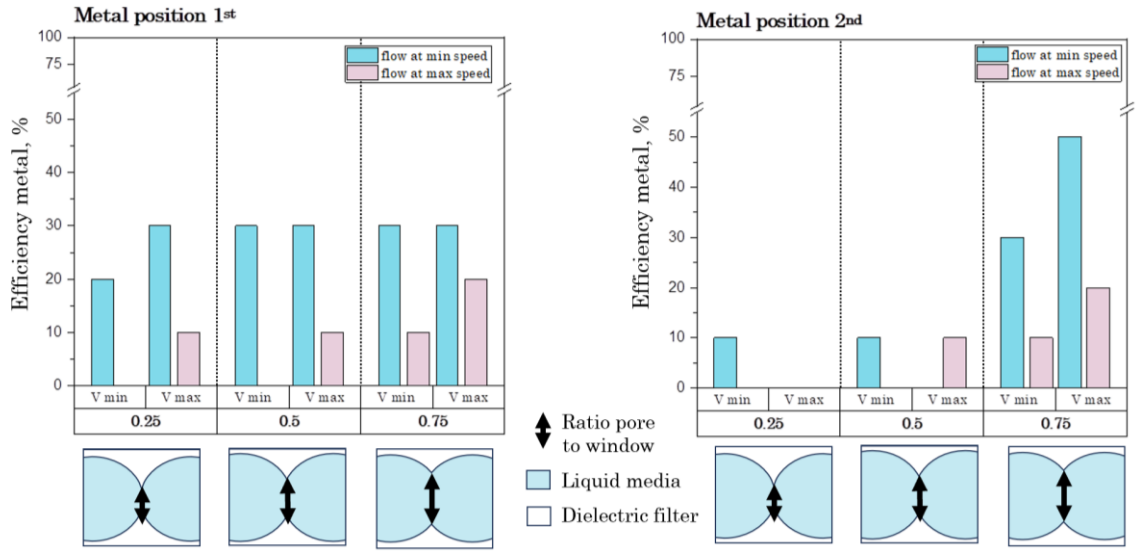

FIGURE 7.8 A voltage (denoted as V min or Vmax) and speed of flow (denoted in blue and rose color) as a function of separation efficiency for different pore-to-window ratios.

The pore-to-window ratio was varied between 0.25, 0.5, 0.75 (Figure 7.8). An influence of the geometrical pore opening was checked for both metal inclusions, with the assumption that the metal particle has a max size of 15 μm. The efficiency metal (%) stands for the particles caught by the metal out of the total number of the particles. Total number of particles in this test was set to 10.

At the lower flow rates, the trapping is higher, which is consistent with DEP theory. At the maximum values of the voltage, it was possible to see trapping on the high speed of flow for the metal inclusion in position 1 (rose bars, indicating max flow, are present for all the pore-to-window ratios at maximum voltage). For the metal inclusion in position 2, the trend is the same only for the pore-to-window ratio of 0.75. For the pore-to-window ratio of 0.5, the trapping at minima voltage happened only for the slow flow. The maximum voltage showed no trapping at the minimum speed of the flow. A similar trend was observed for the highest voltage in the 0.25 pore-to-window ratio. That suggests that the influence of the electric field gradient was stronger than that of the flow parameters and that potentially originates from the fact that inclusion at the second position is located next to the sharp edge of the "one pore" model. It is also visible that the pore-to-window ratio of 0.25 is undesired for both inclusion locations. That is most likely due to the fact that the metal is then located in the global minima of the electric field gradients and therefore hardly influences the particle's trajectories from there. The increased efficiency of metal for

0.75 pore-to-window ratio of the pore might be due to the closeness of a ceramic tip to the inclusion.

In total, overall trapping efficiency of the deposited metal inclusions would depend strongly on their size, location in the porous filter (near field max or field min), sharpness of the tip, and field strength applied. Moreover, another electrokinetic phenomenon, such as induced-charge electro-osmosis (ICEO) flow, must also be considered to further investigate its effect in simulations to see if the target particles are indeed reaching the global minima regions of the electric field close enough to be in the region of the inclusion's field gradient. One shall also note that in the current "one-pore" structure, essentially, two aspects are changing: the material boundary (by the introduction of the metal itself) and the geometry of the pore (by the introduction of inclusions on the pore surface).

III Summary of the results of this part

In this part, a simplified simulation was done to delve into the complex world of implementing conductive boundaries into the filter sponge matrix at the very low-frequency field. The results have shown that implementing metal in a way that allows for μm range metal particles to be present within the porous filter configuration might be promising but is challenging. An increase in the DEP efficiency was only detected when the particle was sufficiently large in size and located in the minima of the electric field. While the efficiency of the metal inclusion would certainly depend on the pore sizes of the filter and the "sharpness" of the edges in the filter, currently, the deposition of the nanoparticles made of metal inside the sponges is not recommended for the DEP filter. In the case of particle sizes smaller than 1 μm, the gradients induced by the metal particles were shown to be too localized to influence the target particles. Significantly larger metal inclusions (compared to the pore sizes) would lead to relatively lower and less local gradients, potentially increasing the spatial region of the DEP filtration, but also decreasing the effective pore size and thereby increasing the potential mechanical trapping. Additionally, the position of the metal inclusion concerning the minima and maxima of the electric field seems to be an uncontrollable factor in most deposition methods [124,125]. Furthermore, a hybrid filter causes concerns due to surface potential differences in the materials used. Under certain circumstances, target particles might predominantly stick to the metal inclusions, thereby hindering DEP selective material trapping.

Chapter 8: Conclusions and outlook

This thesis aimed to improve the understanding of separation performance in DEP filtration with macro-sized filters in the form of the packed bed. Primarily, the focus was on geometric aspects of the filter, as was inspired by the pore geometry rules in microfluidic DEP. Secondly, a small exploration of the impact of material changes was made for the case of metal nano-inclusions. Thirdly, dielectrophoretic filtration was studied for a societally relevant material separation task from the field of battery recycling, with an ambition to link both fundamental and applied research.

DEP filtration of polystyrene micro-particles of 500 nm was used as a model system to probe the impact of pore structure in a packed bed filter. Using three different filter matrices, with different pore structure but similar porosities, it was shown that the amount of edges of the filter surface has a bigger influence than the grain size. That enabled a new perspective on the packed bed filter design for dielectrophoretic filtration. It highlighted the need for research devoted to the characterization of angular grains and their filtration capabilities. Because the highest separation efficiency differences were observed at the high voltages, any follow-up on the grain morphology study should include electric fields strengths up to at least 75 kV/m. One idea for further investigation on influences of edgy and smooth particles can be a focus on narrow size distributions of the grains (e.g., 200-205 µm) and assembly of these grains between microscope slides in a configuration similar to a 3D iDEP chip[127,128]. It would allow for a very straightforward basic study with selected target particles, providing clear visibility of the trapping process. Furthermore, to judge the usability of a packed bed filter with modified grains towards industrial applications in the field of recycling, the separation efficiency and recovery of metal powders should be investigated additionally for DEP filtration, as metal powders would differ in shape and possess a significantly higher conductivity than PS particles.

In this thesis, the feasibility of a hybrid metal-dielectric sponge filter was explored. The potential of the performance of nanoparticle-coated ceramic sponges for DEP was investigated with 2D simulations. It was concluded the separation efficiency of such a structure would depend on the position of the metal inclusions and the ratio between the size of the inclusion and the pore size. However, the simulations showed the inclusions in these sub-micron size ranges would not enhance a total separation

efficiency of the filters. Besides, due to previously mentioned concerns on “sticking” of some types of the particles to the metal inclusions, such hybrid filters are unlikely candidates for applications of mixture separation for the future.

From an application side, the thesis findings demonstrate a proof-of-concept that dielectrophoretic filtration can be applied to recycling of battery materials in the context of an additional separation step. A feasibility experiment was accomplished with a mixture of uncoated LFP and graphite particles, which showed that by tuning the liquid media's conductivity, the particles' polarizability difference would lead to selective trapping by DEP. With the data obtained from the geometrical filter parameters, combined with research on LFP and graphite recovery rates, one can move further in this direction.

Generally, the author finds it essential to select a filter material for the applied task based on the particles of interest; in particular, choose a filter that allows for straightforward and inexpensive scale-up of the setup (such as packed beds), select a material of the filter with surface potential that avoids undesired adhesion of the particles to it, and select a morphology of the filter matrix that avoids mechanical trapping caused by the pore sizes. Besides, the overall filter should ideally be cleanable without the usage of harsh chemicals. Correct tuning of the suspension or the overall experimental setup shall also be arranged (such as adding surfactants, implementing a stirring magnet inside the suspension, etc.), to allow for proper mixing of the particles.

It shall be noted that the separation of waste LFP from graphite remains a real challenge, not only because real LFP recovered from batteries would have a different surface composition, but also because it would contain impurities (which might lead to degradation of the material, changes in the polarizability, etc.). Therefore, the research in this thesis is only an intermediate step towards this bigger challenge, which is needed to show the feasibility of DEP in the battery recycling field.

Additional information

Appendix 1

Model parameters of simulations

In the simulations "electric currents (ec)" and "laminar flow (spf)" were mostly used in the models.

The DEP trajectories were visualized as:

$$\mathbf{u_{1,x}} + 2\mu_{\mathrm{DEP}} \cdot \mathrm{d}(\mathrm{ec.E}_x^2 + \mathrm{ec.E}_y^2, \mathrm{x})$$
$$\mathbf{u_{1,y}} + 2\mu_{\mathrm{DEP}} \cdot \mathrm{d}(\mathrm{ec.E}_x^2 + \mathrm{ec.E}_y^2, \mathrm{y})$$

Where μ_{DEP} is defined as:

$$\mu_{\mathrm{DEP}} = \frac{d_p^2 \varepsilon_{\mathrm{water}} f_{CM}}{24\eta_{\mathrm{water}}}$$

Here $\eta_{\mathrm{water}} = 1 \cdot 10^{-3}$ Pa · s and $\varepsilon_{\mathrm{water}} = 80.2\varepsilon_0$, and $f_{CM}$the Clausius-Mossotti factor.

Voltage in the simulation is defined as:

$$V = \frac{V_{ex}}{L_{ex}} \cdot S_v,$$

Where V_{ex} stands for V_{rms} in the experiment, L_{ex} stand for the distance between the electrodes (in which the porous filter is located) and scaling factor S_v which represents the distance between the applied voltages in the simulation and scales the "one-pore" geometry to the required filed strength in the following way:

$$S_v = d_{\mathrm{pore}} + 2(d_{\mathrm{pore}} - \delta)$$

Where d_{pore} is the diameter of the pore and δ represents the specific distance between the two pores (the details on the constructions are given in Reference [119]). In the first model, $S_v = \mathbf{9 \times 10^{-4}}$ m.

Appendix 2

Installation of the packed bed filters

The content of this section is an identical copy from the supplementary materials of the author's publication from 2023 [1] (distributed under CC BY 4.0).

FIGURE A.2.1 Packed bed of sand inside the filter cell (located between two metal electrodes)[1].

To verify that filter loading procedure is consistent, the sand filter (mesh 250) was tested out three times (resulting in testing of three different fractions referred below as three different packs taken from the storage reservoir). This experiment was done by two different people for statistics purposes. The DEP filtration efficiency (Fig. A.2.2) remained consistent within the packs and therefore the measurement with the packed bed grained filer is considered to be sufficiently stable in this setting.

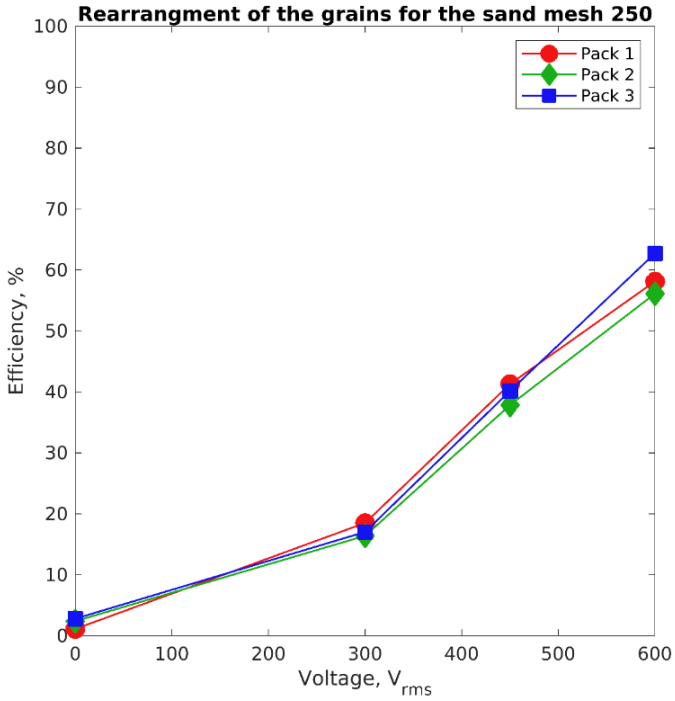

FIGURE A.2.2 DEP efficiency of the sand filer (mesh 250), which was loaded in three different packs to the setup. The values at the highest voltage differ no more than ±3 % from their mean value and fit to the expected range. The experimental parameters are 1 kHz, 11 ml/min, target particles are identical to those in the main manuscript (PS 500 nm)[1].

Appendix 3

Mechanical trapping

The content of this section is an identical copy from the supplementary materials of the author's publication from 2023 [1] (distributed under CC BY 4.0).

It should be noted that among all samples, sand filters demonstrated the highest mechanical trapping rate for all the size fractions (Table A.3).

0 V trapping, %	Glass beads	Sand	Crushed glass
150 mesh	0.1 ± 0.1%	1.6 ± 0.3%	0.7 ± 0.8%
250 mesh	0.4 ± 0.2%	0.9 ± 0.2%	0.8 ± 0.6%
355 mesh	1.4 ± 0.7%	1.4 ± 0.5%	1.3 ± 0.8%

TABLE A.3 Mechanical trapping of PS particles at 11 ml/min among different filter materials. here the efficiencies are calculating as mean values from n ≥3 experiments with their standard deviations[1].

Appendix 4

PSD details

The content of this section is an identical copy from the supplementary materials of the author's publication from 2023 [1] (distributed under CC BY 4.0).

Mesh		d10, µm	d50, µm	d90, µm	D [3, 2], µm	D [4, 3], µm	SPAN value
150	Sand,	164.7	228.1	315.2	220.8	235.2	0.66
	COV	0.5%	0.5%	0.5%	0.5%	0.5%	
	Glass beads,	169.8	232.2	317	225.9	239.2	0.63
	COV	2.0%	2.2%	4.3%	2.1%	2.6%	
	Crushed glass,	160.2	228.1	326.6	220.0	237.3	0.73
	COV	2.9%	7.3%	13.0%	5.9%	7.5%	
250	Sand,	266.7	365.2	497.1	354.2	375.7	0.63
	COV	0.6%	0.6%	0.5%	0.6%	0.5%	
	Glass beads,	235.6	321.7	439.2	312.8	331.4	0.63
	COV	1.1%	1.2%	1.5%	1.1%	1.2%	
	Crushed glass,	266	389.7	568.5	372.9	405.8	0.78
	COV	1.5%	1.8%	2.6%	1.7%	2.0%	
355	Sand,	358.5	492.7	672.2	478.3	506.9	0.64
	COV	0.9%	2.5%	5.2%	2.3%	3.2%	
	Glass beads,	348	473.9	641.4	460.4	486.0	0.62
	COV	1.0%	2.0%	3.4%	1.9%	2.2%	
	Crushed glass,	395.7	550.2	767.3	532.9	569.1	0.68
	COV	5.3%	3.2%	1.7%	3.6%	3.0%	

TABLE A.4 Main parameters of particle size distribution of the three types of packed bed samples in three size fractions with indications (in %) of the coefficients of variation of these parameters obtained in the reproducibility tests with a repetition rate of $n \geq 3$. COV calculation is based on the standard deviation of the values. Additionally, parameters of surface-weighted mean d[3, 2] (most sensitive towards fine particles) and volume-weighted mean d[4, 3] (most sensitive towards coarse particles) are shown for a complete comparison. The span value is characterizing the distribution width and was calculated as $\frac{D_{90}-D_{10}}{D_{50}}$ [1].

Appendix 5

µCT filter structural results

The content of this section is an identical copy from the supplementary materials of the author's publication from 2023 [1] (distributed under CC BY 4.0).

Parameters	Glass beads mesh 250	Sand mesh 250	Sand mesh 355
Tortuosity	1.62	1.74	1.69
Porosity, %	43	35	38
Permeability, m^2	1.29×10^{-6}	3.41×10^{-7}	1.17×10^{-6}
Hydraulic pore diameter (mean), µm	157	132	151
Throat (pore window) equivalent diameter (mean), µm	78	59	74
Sphericity of the pores (mean)	1.667×10^{-1}	3.34×10^{-4}	4.45×10^{-4}
Specific surface area, mm^{-1}	11.3	14.2	10.8

TABLE A.5 Summary of the main parameters extracted from the CT scans of the packed bed samples based on the analysis[1].

Appendix 6

PSD of the target particles of LFP and graphite

The content of this section is an identical copy from the author's publication from 2024 [24] (distributed under CC BY 4.0).

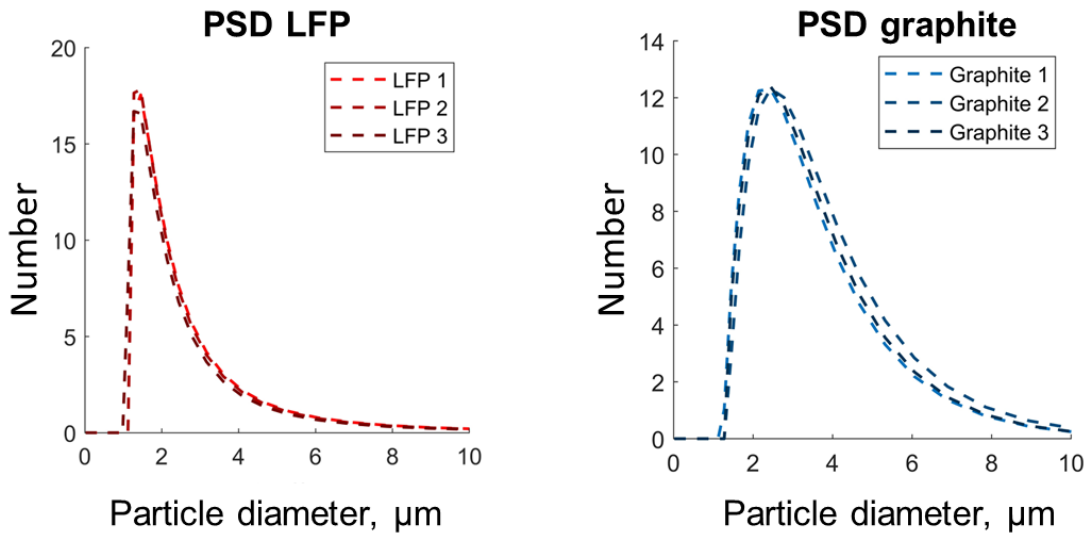

FIGURE A.6. Particle size distribution (PSD), number-based, and additionally normalized distribution of two-particle systems (LFP and graphite) were measured three times with laser diffraction[24].

Contributions to the articles

M. Kepper, G. Pesch, M. Baune and Thöming J. conceived the experiments. G. Pesch and M. Baune supervised the project. M. Kepper conducted the experiments and arranged the data curation. N. Karim provided the µCT processing results for the packed bed samples and wrote the details about the processing. M. Kepper and G. Pesch analysed the results. M. Kepper wrote the original manuscript with input from all other authors.

M. Kepper and G. Pesch conceived the experiments, validated the data and were responsible for the project administration. G. Pesch supervised the project. M. Kepper did the experiments and analysed the results. J. Thöming was responsible for the resources. A. Rother was responsible for formal analysis of the AAS data and the curation of the overall gather data. M. Kepper wrote the original manuscript with input from all other authors.

M. O'Donnell, M. Kepper, G. Pesch conceived the study. G. Pesch supervised the project. M. Kepper wrote the detailed table of literature which was used in the review. M. O'Donnell wrote the original manuscript with input from all other authors.

Concerning the contributions in the not published materials, TU Bergakademie Freiberg arranged angularity measurements in Chapter 5 of this thesis and provided the data for the analysis.

List of symbols

Symbol	Meaning
$\mathbf{F}$	Force vector
Q_1, Q_2, Q	Static charge
r	Distance between charges
ε_0	Vacuum permittivity constant
$\mathbf{r}_{12}$	Vector directed from one charge to another
$\mathbf{E}$	Electric field
$\mathbf{r}$	Position vector
$\mathbf{p}$	Dipole moment
U	Potential energy
$\boldsymbol{\nabla}$	Gradient operator
φ	Scalar potential of the electric field
σ_ρ	Surface charge density
ΔS	Surface element
ρ	Volume charge density
ΔV	Volume element
Φ	Electric flux
$\mathbf{n}$	Surface outward normal vector
$\rho_\mathrm{f}, \rho_\mathrm{b}$	Volume density of free and bound charges
$\mathbf{D}$	Electric field displacement vector
$\mathbf{P}$	Polarization vector
χ_{ae}	Electric susceptibility
ε_r	Dimensionless relative permittivity
ε	Absolute permittivity
σ	Conductivity
$\mathbf{J}$	Current density
ω	Angular frequency of the electromagnetic field
i	Imaginary unit
$\hat{\varepsilon}$	Complex permittivity
C	Capacitance
d	Distance between capacitor plates
Z	Impedance
R	Resistance
ω_p	Metal plasma frequency
$\hat{\sigma}(\omega)$	Complex frequency-dependent conductivity
t_a	Average time between electron collisions
ε_∞	Permittivity at infinite frequency
E_0	Electric field amplitude

J_0, J_1	Bessel function of the first kind of order zero and order one
c	Speed of light
$\mathbf{e}_r,\ \mathbf{e}_\phi, \mathbf{e}_z$	Unit vectors of the cylindrical system of coordinates
$\mathbf{H}$	Magnetic field
χ_{or}	Low-frequency limit for orientational susceptibility
ε_s	Permittivity of DC electric field
τ_{or}	Orientational relaxation time
$\varepsilon_p, \varepsilon_m$	Permittivity of particle and permittivity of medium
$\tilde{\alpha}$	Effective polarizability
τ_{MW}	Relaxation time in Maxwel-Wagner model
r_p	Radius of the sphere
f_{CM}	Clausius–Mossotti factor
$\mathbf{E}_{\mathrm{rms}}$	Root-mean-square electric field
$\mathrm{V}_{\mathrm{rms}}$	Root-mean-square voltage
k^{-1}	Debye length
T	Temperature
k_B	Boltzmann constant
Q_-	Electron charge
c_{ion}	Ion concentration
z	Valence
$\sigma_p, \sigma_{p,bulk}, \sigma_m$	Conductivity of the particle, bulk conductivity of the particle, conductivity of the media
K_{s}	Surface conductance
f_{DL}	Frequency to fully charge the double layer
ρ_{FL}	Fluid density
Π	Pressure
$\mathbf{u}$	Fluid flow velocity
η	Dynamic viscosity
R_n	Reynold's number
u_0	Characteristic velocity of the fluid
l_0	Characteristic scale
St	Stokes number
ρ_p	Particle density
η_D	Friction coefficient
μ_{DEP}	DEP mobility
$\boldsymbol{\psi}_{\mathrm{i}}$	Position vector for i^{th} DEP target part
D	Diffusion coefficient
P_{ec}	Peclet number
C_D	Capacitance of the diffuse layer
τ_{EL}	Relaxation time to charge DL
$\mathbf{v}_{\mathrm{ICEO}}$	Velocity of ICEO flow

c_e, c_0	Concentrations of particles when electric field is on and off, correspondingly
c_r, c_t	Concentrations of released and trapped concentration of particles, correspondingly
q_flow	Volumetric flow rate
S_F	Cross-sectional area of the filter
κ_p	Permeability coefficient
L	Flow length in the filter
V_p	Pore volume
S_p	Surface area of the pore

List of acronyms

Acronym	Meaning
AAS	Atomic absorption spectroscopy
AC	Alternating current
CM	Clausius-Mossotti
COV	Coefficient of variation
CT	Computed (X-ray) Tomography
DC	Direct current
DEP	Dielectrophoresis
DL	Double layer
DS	Dukhin-Shilov
eDEP	Electrode-based dielectrophoresis
EO	Electroosmosis
ICEO	Induced-charge electroosmosis
iDEP	Insulator-based dielectrophoresis
LbL	Layer-by-layer
LFP	Lithium iron phosphate
LIB	Lithium-ion battery
micro-CT, µCT	Micro Computed (X-ray) Tomography
MW	Maxwell-Wagner
MWO	Maxwell-Wagner-O'Konski
nDEP	Negative dielectrophoresis
pDEP	Positive dielectrophoresis
PS	Polystyrene
PSD	Particle size distribution
PVC	Polyvinyl chloride
RMS	Root-mean-square
R&D	Research and development
SEM	Scanning electron microscope
STD	Standard deviation
TP	Target particle
TU	Technical University

Bibliography

1. Kepper, M., Karim, M. N., Baune, M., Thöming, J. & Pesch, G. R. Influence of the filter grain morphology on separation efficiency in dielectrophoretic filtration. *Electrophoresis* **44**, 1645–1654 (2023).

2. Ahirwar, R. & Tripathi, A. K. E-waste management: A review of recycling process, environmental and occupational health hazards, and potential solutions. *Environ. Nanotechnology, Monit. Manag.* **15**, 100409 (2021).

3. Kaya, M. Recovery of metals and nonmetals from electronic waste by physical and chemical recycling processes. *Waste Manag.* **57**, 64–90 (2016).

4. Gascoyne, P. R. C. & Vykoukal, J. Particle separation by dielectrophoresis. *Electrophoresis* **23**, 1973–83 (2002).

5. Pohl, H. A. The Motion and Precipitation of Suspensoids in Divergent Electric Fields. *J. Appl. Phys.* **22**, 869–871 (1951).

6. Farasat, M. *et al.* Signal-Based Methods in Dielectrophoresis for Cell and Particle Separation. *Biosensors* **12**, 510 (2022).

7. Suehiro, J., Guangbin Zhou, Imamura, M. & Hara, M. Dielectrophoretic filter for separation and recovery of biological cells in water. *IEEE Trans. Ind. Appl.* **39**, 1514–1521 (2003).

8. Jun, S., Chun, C., Ho, K. & Li, Y. Design and Evaluation of a Millifluidic Insulator-Based Dielectrophoresis (DEP) Retention Device to Separate Bacteria from Tap Water. *Water* **13**, 1678 (2021).

9. Lewpiriyawong, N., Xu, G. & Yang, C. Enhanced cell trapping throughput using DC-biased AC electric field in a dielectrophoresis-based fluidic device with densely packed silica beads. *Electrophoresis* **39**, 878–886 (2018).

10. Abd Rahman, N., Ibrahim, F. & Yafouz, B. Dielectrophoresis for Biomedical Sciences Applications: A Review. *Sensors* **17**, 449 (2017).

11. Park, J. *et al.* An efficient cell separation system using 3D-asymmetric microelectrodes. *Lab Chip* **5**, 1264 (2005).

12. Du, F., Baune, M., Kück, A. & Thöming, J. Dielectrophoretic gold particle separation. *Sep. Sci. Technol.* **43**, 3842–3855 (2008).

13. Weirauch, L. *et al.* Material-selective separation of mixed microparticles via insulator-based dielectrophoresis. *Biomicrofluidics* **13**, 64112 (2019).

14. Morgan, H. & Green, N. G. *AC Electrokinetics: colloids and nanoparticles*. (Research Studies Press, 2003).

15. Çetin, B. & Li, D. Dielectrophoresis in microfluidics technology. *Electrophoresis* **32**, 2410–2427 (2011).

16. Giesler, J., Weirauch, L., Thöming, J., Baune, M. & Pesch, G. R. High-throughput dielectrophoretic separator based on printed circuit boards. *Electrophoresis* **44**, 72–81 (2023).

17. Waheed, W., Sharaf, O. Z., Alazzam, A. & Abu-Nada, E. Dielectrophoresis-field flow fractionation for separation of particles: A critical review. *J. Chromatogr. A* **1637**, 461799 (2021).

18. Masuda, S., Washizu, M. & Nanba, T. Novel method of cell fusion in field constriction area in fluid integration circuit. *IEEE Trans. Ind. Appl.* **25**, 732–737 (1989).

19. Thwar, P. K., Linderman, J. J. & Burns, M. A. Electrodeless direct current dielectrophoresis using reconfigurable field-shaping oil barriers. *Electrophoresis* **28**, 4572–4581 (2007).

20. Regtmeier, J., Eichhorn, R., Viefhues, M., Bogunovic, L. & Anselmetti, D. Electrodeless dielectrophoresis for bioanalysis: theory, devices and applications. *Electrophoresis* **32**, 2253–73 (2011).

21. Lorenz, M. *et al.* High-throughput dielectrophoretic filtration of sub-micron and micro particles in macroscopic porous materials. *Anal. Bioanal. Chem.* **412**, 3903–3914 (2020).

22. Weirauch, L., Giesler, J., Baune, M., Pesch, G. R. & Thöming, J. Shape-selective remobilization of microparticles in a mesh-based DEP filter at high throughput. *Sep. Purif. Technol.* **300**, 121792 (2022).

23. Pesch, G. R. *et al.* Bridging the scales in high-throughput dielectrophoretic (bio-)particle separation in porous media. *Sci. Rep.* **8**, 10480 (2018).

24. Kepper, M., Rother, A., Thöming, J. & Pesch, G. R. Polarisability-dependent separation of lithium iron phosphate (LFP) and graphite in dielectrophoretic filtration. *Results Eng.* **21**, 101854 (2024).

25. *Electrokinetics and Electrodynamics in Microsystems. CISM Courses and Lectures, vol. 530*. (Springer Wien New York, 2011).

26. Pethig, R. *Dielectrophoresis. Theory, Methodology, and Biological Applications*. (John Wiley & Sons, 2017). doi:10.1002/9781118671443.

27. Andrew Zangwill. *Modern electrodynamics*. (Cambridge University Press, 2012).

28. Pethig, R. bound charges polarization. in *Dielectrophoresis. Theory, Methodology and Biological Applications* 57 (Wiley, 2017).

29. Richard P. Feyman; Leighton, Robert B.; Sands, M. *The Feynman lectures on physics. Volume 2: Mainly Electromagnetism and Matter*. (Addison-Wesley publishing company, 1964).

30. Weber, H. Ueber eine Darstellung willkürlicher Functionen durch Bessel'sche Functionen. *Math. Ann.* **6**, 146–161 (1873).

31. Lapizco-Encinas, B. H. The latest advances on nonlinear insulator-based electrokinetic microsystems under direct current and low-frequency alternating current fields: a review. *Anal. Bioanal. Chem.* **414**, 885–905 (2022).

32. Kao, K. C. *Dielectric Phenomena in Solids*. (Elsevier Academic Press, 2004).

33. Pesch, G. R. *et al.* Recovery of submicron particles using high-throughput

dielectrophoretically switchable filtration. *Sep. Purif. Technol.* **132**, 728–735 (2014).

34. Green, N. G. & Nili, H. Dielectrophoresis BT - Encyclopedia of Nanotechnology. in (ed. Bhushan, B.) 534–543 (Springer Netherlands, 2012). doi:10.1007/978-90-481-9751-4_131.

35. Bücker, M., Flores Orozco, A., Undorf, S. & Kemna, A. On the Role of Stern- and Diffuse-Layer Polarization Mechanisms in Porous Media. *J. Geophys. Res. Solid Earth* **124**, 5656–5677 (2019).

36. Zhao, H. Double-layer polarization of a non-conducting particle in an alternating current field with applications to dielectrophoresis. *Electrophoresis* **32**, 2232–2244 (2011).

37. Ermolina, I. & Morgan, H. The electrokinetic properties of latex particles: comparison of electrophoresis and dielectrophoresis. *J. Colloid Interface Sci.* **285**, 419–28 (2005).

38. Green, N. G. & Morgan, H. Dielectrophoresis of Submicrometer Latex Spheres. 1. Experimental Results. *J. Phys. Chem. B* **103**, (1999).

39. Ramos, A., García-Sánchez, P. & Morgan, H. AC electrokinetics of conducting microparticles: A review. *Curr. Opin. Colloid Interface Sci.* **24**, 79–90 (2016).

40. Ren, Y. K., Morganti, D., Jiang, H. Y., Ramos, A. & Morgan, H. Electrorotation of metallic microspheres. *Langmuir* **27**, 2128–2131 (2011).

41. Bazant, M. Z., Thornton, K. & Ajdari, A. Diffuse-charge dynamics in electrochemical systems. *Phys. Rev. E* **70**, 21506 (2004).

42. Ramos, A., Morgan, H., Green, N. G. & Castellanos, A. The role of electrohydrodynamic forces in the dielectrophoretic manipulation and separation of particles. *J. Electrostat.* **47**, 71–81 (1999).

43. Li, S., Marshall, J. S., Liu, G. & Yao, Q. Adhesive particulate flow: The discrete-element method and its application in energy and environmental engineering. *Prog. Energy Combust. Sci.* **37**, 633–668 (2011).

44. Lorenz, M. Dielectrophoretic filtration of particles in porous media: concept, design, and selectivity. (2021) doi:10.26092/elib/593.

45. Huysmans, M. & Dassargues, A. Review of the use of Péclet numbers to determine the relative importance of advection and diffusion in low permeability environments. *Hydrogeol. J.* **13**, 895–904 (2005).

46. Sharma, S., Shukla, P., Misra, A. & Mishra, P. R. Chapter 8 - Interfacial and colloidal properties of emulsified systems: Pharmaceutical and biological perspective. in (eds. Ohshima, H. & Makino, K. B. T.-C. and I. S. in P. R. and D.) 149–172 (Elsevier, 2014). doi:https://doi.org/10.1016/B978-0-444-62614-1.00008-9.

47. Salari, A. & Thompson, M. Recent advances in AC electrokinetic sample enrichment techniques for biosensor development. *Sensors Actuators B Chem.* **255**, 3601–3615 (2018).

48. Squires, T. M. & Bazant, M. Z. Induced-charge electro-osmosis. *J. Fluid*

Mech. **509**, 217–252 (2004).

49. Xuan, X. Review of nonlinear electrokinetic flows in insulator-based dielectrophoresis: From induced charge to Joule heating effects. *Electrophoresis* **43**, 167–189 (2022).

50. Hu, S. *et al.* A comprehensive review of alkaline water electrolysis mathematical modeling. *Appl. Energy* **327**, 120099 (2022).

51. Gencoglu, A. *et al.* Quantification of pH gradients and implications in insulator-based dielectrophoresis of biomolecules. *Electrophoresis* **32**, 2436–2447 (2011).

52. Weirauch, L. Multidimensional sorting of microparticles in electrically switchable dielectrophoretic filters. (PhD Thesis, Universität Bremen, 2023). doi:doi:10.26092/elib/2692.

53. Ran An. Electrochemical processes in microfluidics systems under AC electric fields. (Michigan Technological University, 2015). doi:https://doi.org/10.37099/mtu.dc.etds/951.

54. Perez-Gonzalez, V. H. Particle trapping in electrically driven insulator-based microfluidics: Dielectrophoresis and induced-charge electrokinetics. *Electrophoresis* **42**, 2445–2464 (2021).

55. Derjaguin, B. & Landau, L. Theory of the stability of strongly charged lyophobic sols and of the adhesion of strongly charged particles in solutions of electrolytes. *Prog. Surf. Sci.* **43**, 30–59 (1993).

56. Mavis, F. T. & Wilsey, E. F. *A study of the permeability of sand*. (State University of Iowa, 1936). doi:10.17077/006163.

57. Curry, C. W., Bennett, R. H., Hulbert, M. H., Curry, K. J. & Faas, R. W. Comparative Study of Sand Porosity and a Technique for Determining Porosity of Undisturbed Marine Sediment. *Mar. Georesources Geotechnol.* **22**, 231–252 (2004).

58. Scott, G. D. Packing of Spheres: Packing of Equal Spheres. *Nature* **188**, 908–909 (1960).

59. Pal, L., Joyce, M. & Fleming, P. D. A Simple Method for Calculation of the Permeability Coefficient of Porous Media. *TAPPI J.* **5**, 10–16 (2006).

60. Wang, D. & Fan, L.-S. Particle characterization and behavior relevant to fluidized bed combustion and gasification systems. in *Fluidized Bed Technologies for Near-Zero Emission Combustion and Gasification* (ed. Scala, F.) 42–76 (Woodhead Publishing, 2013). doi:10.1533/9780857098801.1.42.

61. da Silva, M. T. Q. S., do Rocio Cardoso, M., Veronese, C. M. P. & Mazer, W. Tortuosity: A brief review. *Mater. Today Proc.* **58**, 1344–1349 (2022).

62. Zhang, S., Li, R. & Pei, J. Evaluation methods and indexes of morphological characteristics of coarse aggregates for road materials: A comprehensive review. *J. Traffic Transp. Eng. (English Ed.)* **6**, 256–272 (2019).

63. O'Donnell M.C., Kepper M., Pesch G.R. A brief history and future directions of dielectrophoretic filtration: A review. *Electrophoresis*. 1-21 (2024).

64. Pohl, H. A. & Hawk, I. Separation of Living and Dead Cells by Dielectrophoresis. *Science (80-.).* **152**, 647-649. (1966).

65. Ting, I. P., Jolley, K., Beasley, C. A. & Pohl, H. A. Dielectrophoresis of chloroplasts. *Biochim. Biophys. Acta - Bioenerg.* **234**, 324–329 (1971).

66. Tada, S., Hayashi, M., Eguchi, M. & Tsukamoto, A. High-throughput separation of cells by dielectrophoresis enhanced with 3D gradient AC electric field. *Biomicrofluidics* **11**, 64110 (2017).

67. Adams, T. N. G. *et al.* Label-free enrichment of fate-biased human neural stem and progenitor cells. *Biosens. Bioelectron.* **152**, 111982 (2020).

68. Ayash, A. A., Al-Moameri, H. H., Salman, A. A., Lubguban, A. A. & Malaluan, R. M. Analysis and Simulation of Blood Cells Separation in a Polymeric Serpentine Microchannel under Dielectrophoresis Effect. *Sustainability* vol. 15 (2023).

69. Oshiro, K. *et al.* Fabrication of a new all-in-one microfluidic dielectrophoresis integrated chip and living cell separation. *iScience* **25**, (2022).

70. Hughes, M. P. Fifty years of dielectrophoretic cell separation technology. *Biomicrofluidics* **10**, (2016).

71. Morgan, Hywel; Green, N. J is in AC electrokinetics. in *AC Electrokinetics: colloids and nanoparticles* 17, 24–26 (Research Studies Press LTD., 2003).

72. Ghomian, T. & Hihath, J. Review of Dielectrophoretic Manipulation of Micro and Nanomaterials: Fundamentals, Recent Developments, and Challenges. *IEEE Trans. Biomed. Eng.* **70**, 27–41 (2023).

73. Masaeli, M. *et al.* Continuous Inertial Focusing and Separation of Particles by Shape. *Phys. Rev. X* **2**, 31017 (2012).

74. Kwak, T. J., Jung, H., Allen, B. D., Demirel, M. C. & Chang, W.-J. Dielectrophoretic separation of randomly shaped protein particles. *Sep. Purif. Technol.* **262**, 118280 (2021).

75. Wang, X.-B., Vykoukal, J., Becker, F. F. & Gascoyne, P. R. C. Separation of Polystyrene Microbeads Using Dielectrophoretic/Gravitational Field-Flow-Fractionation. *Biophys. J.* **74**, 2689–2701 (1998).

76. Chen, Q. & Yuan, Y. J. A review of polystyrene bead manipulation by dielectrophoresis. *RSC Adv.* **9**, 4963–4981 (2019).

77. P R C Gascoyne, Ying Huang, R Pethig, J Vykoukal & F F Becker. Dielectrophoretic separation of mammalian cells studied by computerized image analysis. *Meas. Sci. Technol.* **3**, 439 (1992).

78. Riahifar, R. *et al.* Sorting ZnO particles of different shapes with low frequency AC electric fields. *Mater. Lett.* **65**, 632–635 (2011).

79. Dubose, J. *et al.* Microfluidic electrical sorting of particles based on shape in a spiral microchannel. *Biomicrofluidics* **8**, 14101 (2014).

80. Huang, K., Guo, J. & Xu, Z. Recycling of waste printed circuit boards: A review of current technologies and treatment status in China. *J. Hazard. Mater.* **164**, 399–408 (2009).

81. Sano, N., Iwase, K. & Tamon, H. *In-Situ* Estimation of Selective Capture of Tungsten Carbide Particles from Mixture with Diatomite Particles by Mesh-Stacked Dielectrophoresis Separator. *J. Chem. Eng. JAPAN* **46**, 535–540 (2013).

82. Natarajan, S. & Aravindan, V. An Urgent Call to Spent LIB Recycling: Whys and Wherefores for Graphite Recovery. *Adv. Energy Mater.* **10**, 2002238 (2020).

83. Mennik, F., Dinç, N. İ. & Burat, F. Selective recovery of metals from spent mobile phone lithium-ion batteries through froth flotation followed by magnetic separation procedure. *Results Eng.* **17**, 100868 (2023).

84. Al-Shammari, H. & Farhad, S. Chapter 13 - Separating battery nano/microelectrode active materials with the physical method. in *Micro and Nano Technologies* (eds. Farhad, S., Gupta, R. K., Yasin, G. & Nguyen Remanufacturing, and Reusing, T. A. B. T.-N. T. for B. R.) 263–286 (Elsevier, 2022). doi:https://doi.org/10.1016/B978-0-323-91134-4.00016-9.

85. Jones, T. B. Basic theory of dielectrophoresis and electrorotation. *IEEE Eng. Med. Biol. Mag.* **22**, 33–42 (2003).

86. Chiou, P. Y., Chang, Z. & Wu, M. C. A novel optoelectronic tweezer using light induced dielectrophoresis. in *2003 IEEE/LEOS International Conference on Optical MEMS (Cat. No.03EX682)* 8–9 (2003). doi:10.1109/OMEMS.2003.1233441.

87. Barasinski, M., Pesch, G. R. & Garnweitner, G. Chapter 7 - Electrophoresis and dielectrophoresis. in *Handbooks in Separation Science* (ed. Contado, C. B. T.-P. S. T.) 179–219 (Elsevier, 2022). doi:https://doi.org/10.1016/B978-0-323-85486-3.00009-3.

88. Lin, I. J. & Benguigui, L. Dielectrophoretic Filtration and Separation: General Outlook. *Sep. Purif. Methods* **10**, 53–72 (1981).

89. Benguigui, L. & Lin, I. J. Dielectrophoretic Filtration of Nonconductive Liquids. *Sep. Sci. Technol.* **17**, 1003–1017 (1982).

90. Ham, G. & Barnes, R. Process of Purifying Hydrocarbon Liquids, US patent 2534907. (1950).

91. Hamlin, H. Electrical Precipitation Method, US patent 2573967. (1951).

92. Shirley, W. Method and Apparatus for Unloading Filters, US patent 3394067. (1968).

93. Oberton, S. Electrofiltration Process for Purifying Organic Liquids, patent US4040926. (1977).

94. Landis, J. V. Quality improvement process for organic liquid, patent US4155924A. (1979).

95. Waterman, L. C. & Franse, A. D. Electric filter, US patent 3324026. (1967).

96. Fritsche & Haniak. Electrofilter, patent US3928158. (1975).

97. Fritsche, G., Bujas, R. & Caprioglio, G. Electrostatic separator using a bead bed, patent EP0570108A2. (1993).

98. Franse, A. Electrofilter system, patent US3799857A. (1974).

99. Crissman, J., Fritsche, G., Hamel, F. & Hilty, L. Radial Flow Electrostatic Filter, US patent 4059498. (1977).

100. Dietz, P. W. Electrostatic filtration of inertialess particles by granular beds. *J. Aerosol Sci.* **12**, 27–38 (1981).

101. Lin, I. J. & Benguigui, L. Dielectrophoretic Filtration of Liquids. II. Conducting Liquids. *Sep. Sci. Technol.* **17**, 645–654 (1982).

102. Watson, F., Mayse, W. & Franse, A. Radial Flow Electrofilter, US patent 4372837. (1983).

103. Lin, I. J. & Benguigui, L. Dielectrophoretic Filtration in Time-Dependent Fields. *Sep. Sci. Technol.* **20**, 359–376 (1985).

104. Sisson, W. G., Brunson, R. R., Scott, T. C., Harris, M. T. & Look, J. L. Removal of Submicron Silica Particles from *tert* -Amyl Alcohol by Dielectric/Electric Packed Bed Filtration. *Sep. Sci. Technol.* **30**, 1421–1434 (1995).

105. Halm, R. & Hayes, K. Method for removing particulate from a liquid silicon containing compound, patent EP0995770A2. (2000).

106. Wakeman, R. J. & Butt, G. An Investigation of High Gradient Dielectrophoretic Filtration. *Chem. Eng. Res. Des.* **81**, 924–935 (2003).

107. Zhang, Z. *et al.* Effect of structural parameters of an electrostatic separator on the removal of catalyst particles from fluid catalytic cracking slurry. *Sep. Purif. Technol.* **222**, 11–21 (2019).

108. Li, Q. *et al.* Microscopic mechanistic study on the removal of catalyst particles in FCCS by an electrostatic field. *Powder Technol.* **363**, 500–508 (2020).

109. Li, Q. *et al.* Experimental study on the removal of FCCS catalyst particles by electrostatic separation. *Energy Sources, Part A Recover. Util. Environ. Eff.* **45**, 3490–3502 (2023).

110. Li, Q. *et al.* Effects of the properties of FCCS on the removing of catalyst particles from FCCS under a DC electrostatic field. *Pet. Sci.* **20**, 1885–1894 (2023).

111. Li, Q. *et al.* Experimental study on the removal of FCCS catalyst particles by the coupling interaction of the electrostatic field and flow field. *Pet. Sci. Technol.* **41**, 457–476 (2023).

112. Li, Q. *et al.* Influence of filler characteristics on particle removal in fluid catalytic cracking slurry under an alternating electric field. *Pet. Sci.* **21**, 2102–2111 (2024).

113. Shen, Y., Elele, E. & Khusid, B. A novel concept of dielectrophoretic engine oil filter. *Electrophoresis* **32**, 2559–68 (2011).

114. Islam, M. N., Gagnon, Z. R. & Mcferrin, A. Dielectrophoretic Trapping in Paper: Paper-based Electric Field Gradients for High-Throughput Particle Trapping. *Engrxiv Eng. Arch.* (2022).

115. Pesch, G. R., Kiewidt, L., Du, F., Baune, M. & Thöming, J. Electrodeless dielectrophoresis: Impact of geometry and material on obstacle polarization. *Electrophoresis* **37**, 291–301 (2016).

116. Pesch, G. R., Du, F., Baune, M. & Thöming, J. Influence of geometry and material of insulating posts on particle trapping using positive dielectrophoresis. *J. Chromatogr. A* **1483**, 127–137 (2017).

117. Saucedo-Espinosa, M. A. Improving the Design and Application of Insulator-Based Dielectrophoretic Devices for the Assessment of Complex Mixtures. (Rochester Institute of Technology, 2017).

118. Crowther, C. V. & Hayes, M. A. Refinement of insulator-based dielectrophoresis. *Analyst* **142**, 1608–1618 (2017).

119. Kepper, M. Online repository for additional information of the DEP filter simulations and recovery rates. (2024) doi:10.5281/zenodo.13123824.

120. Bolte, S. & Cordelières, F. P. A guided tour into subcellular colocalization analysis in light microscopy. *J. Microsc.* **224**, 213–232 (2006).

121. Yang, M.-R., Ke, W. & Wu, S. Improving electrochemical properties of lithium iron phosphate by addition of vanadium. *J. Power Sources* **165**, 646–650 (2007).

122. Wang, G. X. *et al.* Physical and electrochemical properties of doped lithium iron phosphate electrodes. *Electrochim. Acta* **50**, 443–447 (2004).

123. Giesler, J. *et al.* Sorting Lithium-Ion Battery Electrode Materials Using Dielectrophoresis. *ACS omega* **8**, 26635–26643 (2023).

124. Guo, T. *et al.* Plasmonic porous ceramics based on zirconia-toughened alumina functionalized with silver nanoparticles for surface-enhanced Raman scattering. *Open Ceram.* **9**, 100228 (2022).

125. Guo, T., Murshed, M. M., Rezwan, K. & Maas, M. Ceramic Open Cell Foams Featuring Plasmonic Hybrid Metal Nanoparticles for In Situ SERS Monitoring of Catalytic Reactions. *Adv. Mater. Interfaces* **10**, 2300207 (2023).

126. Mortensen, N. A. Mesoscopic electrodynamics at metal surfaces . *From quantum-corrected hydrodynamics to microscopic surface-response formalism* vol. 10 2563–2616 (2021).

127. Iliescu, C., Xu, G., Loe, F. C., Ong, P. L. & Tay, F. E. H. A 3-D dielectrophoretic filter chip. *Electrophoresis* **28**, 1107–14 (2007).

128. Iliescu, C., Xu, G. L., Ong, P. L. & Leck, K. J. Dielectrophoretic separation of biological samples in a 3D filtering chip. *J. Micromechanics Microengineering* **17**, S128–S136 (2007).